Beam-Spin Asymmetry of Exclusive Coherent Electroproduction of the π^0 Off ^{4}He

Frank Thanh Cao, Ph.D.

University of Connecticut, 2019

To understand the partonic structure of nucleons in nuclei, extracting the beam spin asymmetry (BSA) from exclusive processes is an important measurement to get at the so-called Generalized Parton Distributions (GPDs) that describe the partons behavior inside the nucleon. In particular, BSA in Deeply Virtual Meson Production (DVMP) can offer valuable constraints on the transverse GPDs which are not accessible through Deeply Virtual Compton Scattering (DVCS). Furthermore, DVMP measurements on bound nucleons can offer insights into structure modification due to the nuclear environment. The interpretation of this bounded nucleon (incoherent) DVMP on nuclear targets rests on the assumption of factorization [1] and that higher-order effects are negligible. These assumptions can be tested through measurement of nuclear (coherent) DVMP on a spin-0 target, where at leading order the BSA should be zero [2]. Any non-zero BSA can indicate the size of the higher-order contributions. In the CLAS EG6 experiment, the spin-0 ^{4}He gas target is probed via the deeply virtual ($Q^2 > 2$ (GeV/c)^2) photons from 6 GeV longitudinally polarized electrons. This paper will dis-

cuss the results of coherent meson electroproduction of π^0 off ^{4}He where the BSA is measured to be consistent with zero. This benchmark measurement is in agreement with symmetry arguments presented in a recent theoretical formulation [2] that offers a framework complementary to that of the GPDs and gives confidence in the assumptions made for future studies of exclusive nuclear processes.

Beam-Spin Asymmetry of Exclusive Coherent Electroproduction of the π^0 Off ^{4}He

Frank Thanh Cao

B.S., University of Massachusetts Boston, 2011

M.S., University of Massachusetts Boston, 2013

A Dissertation

Submitted in Partial Fulfillment of the

Requirements for the Degree of

Doctor of Philosophy

at the

University of Connecticut

2019

APPROVAL PAGE

Doctor of Philosophy Dissertation

Beam-Spin Asymmetry of Exclusive Coherent Electroproduction of the π^0 Off ^{4}He

Presented by

Frank Thanh Cao, M.S.

Major Advisor

Kyungseon Joo

Associate Advisor

Kawtar Hafidi

Associate Advisor

Peter Schweitzer

University of Connecticut

2019

For you Danny Thanh Cao.

Thank you for looking over us from above. I hope you are proud of me, little brother.

I promise to continue to work towards that.

ACKNOWLEDGEMENTS

First, I want to thank my dear family who have been so patient with me and trusting me with this rather *selfish* pursuit. I truly would be nothing without you.

Thank you, mom for continuing to work your low wage service job at your older age so that I can pursue what I love. I am deeply grateful for *all* that you have done in my life.

Kyungseon, thank you for the opportunity to do this research and thank you in particular for the opportunity to be in Chicago where I have thrived and where I continue to grow. I have taken so much out of my time here in all aspects of my life; it perfectly suited me and there is no place I would have rather been.

Kawtar, thank you for the opportunity to work with the amazing people at Argonne National Lab. I truly appreciate you taking me in as one of your own and the tough love was just what I needed.

Mohammad, thank you for your patience with me. Letting me bug you all those long hours in your office have really had an impact on me – your hard work ethic and curiosity is infectious.

Whitney, I also want to thank you for your patience with me. Our long discussions have really impacted how I think and approach a problem – with a great degree of organizational finesse. I truly value our conversations; your insight, in just about everything, is inspiring.

Thank you all of my friends from Boston to Chicago that have supported me and cheered me on all along the way. You make my tougher days better.

TABLE OF CONTENTS

LIST OF FIGURES

LIST OF TABLES

Chapter 1

Introduction and Overview

1.1 Overview

The focus of this thesis is the exclusive process of the Deeply Virtual Meson Production (DVMP) of π^0 off ^{4}He:

$$e\ {}^4\text{He} \rightarrow e\ {}^4\text{He}\ \pi^0, \tag{1.1}$$

of which the background and motivation will be built up in **Chapter 2** and **Chapter 3**, respectively. The so-called coherent channel of this DVMP of π^0 (DVπ^0P) process off ^{4}He is of particular interest due to the symmetries involved in the reaction. In this deeply virtual process (where the square-momentm transferred from the electron, i.e. the resolution, is $Q^2 > 1\,(\text{GeV}/c)^2$), the produced π^0 is pseudoscalar and the recoiling ^{4}He, which is left intact, is scalar. This alone limits the pairwise components of the interaction between the virtual photon and partons involved. The measurement of interest will be an extraction of the model-independent beam spin asymmetries to put constraints on these components.

This exclusive process requires the detection of the very short-lived π^0 (lifetime on the order of 10^{-17} s [3]). Such a short life time cannot be measured, but the π^0

decays into a pair of photons with a branching ratio of 98.8% [3], and photon detection is straight forward. The CLAS EG6 experiment was just the unique experiment, with its 6 GeV longitudinally polarized electron beam and gas ^{4}He target, to study this fully exclusive processes: the existing CLAS measured the scattered electron; the addition of the Inner Calorimeter (IC) extended the CLAS acceptance to detect high energy, low-polar-angle photons; and the addition of the Radial Time Projection Chamber (RTPC) allowed the detection of low-momentum recoiled ^{4}He nuclei (discussed in **Chapter 4**).

To study full exclusivity, every particle (or its decay products) on both sides of **Eq. 1.1** needs to be identified. The initial ^{4}He is taken to be at rest and the initial electron is taken to be from the beam. Particle identification of the final state particles follows the procedure outlined in [4, 5] and is shown in full in **Chapter 5**. Identification of the final state electron, helium, and photons is essential to ensure the exclusivity of the process.

However, the detection of a scattered electron, a recoiled helium track, and two photons alone does not mean that the event is part of the exclusive coherent DVπ^0P off ^{4}He. Any one of the detected particles could be misidentified and any subset of the particles detected could be part of an unrelated process. Event selection is required to then sort through these sets of positively identified particles to select the ones relevant to coherent DVπ^0P process of interest. The accepted standard event selection is done through a series of exclusivity variable cuts that is ubiquitous in analyses including similar studies done in [4, 6, 7] and [5], among many other CLAS analyses [8, 9, 10, 11, 12] (discussed in **Chapter 6**). As an alternative method to ensure exclusivity,

this thesis introduces kinematic fitting as event selection following the nonlinear least-squares fit formalism outlined in [13] (introduced in **Chapter 7** and constructed for this experimental setup in **Chapter 8**). Though this is not the first time kinematic fitting has been used in CLAS (previous works in CLAS [14, 15, 16, 17, 18]), it is however, a first look at kinematic fitting applied to electron scattering off nuclei.

To check the robustness of the kinematic fitting procedure, the fit is first applied to select coherent Deeply Virtual Compton Scattering (DVCS):

$$e\ {}^4\mathrm{He} \rightarrow e\ {}^4\mathrm{He}\ \gamma \quad , \tag{1.2}$$

using only conservation of momentum and energy of an exclusive process (discussed in **Chapter 9**). This starting point has many advantages: the particles involved are convenient – every particle involved in DVCS is also involved in DVπ^0P; there are fewer particles involved in this reaction so all correlations entering the construction of the fit can be better isolated and studied; and there are many more events –the results will not be limited by statistics and the shapes of the various distributions are better characterized. Moreover, the results of DVCS off ^{4}He, using a different event selection method, has been peer-reviewed and published [6], so testing the kinematic fitting procedure can check the feasibility of the fitting procedure as well as to cross-validate the results.

Naturally, by simply including another detected photon into the fit, we can begin to look at coherent DVπ^0P events:

$$e\ {}^4\mathrm{He} \rightarrow e\ {}^4\mathrm{He}\ \gamma\ \gamma, \tag{1.3}$$

discussed in **Chapter 10**. Here, the power of kinematic fitting coupled with the constraints of exclusivity is fully exemplified. The fit, termed a $4C$-fit, only uses conservation of momentum and energy of the particles in **Eq. 1.3**. However, when looking at the invariant mass of distribution of two selected photons, a clear peak with very little background is shown at the nominal value of π^0 mass without any mention of this value anywhere in the fitting procedure. To ensure that the π^0 is selected, an additional invariant mass cut on the photon pair can be applied.

Instead, a fit which also simultaneously includes the decay of the π^0:

$$\begin{aligned} e\ {}^4\text{He} &\rightarrow e\ {}^4\text{He}\ \pi^0 \\ \pi^0 &\rightarrow \gamma\ \gamma \end{aligned} \quad , \tag{1.4}$$

termed a $5C$-fit, is introduced and deployed (discussed in **Chapter 11**). The results of this final $5C$-fit are outlined in **Chapter 12** and compared to the results of the previous study where event selection was done with exclusivity variable cuts in **Chapter 13**.

Once the events have been selected, by whichever method, an extraction of the beam spin asymmetry (BSA) of the longitudinally polarized electron beam on an unpolarized, spin-0 helium target is measured, represented as A_{LU}. Then, statistical uncertainties are calculated and systematic studies are done to quantify the contributions of uncertainty that limit the measurement in **Chapter 14**. Finally, the physical interpretations of the results will be discussed and an outlook will be outlined to consider measurements and experiments for a path moving forward in the concluding chapters, **Chapters 15 & 16** .

1.2 Primer: Fixed Target Electron Scattering Notation

Since all discussion in this thesis will be on fixed target electron scattering, the kinematics variables that will be used throughout the text will be listed here in the lab frame for convenience.

In fixed target electron scattering, an electron (e) with initial 4-momentum

$$k = \left(\vec{\boldsymbol{k}}, E\right) \tag{1.5}$$

is scattered (e'), with resulting 4-momentum

$$k' = \left(\vec{\boldsymbol{k}}', E'\right), \tag{1.6}$$

via the exchange of a virtual photon (γ^*), with 4-momentum q and energy ν, uniquely defined by the e and e':

$$q := k - k' = \left(\vec{\boldsymbol{q}}, \nu\right), \tag{1.7}$$

off a fixed target nucleon (N) of mass M, initial 4-momentum

$$p = \left(\vec{\boldsymbol{0}}, M\right), \tag{1.8}$$

and recoiled (N') final state 4-momentum p'.

1.2.1 Useful Lorentz Invariant Quantities

Some useful quantities that will be pervasive include, but are not limited to, the squared momentum transfer,

$$Q^2 := -q^2 > 0 \quad , \tag{1.9}$$

the squared momentum transfer from the initial to the final state target

$$t := \left(p - p'\right)^2 \tag{1.10}$$

For deep processes, where the virtual photon interacts with the partonic structure of the nucleon, the useful variables, to add to the previously defined ones are the fractional momentum component of the struck quark to the nucleon

$$x := Q^2 / \left(2p \cdot q\right) \quad , \tag{1.11}$$

the fractional energy of struck quark to the nucleon

$$y := p \cdot q / p \cdot k \quad , \tag{1.12}$$

and the squared invariant mass of the nucleon and virtual photon system

$$W^2 := (p+q)^2 = M^2 + 2p \cdot q - Q^2 = M^2 + \frac{1-x}{x} Q^2 \quad . \tag{1.13}$$

1.2.2 Lab Frame Kinematics

The virtual photon squared momentum transfer and energy can be expressed in terms of the lab frame variables as

$$Q^2 = 4EE' \sin^2 \frac{\theta}{2} \tag{1.14}$$

$$\nu = E - E' \tag{1.15}$$

$$x = Q^2 / 2M\nu \tag{1.16}$$

where E and E' are the energy of the intial and scattered electron, respectively, and θ being the polar angle between them, all in the lab frame.

Chapter 2

Background and Theoretical Framework

It has been long since Rutherford's elastic scattering experiments demonstrated that within the atom, there is a dense nuclear core. The nuclear core, i.e. the nucleus, was resolved to be made up of nucleons (protons and neutrons). The nucleons were once thought of as fundamental, point-like particles.

However, the first evidence for the composite nature of nucleons came to light with measurements of the proton's magnetic moment[19, 20] showed that the proton was not a point-like particle. Stanford Linear Accelerator (SLAC) experiments in the mid 1950's [21] then measured that the charge distribution of the proton with elastic electron-proton (e-p) scattering experiments. This showed that the protons having some finite size extent through their electric and magnetic form factors, by way of the Rosenbluth separation [22].

The Rosenbluth separation can be shown in differential cross-section

$$\left(\frac{d\sigma}{d\Omega}\right)_{\text{Rosenbluth}} = \left(\frac{E'}{E}\right)\left[\frac{G_E^2 + \tau G_M^2}{1+\tau} + 2\tau G_M^2 \tan^2\frac{\theta}{2}\right]\left(\frac{d\sigma}{d\Omega}\right)_{\text{Mott}}, \tag{2.1}$$

where $\tau := \frac{Q^2}{4M^2}$; $\left(\frac{d\sigma}{d\Omega}\right)_{\text{Mott}}$ is the Mott differential cross-section (see **Appendix A**); and the electric $G_E(Q^2)$ and magnetic $G_M(Q^2)$ Form Factors (FFs), depending solely on the

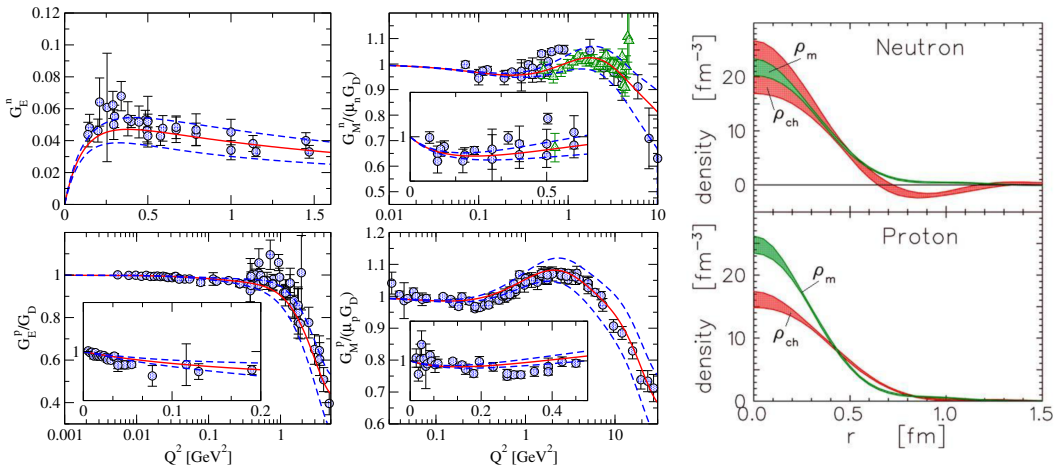

(a) Nucleon electric and magnetic FFs vs Q^2 [23]

(b) Nucleon charge densities [23]

Fig. 2.1: World data of electric and magnetic form factors as function of Q^2 and corresponding, Fourier transformed, charge density distributions for the proton and neutron

momentum transfer Q^2 (see **Eq. 1.9**), can be separated to measure the extent of the nucleons. This lead to effort in extracting the nucleon FFs (a modern compilation of world data can be seen in **Fig. 2.1a**) which can in turn with a Fourier transformation be used to infer the charge density to get at the nucleon radius (seen in **Fig. 2.1b**).

To truly realize the nucleons' extent is due to being composite in nature, much more energy was needed to improve the resolution required to go beyond what we now know as the elastic scattering regime. SLAC, continuing its tradition, accomplished this in 1967 and 1973 with experiments [24, 25], wherein inclusive deep inelastic scattering measurements suggested substructure with point-like, spin-1/2 particles, in the nucleon.

This can be seen by measuring the differential cross-section at finer resolution or, equivalently, higher momentum transfer Q^2 (see **Eq. 1.9**). To get a sense of the scale in Q^2, the idea is to be able to resolve distances below the nucleon radius of $\sim$ 1 fm

which, via the Compton wavelength, corresponds to $Q^2 > 1$ (GeV/c)^2. This is seen as the "deeply virtual" regime since Q^2 can also be thought of as the virtual photon's squared invariant mass. And so Q^2 is also often referred to as the 'virtuality'.

From elastic electron-proton scattering, for large Q^2, $G_M\left(q^2\right) \sim \frac{1}{(Q^2)^2}$. Thus at high Q^2, the Rosenbluth differential cross-section becomes:

$$\lim_{Q^2\to\infty}\left(\frac{d\sigma}{d\Omega}\right)_{\text{Rosenbluth}} \sim \tau G_M^2 \sim \frac{1}{\left(Q^2\right)^3} \tag{2.2}$$

However, the measurements at SLAC did not agree with this predicted power law in Q^2, as can be seen by the elastic scattering curve in **Fig. 2.2**. The measured reduced cross-sections was much shallower in Q^2 and depended on the final state invariant mass W (see **Eq. 1.13**).

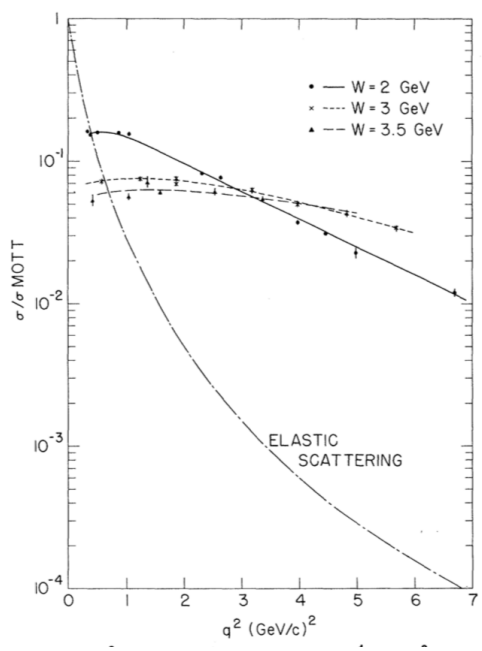

Fig. 2.2: DIS: Reduced cross section as a function of Q^2 [26].

2.1 Deep Inelastic Scattering (DIS)

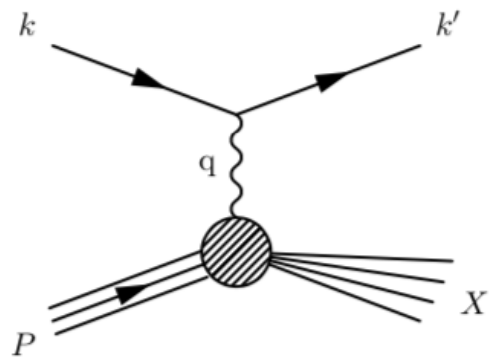

Fig. 2.3: Schematic diagram of DIS [27]

The fact that the reduced cross-sections become less dependent on Q^2, at higher and higher W, hint at the electron scattering off point-like, spin 1/2 particles, since the equivalent probe size $\sim 1/Q^2$ becomes irrelevant. Gell-Mann and Zweig proposed that these particles, which were named quarks, were fractionally-charged in their quark model [28, 29]. Later, together with Feynman's parton model, this Quark-Parton Model, was able to describe a wide variety of baryons and mesons [30]. Still, there was much that it could not describe.

From **Fig. 2.2**, we see that the cross-section depends on two variables. A schematic of the inclusive DIS process can be seen in **Fig. 2.3** where only the kinematics of the electron (initial and final state) are measured. In addition to Q^2, an additional variable needs to be defined in order to parametrize the unmeasured final state nucleon from the measured interaction between the initial state nucleon and the virtual photon. Two

choices are longitudinal momentum fraction

$$x := Q^2 / (2p \cdot q) \tag{2.3}$$

and the final state invariant mass W following from

$$W^2 := (p+q)^2 . \tag{2.4}$$

From this parametrization, Drell and Walecka [31] showed, in the same spirit as the Rosenbluth form, that the deep inelastic scattering differential cross-section in terms of solid angle Ω and virtual photon energy ν can be written as:

$$\left(\frac{d^2\sigma}{d\Omega d\nu}\right)_{\text{DIS}} = \left[\frac{2}{M} F_1\left(x, Q^2\right) \tan^2\frac{\theta}{2} + \frac{1}{\nu} F_2\left(x, Q^2\right)\right] \left(\frac{d\sigma}{d\Omega}\right)_{\text{Mott}} . \tag{2.5}$$

Here, for the electron interacting with point-like spin-1/2 partons, F_1 and F_2 are the so-called Parton Distribution Functions (PDFs) that encode the quarks' momentum distribution inside the proton for a given longitudinal momentum fraction x and virtuality Q^2. Efforts have been made to map out these PDFs for a wide range of x and Q^2 (see **Fig. 2.4**). The Q^2 dependence of these curves can be explained by the so-called DGLAP evolution equations [32].

Furthermore, efforts have been made to measure the parton content of the nucleons for a decomposition of the coontributions from the different flavors (up and down valence quarks, gluons, and sea quarks). The HERA collaboration shows these measurements for the proton in **Fig. 2.5** where at high x the parton content is mostly valence up and down quarks in a 2:1 ratio supporting the previous quark model where the proton is three quarks (2 up and 1 down).

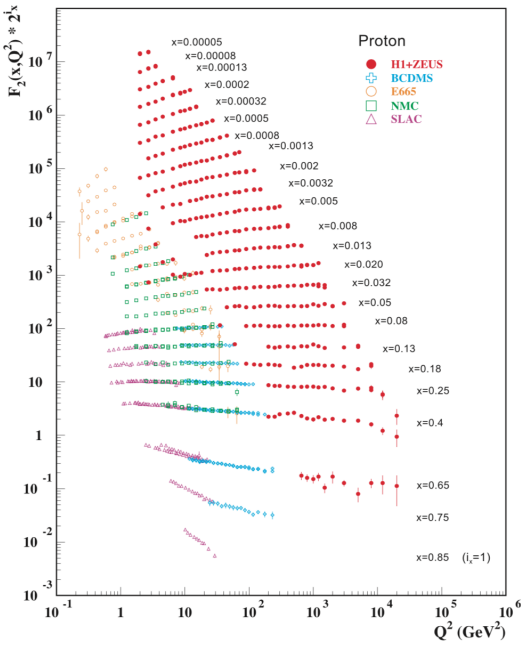

Fig. 2.4: F_2 structure vs Q^2 for proton [33].

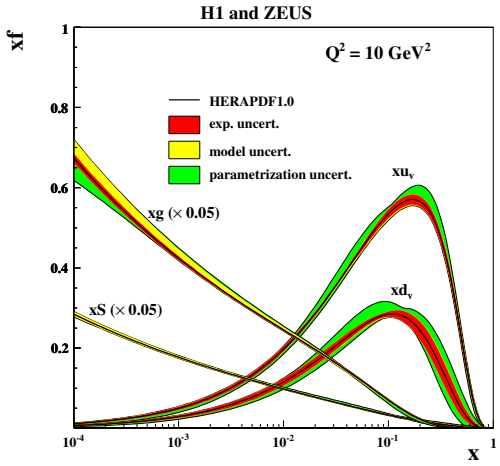

Fig. 2.5: PDFs dependence on x [34].

Altogether inclusive DIS leads to a modern quantum chromodynamic picture of the nucleon. Note that all of the kinematic factors were defined completely from the energy and angle of the scattered electron – a hallmark of inclusive DIS. Though

this makes inclusive DIS convenient and has lead to many key insights of the partonic nature of the nucleon, the information accessible is quite limited. Generally speaking, it is limited to one-dimensional structure of the nucleon.

2.2 Beyond DIS

Additional information of hadronic structure can be unlocked and accessed by the so-called

- Transverse Mometum Distributions (TMDs) in Semi-Inclusive Deep Inelastic Scattering (SIDIS)
- Generalized Parton Distributions (GPDs) in hard exclusive reactions or processes

A general relation between these and the higher Generalized Transverse-Momentum depenent parton Distributions (GTMDs), as well as lower structure that include the FFs and PDFs, can be seen in **Fig. 2.6**.

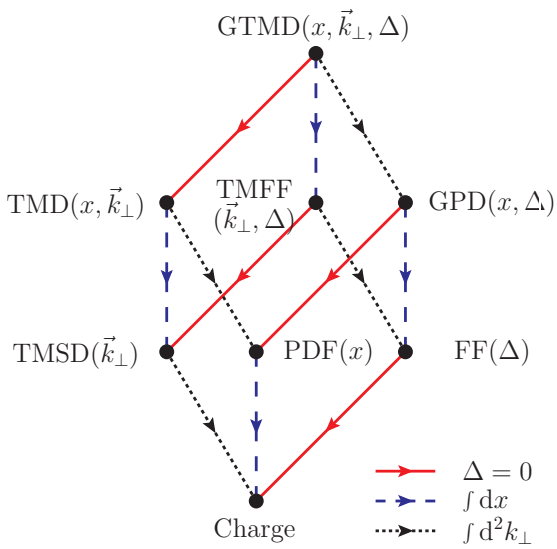

Fig. 2.6: Diagram of the different nucleon structure distributions [35]

This thesis however is focused on the latter, hard exclusive processes, but more information on TMD extraction from SIDIS processes is outlined in [36] and a full treatment of the objects in **Fig. 2.6** can be obtained in [35].

2.2.1 Hard Exclusive Processes

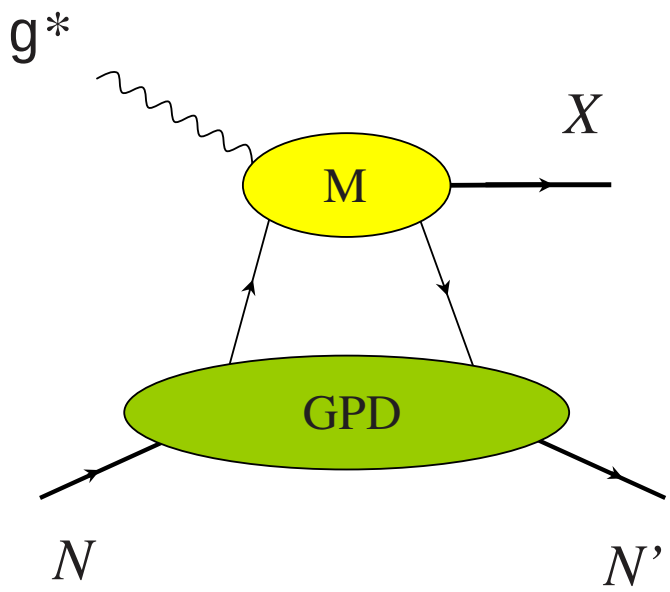

Fig. 2.7: Generic "hand-bag" diagram of deep scattering process [37]

Hard exclusive leptoproduction processes, shown in the generic schematic diagram of **Fig. 2.7**, are processes where a particle X, which could be some gauge boson (e.g. photon) or hadronic system (e.g. meson or jets), is produced through some mechanism M encoded in the Generalized Parton Distributions (GPDs) of the nucleon. These exclusive processes are characterized by their signature property of factorization: the reaction can be factored into a hard interaction between the virtual photon and a constituent quark, which can be calculated perturbatively, and a soft non-perturbative part that is parameterized by GPDs [38, 37]. The factorization process can be seen in **Fig. 2.8**, where the top half above the dashed line is the hard interaction between the virtual photon and struck quark and the bottom half is the nucleon which can be described by the GPDs.

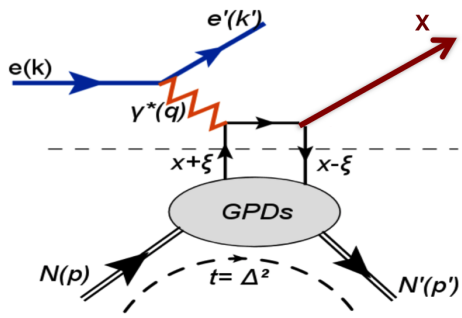

Fig. 2.8: Leading order generic "hand-bag" diagram of deep scattering process [4]

The process can be described as follows: the electron interacts with a quark from the nucleon via a single virtual photon exchange producing an additional particle X in the process before the struck quark is reabsorbed into the nucleon, which stays intact in the final state. These processes offer insights into the three-dimensional, tomographic, picture for the partons that make up the nucleon via GPDs since the GPDs hold the correlations between the partons' transverse spatial components (seen in **Fig. 2.9a**) and longitudinal momentum components (seen in **Fig. 2.9b**).

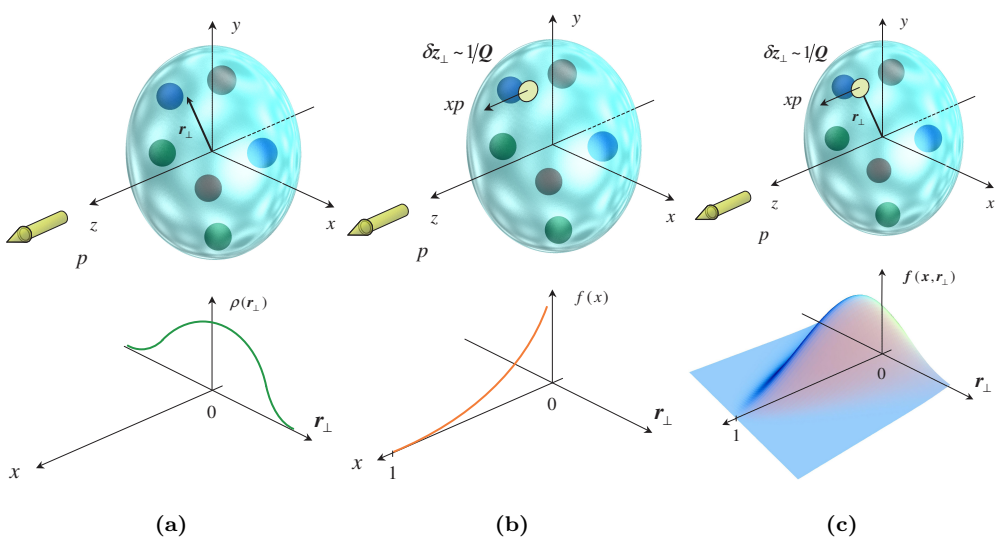

Fig. 2.9: Tomographic picture of GPDs [37]

2.2.1.1 Generalized Parton Distributions (GPDs)

The GPDs are complex mathematical objects that depend on the three variables x, ξ, and t, where, as seen in **Fig. 2.8**,

- $x+\xi$ is the nucleon's longitudinal momentum fraction carried by the struck quark;
- 2ξ is the fractional longitudinal component of Δ that is involved in the production of the particle X, often referred to as the skewness;
- Δ $(= p' - p)$ is the momentum transfer between the final and initial state of the nucleon; and
- t $(= \Delta^2)$ is the familiar Mandelstam variable;

that can be interpreted as a probability amplitude, for a given squared momentum transfer t, of striking a quark carrying a longitudinal momentum fraction of $x+\xi$ which returns to the nucleon (without breaking it) with longitudinal momentum fraction of $x-\xi$. The remaining 2ξ goes into the resulting produced photon or meson.

The GPDs can be expanded in the so-called twist expansion where each term of the expansion is in powers of $1/Q$ [39]. The twist n can be calculated as the difference between the dimension of nonlocal quark/gluon operator and its spin, which appears in the dominant term as M^{n-2}.

At leading twist, there are 8 GPDs for each quark flavor

- 4 helicity preserving or chiral-even $(E, \tilde{E}, H, \tilde{H})$ and
- 4 helicity flipping or chiral-odd $(E_T, \tilde{E_T}, H_T, \tilde{H_T})$.

that play a role in the hard exclusive electroproduction process off the nucleon.

2.2.1.2 Beam Spin Asymmetry (BSA)

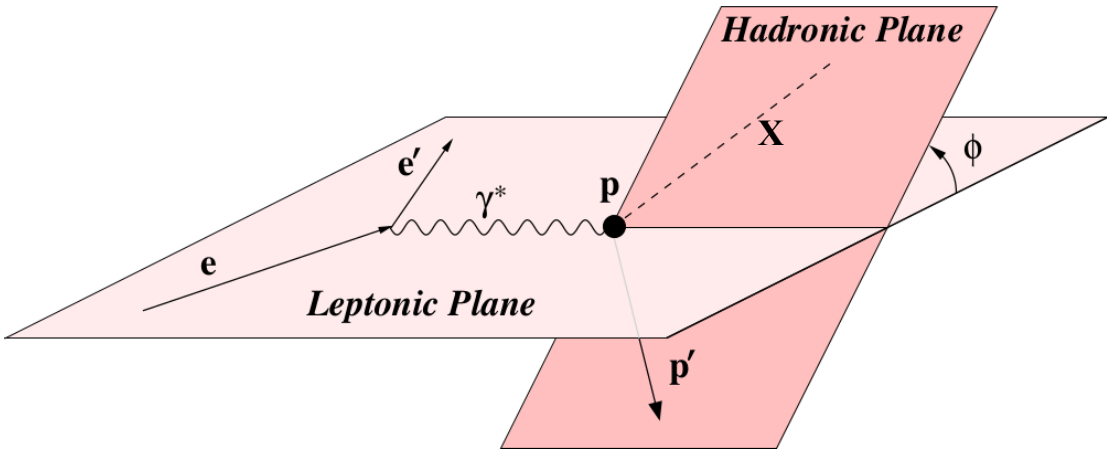

Fig. 2.10: Schematic of ϕ convention for generic hard exclusive process [40].

One approach to access these GPDs is to measure beam spin asymmetries (BSA) of these exclusive processes. First we introduce some convention and terminology needed to define and ultimately measure it.

A schematic of a generic hard exclusive electroproduction of a particle X off a target p is shown in **Fig. 2.10**, where the incoming electron (e) is scattered (e') off the target (p) via the virtual photon (γ^*), producing a particle X in the process. The incoming and outgoing electron form the scattering or leptonic plane, while the recoiling target p' and produced X form the reaction or hadronic plane. Following the Trento convention and fixing the leptonic plane with the virtual photon lying on the z-axis [41], ϕ is the angle between the two planes.

The virtual photon can be completely determined from the incoming and scattered electron – the four-momentum transfer Q^2, energy transfer ν, and polarization ϵ are

defined in the lab frame as:

$$\nu := E - E' \tag{2.6}$$

$$Q^2 := 4EE' \sin^2 (\theta_{e'}/2) \tag{2.7}$$

$$\epsilon := \left[1 + 2\frac{\nu^2}{Q^2} \tan^2 \frac{\theta_{e'}}{2}\right]^{-1} \tag{2.8}$$

where E, E' are the initial and final energy of the electron, respectively, and $\theta_{e'}$ is the scattered electron's lab frame polar angle.

For a longitudinally polarized (L) electron beam and unpolarized (U) target, the BSA A_{LU} is defined as

$$A_{LU} := \frac{d^4\sigma_+ - d^4\sigma_-}{d^4\sigma_+ + d^4\sigma_-} \quad . \tag{2.9}$$

Here $d^4\sigma^{\pm}$, the differential cross section with beam helcity ± 1, is shorthand for

$$d^4\sigma_{\pm} = \frac{d^4\sigma_{\pm}}{dQ^2 dx dt d\phi} = \frac{\Gamma}{2\pi} \left(\Sigma_{fi} \pm \Delta_{fi}\right)$$

where fi denotes the transition from the initial to final nuclear state and Γ, a phase space term, depends of Q^2, x and E

$$\Gamma\left(Q^2, x, E\right) := \frac{\alpha_{\mathrm{EM}}}{8\pi} \frac{Q^2}{m^2 E^2} \frac{1-x}{x^3} \frac{1}{1-\epsilon} \quad ,$$

with α_{EM} being the usual electromagnetic strength or coupling constant.

Respectively, the symmetric and antisymmetric terms, showing their explicit dependences,

$$\begin{aligned} \Sigma_{fi}\left(Q^2, x, t, \phi\right) &:= \sigma_T + \epsilon_L \sigma_L + \sqrt{2\epsilon_L\left(\epsilon + 1\right)}\sigma_{LT} \cos\phi + \epsilon \sigma_{TT} \cos 2\phi \\ \Delta_{fi}\left(Q^2, x, t, \phi\right) &:= \sqrt{2\epsilon_L\left(\epsilon - 1\right)}\sigma_{L'T} \sin\phi \end{aligned} \quad , \tag{2.10}$$

contain the so-called structure functions, σ_T, σ_L, σ_{LT}, σ_{TT}, and $\sigma_{L'T}$, which are functions of Q^2, x and t, that can be parametrized by the coupling of the longitudinal (L) and transverse (T) components of virtual photon to that of the GPDs.

Then the BSA, A_{LU}, is:

$$\begin{aligned} A_{LU} &= \frac{d^4\sigma^+ - d^4\sigma^-}{d^4\sigma^+ + d^4\sigma^-} = \frac{2\Delta_{fi}}{2\Sigma_{fi}} \\ &= \frac{\sqrt{2\epsilon_L(\epsilon-1)}\sigma_{L'T}\sin\phi}{\sigma_T + \epsilon_L\sigma_L + \sqrt{2\epsilon_L(\epsilon+1)}\sigma_{LT}\cos\phi + \epsilon\sigma_{TT}\cos 2\phi} \\ &=: \frac{\alpha\sin\phi}{1+\beta\cos\phi+\gamma\cos 2\phi} \end{aligned} \tag{2.11}$$

and the parameters to measure from experiment are then

$$\begin{aligned} \alpha &:= \left[\frac{\sigma_{L'T}}{\sigma_T+\epsilon_L\sigma_L}\right] \sqrt{2\epsilon_L(\epsilon-1)} \\ \beta &:= \left[\frac{\sigma_{LT}}{\sigma_T+\epsilon_L\sigma_L}\right] \sqrt{2\epsilon_L(\epsilon+1)} \qquad . \\ \gamma &:= \left[\frac{\sigma_{TT}}{\sigma_T+\epsilon_L\sigma_L}\right] \epsilon \end{aligned} \tag{2.12}$$

By measuring the BSA of various exclusive processes, we unlock and constrain different linear combinations of the 8 aforementioned GPDs [37]. For instance, measurements of the BSA for Deeply Virtual Compton Scattering (DVCS) off the free nucleon, discussed in the next section, are sensitive to the $H, \tilde{H}, E$ GPDs at leading twist.

These structure function relations to GPDs can be seen through helicity amplitude which depend on the helicity of the virtual photon (ν), produced particle (ν'), initial (μ) and final (μ') state target. The Goldstein-Gonzalez-Liuti (GGL)[42, 43] and Goloskokov-Kroll (GK) [44] models show similar expressions for the BSA in terms of these helicity amplitudes where the explicit relation to the GPDs is presented for different reactions. Still, the parameterization of the GPDs, particularly the chiral-odd ones, are very different:

- the GGL model relies on experimental measurements to constrain the not so well understood chiral-odd GPDs using symmetry arguments to parameterize them by linear relations to the chiral-even ones and

- the GK model makes some assumptions based on lattice QCD with the dominiant chiral-odd GPDs contributions being from H_T, $\widetilde{H_T}$, and E_T, where the latter two come in combinations of $\bar{E_T} := 2\widetilde{H_T} + E_T$, while other chiral-odd GPDs are neglible.

Two particular exclusive processes of interest to constrain these models and others are the previously mentioned DVCS and the Deeply Virtual Meson Production (DVMP) processes. A survey of previous work involving measurements of these processes is presented and discussed in the following sections.

2.2.2 Deeply Virtual Compton Scattering (DVCS)

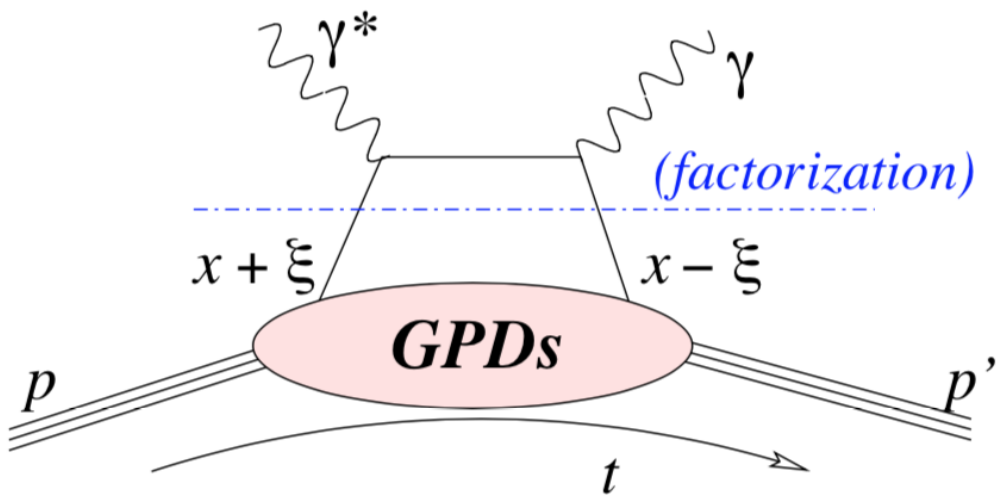

Fig. 2.11: "'Hand-bag" diagram of DVCS [45]

DVCS is the hard exclusive electroproduction of a real photon radiated by the struck quark of the nucleon (seen in **Fig. 2.11**). Factorization for the amplitude of this process has explicitly been proven in two independent calculations [46, 47].

For DVCS the leading twist is 2, while higher twists n are suppressed by powers of $(M/Q)^{n-2}$ [39], and so, as previously mentioned, DVCS is sensitive to the $H, \tilde{H}, E$ GPDs. Beam spin asymmetries have been extracted for a wide range of kinematic variables Q^2, x and t, organized into two-dimensional $\left(Q^2, x\right)$ bins [8, 45], shown in **Fig. 2.12**, in an effort to constrain these GPDs. From these measurements, we see that the models involving different GPD contributions decently, but not ideally, describe the data points.

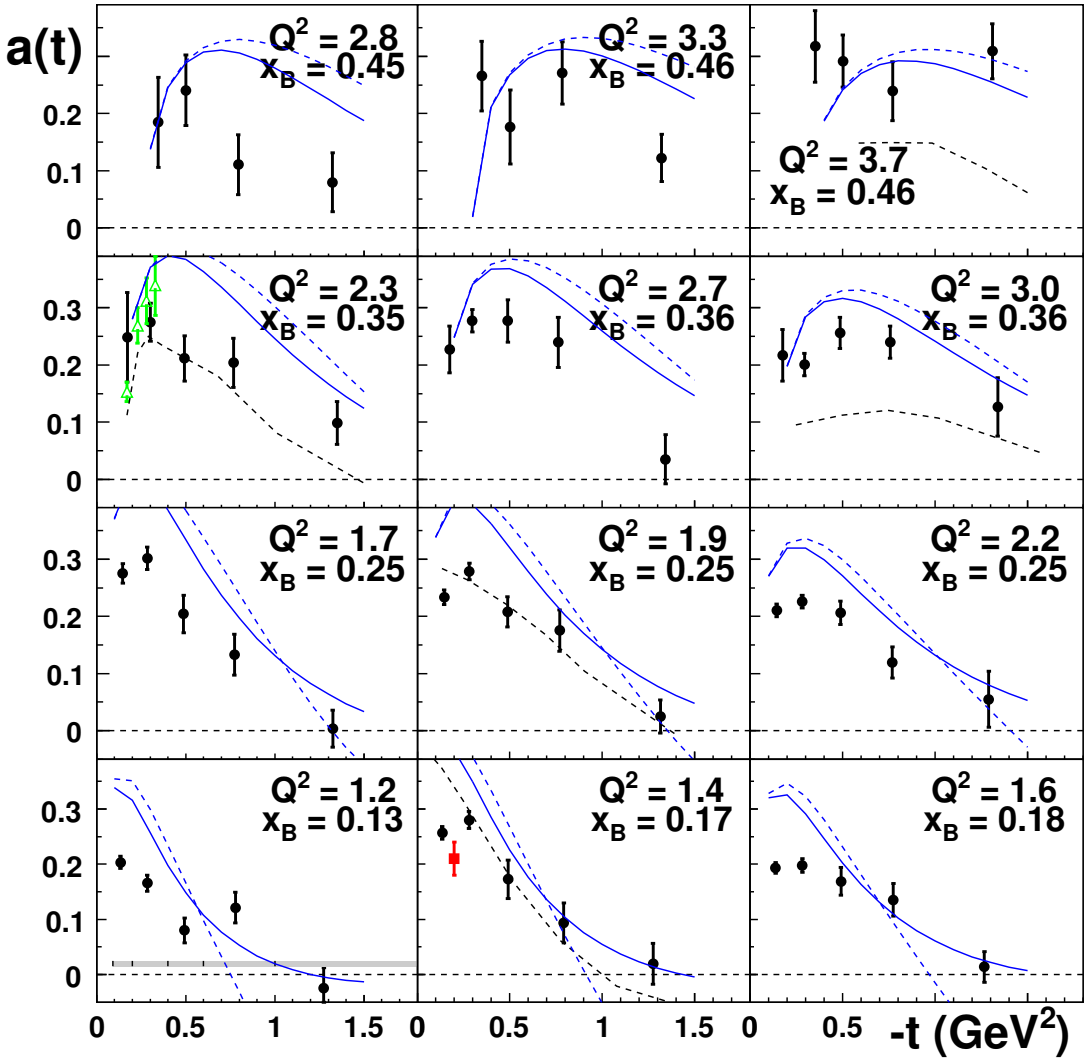

Fig. 2.12: DVCS BSA amplitudes $a(t)$ (BSA measured at $\phi = 90°$) in different bins of Q^2 and x (black points) [45], expanding on the previously measured values (in red and green points). The black dashed curves correspond to a Regge calculation [48]. The blue curves correspond to the GPD calculation described in [45], at twist-2 (solid) and twist-3 (dot-dashed) levels, with only the dominant GPD contribution from H.

2.2.3 Deeply Virtual Meson Production (DVMP)

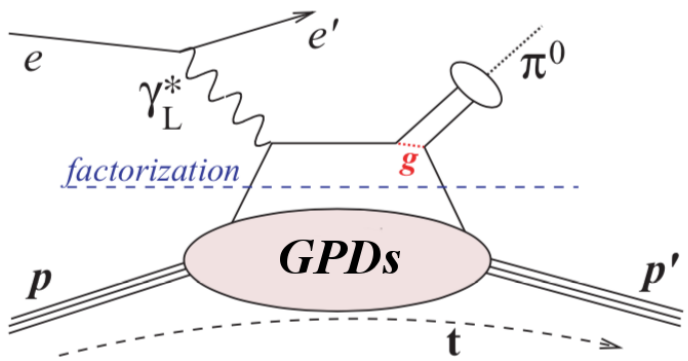

Fig. 2.13: "'Hand-bag" diagram of DVMP of π^0 [11]

While linear combinations of the chiral-even GPDs are relatively well constrained, the chiral-odd counterparts are not. Chiral-odd GPDs, which encode the transverse-spin structure of the nucleon, can be accessible via hard exclusive meson electroproduction [40]. This was made explicit when BSA measurements [11] showed that these contributions cannot be ignored. Moreover, BSA measurements for hard exclusive or Deeply Virtual Meson Production (DVMP) processes (see **Fig. 2.13**) have the distinct advantage of being able to sift out different flavor combinations of GPDs simply by "switching out" mesons. That is, extracting the BSA of a particular meson electroproduction process yields a particular flavor combination of GPDs, supporting an overall flavor decomposition of GPDs [37].

The cross section (and decomposition) as well as BSA measurements of DVMP on the free nucleon have also been extracted to constrain these transverse GPDs for

- the π^0 in [40] and [11], and

- the η in [49] and [12],

and are exhibited in **Figs. 2.14, 2.15** respectively, showing models are in good agreement with the data, particularly for the π^0.

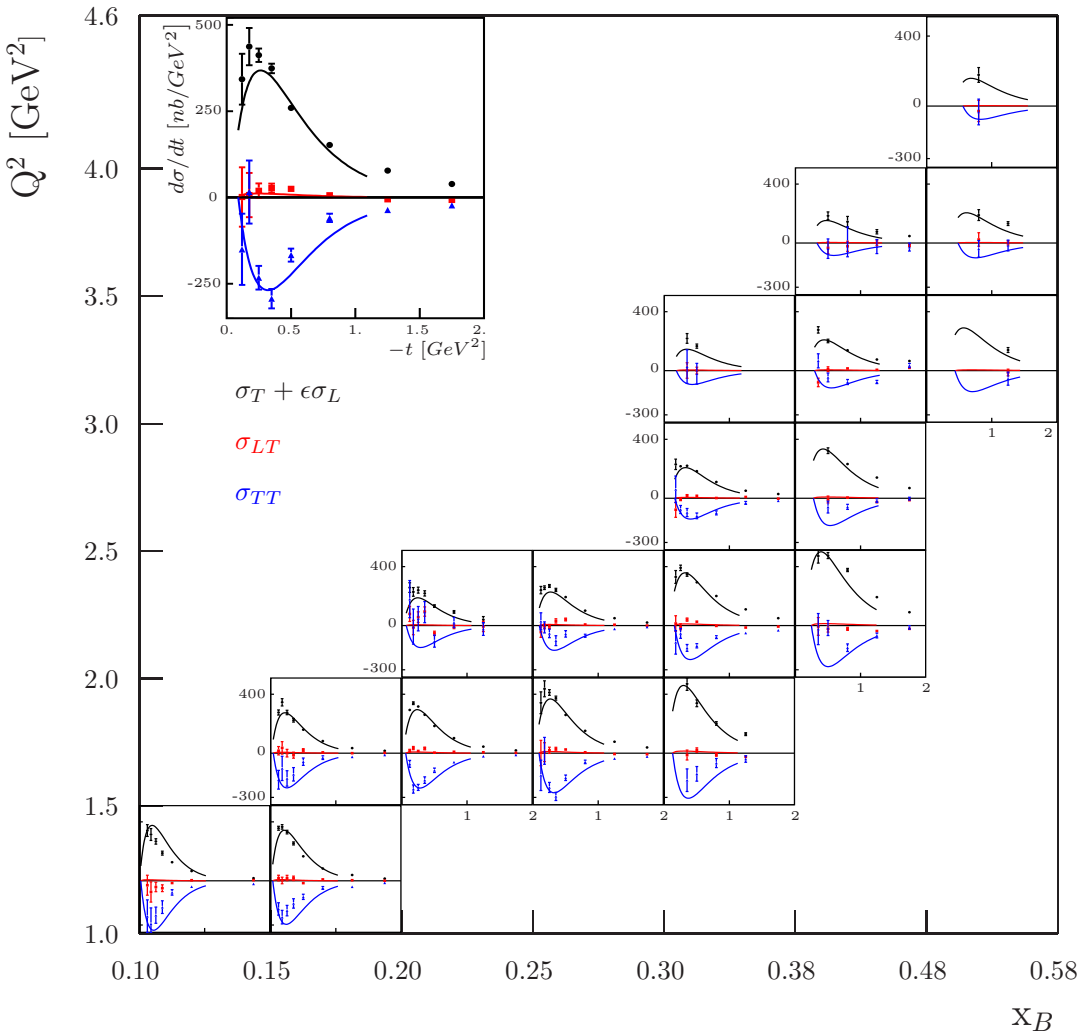

Fig. 2.14: DVMP of π^0 structure function components of cross section in different bins of (Q^2, x) for different combinations of the structure functions (see legend) [40]. The curves correspond to calculations done by [44] which are improvements over the Regge calculation [50] found in [40].

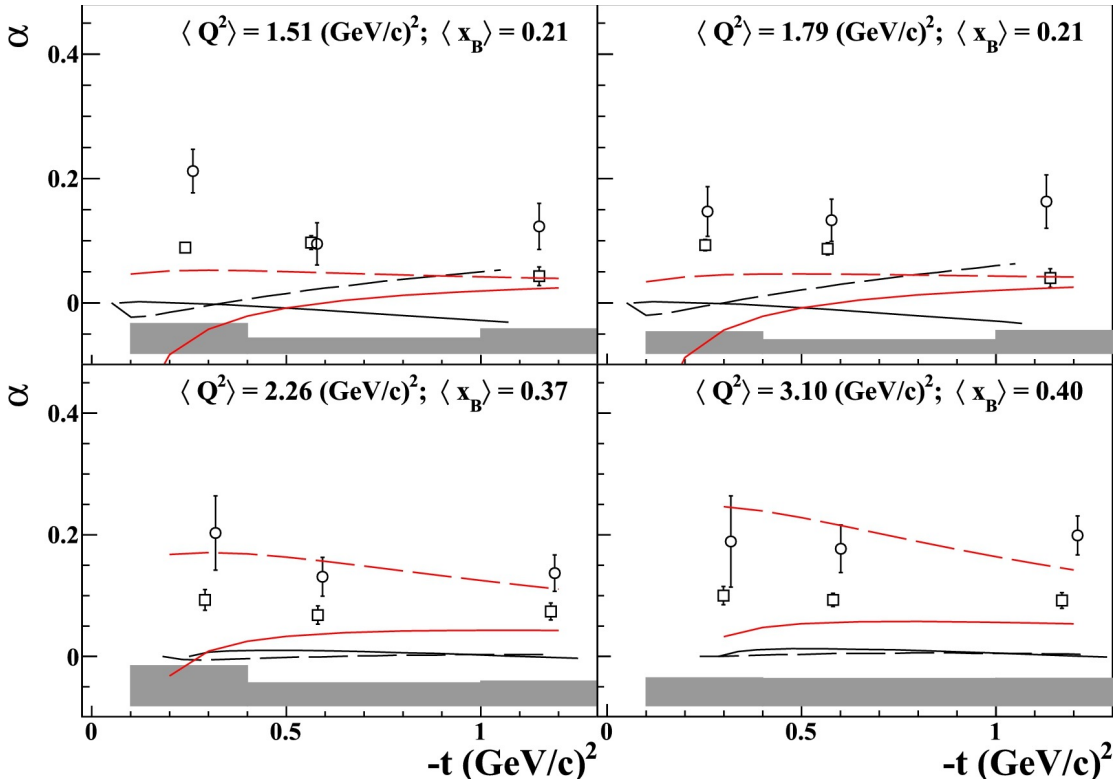

Fig. 2.15: DVMP of π^0 (squares) and η (circles) BSA amplitudes $\alpha(t)$ (measured at $\phi = 90°$) in different bins of $\left(Q^2, x\right)$ [12]. The curves show the calculations for π^0 (dashed) and for η (solid) from two independent GPD models [44] (in black) and [42] (in red).

2.3 Nuclear Targets

Nuclear targets for the same hard exclusive reactions offer an even richer prospect. The benefit is twofold: for a given target, there are two distinct channels for a reaction to occur. Namely, the coherent channel, where the exchanged virtual photon interacts with the target as a whole, and the incoherent channel, where the virtual photon interacts with a spin-1/2 nucleon that then breaks off and traverses the nuclear medium.

The coherent channel offers insights to how these hard exclusive processes occur on targets with different spin; the choice of the target, through its overall nuclear spin, determines what spin degrees of freedom are suppressed and/or enhanced in the exclusive reactions outlined previously. By looking at the same processes but with different targets in the coherent channel, we can explore different spin configurations to support and achieve a decomposition of the spin dependence.

The incoherent channel, on the other hand, offers a unique opportunity to show and quantify how the nuclear medium can modify the GPDs, which can give insight to the so-called EMC effect. This effect can be summarized as the modification to the reduced PDF (namely, F_2 per nucleon) for nuclear targets as compared to the deuteron. This was first demonstrated for iron by the European Muon Collaboration (EMC) through the measurement of the fractional momentum x dependence in the ratio

$$R_{EMC} = \left(\frac{F_2^A}{A}\right) / \left(\frac{F_2^D}{2}\right),$$

of reduced PDFs for nuclei with atomic number A to that of the deuteron D. The effect is seen as the slope of the ratio's x-dependence over the particular range $x \in (0.3, 0.7)$ [51]. This has since been investigated for a variety of different nuclei from different

collaborations and summarized in detail in [52]. The explicit A dependence can be seen in **Fig. 2.16** from the summary, where the effect scales linearly with $A^{-1/3}$ for heavier nuclei but falls off for light nuclei.

While this density dependent, confining nuclear effect is not so well understood, there are two leading candidates offering a possible explanation. One from mean field nuclear medium modifications where dynamical and emergent nuclear forces arise due to the nuclear density [53], wherein nuclear wavefunctions begin to overlap spatially, and another from short range correlations where a small percent of nucleons are correlated in pairs scatter off each other with momentum significantly above the fermi momentum [54, 55].

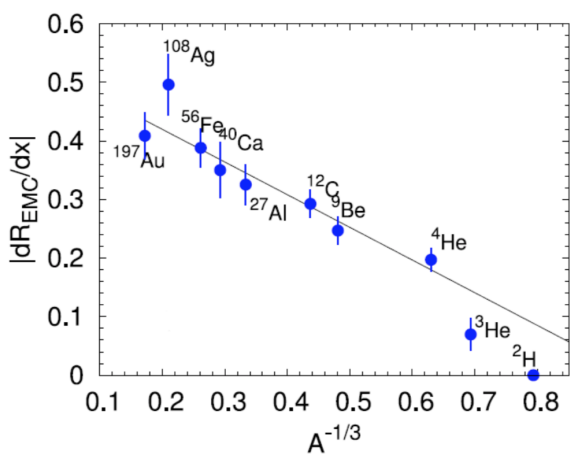

Fig. 2.16: EMC ratio dependence on $A^{-1/3}$ [52]

These competing ideas can benefit from, if not be reconciled with, more nuclear target experiments to measure nuclear structure (e.g. GPDs). In particular, the nuclear target of focus for this thesis is ^{4}He, which has the benefit of being a relatively simple symmetric spin-0 nuclear system.

2.3.1 Nuclear DVCS: DVCS off ^{4}He

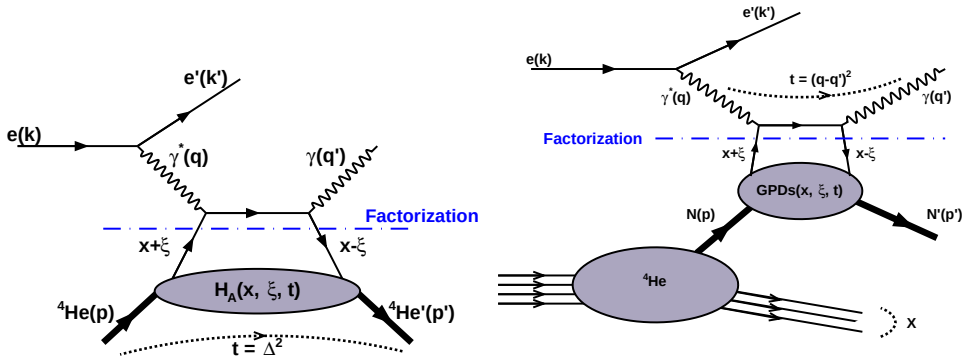

(a) Coherent channel [6] **(b)** Incoherent channel [7]

Fig. 2.17: Coherent and Incoherent DVCS off ^{4}He

Beam spin asymmetries for nuclear DVCS off ^{4}He has been extracted in both the coherent [6] and incoherent [7] channels to complement previous nucleonic DVCS BSAs [45]. The coherent channel BSAs (**Fig. 2.18**) are in agreement with theory calculations for DVCS off the spin-0 ^{4}He target [56] and led to the extraction of the so-called Compton Form Factors (CFFs) H_A shown in **Fig. 2.19** that parameterize the GPDs, also in agreement with current available models.

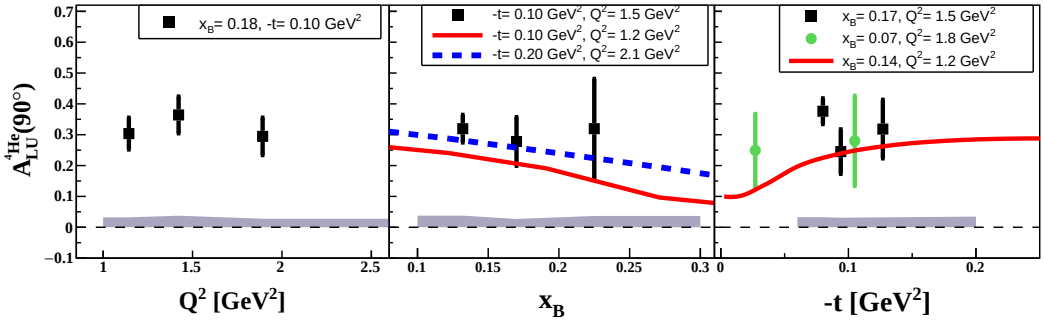

Fig. 2.18: Coherent DVCS: A_{LU} vs $\{Q^2, x, -t\}$ [6]

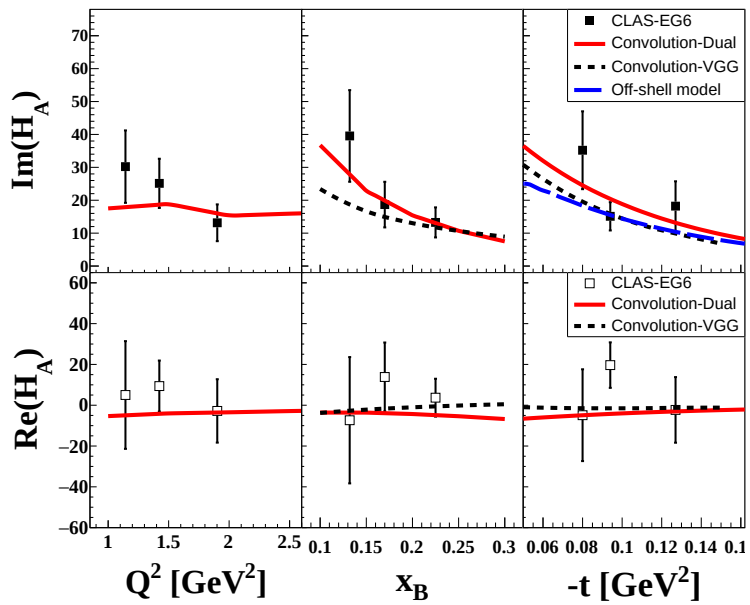

Fig. 2.19: Coherent DVCS: Real and imaginary parts of the CFFs vs $\{Q^2, x, -t\}$ [6]

DVCS in the incoherent channel results [7] showed a clear suppression of the extracted BSA (**Fig. 2.20**), as compared to DVCS off the free proton [45]. Further, they look to be independent of t over a sizable range which is not supported by current available models.

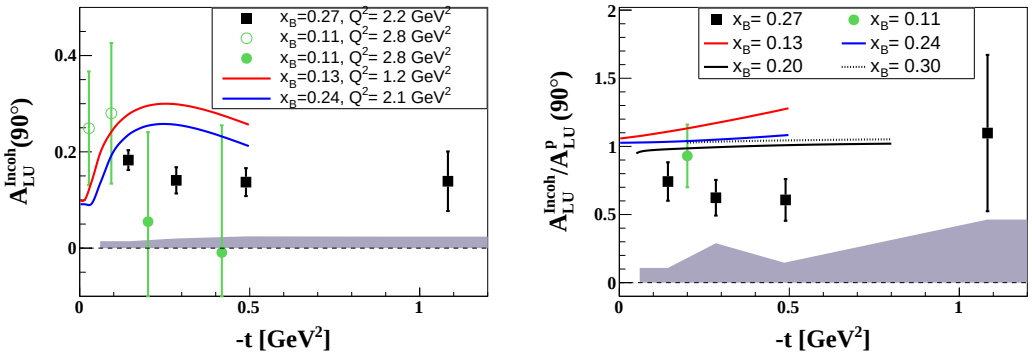

(a) A_{LU} vs $\{Q^2, x, -t\}$ [7]

(b) A_{LU} ratio of incoherent to proton [7]

Fig. 2.20: Incoherent DVCS: BSA measurements [7]

2.3.2 Nuclear DVMP: DVMP off ^{4}He

The subject of this thesis is nuclear DVMP of π^0 off ^{4}He, to offer complementary measurements to previously outlined nuclear DVCS off ^{4}He as well as to bridge the gap to nucleonic DVMP.

The goal is to establish BSA measurements in the coherent channel to have a strong foundation and to lay the path for future measurements of DVMP in the incoherent channel. The importance of the incoherent channel is to get at the nuclear medium modifications in a similar manner to the nuclear DVCS measurements, as to get at the contributions from the chiral-odd GPDs in the nuclear environment. Depending on which model, the incoherent DVπ^0P BSA is sensitive to [12]

- $\mathrm{Im}\left[< H_T >^* < \tilde{E} >\right]$ in the GK model and
- $\mathrm{Im}\left[< E_T >^* < \tilde{H} >\right]$ in the GGL model.

But before making meaningful measurements in the incoherent channel, the coherent channel is first pitted against theoretical predictions. The rest of this thesis will be presenting the work leading up to this measurement in the coherent channel with results and discussion in the concluding chapters.

First however, we will take a step back from the discussion of GPDs and outline a recent result where the DVπ^0P off ^{4}He is generalized to the electroproduction process of pseudoscalar mesons off scalar targets. The BSA prediction from this formalism and its consequences can then be analyzed in the scope of GPDs.

Chapter 3

Electroproduction of Pseudoscalar Mesons off Scalar Targets

3.1 Theoretical Prediction

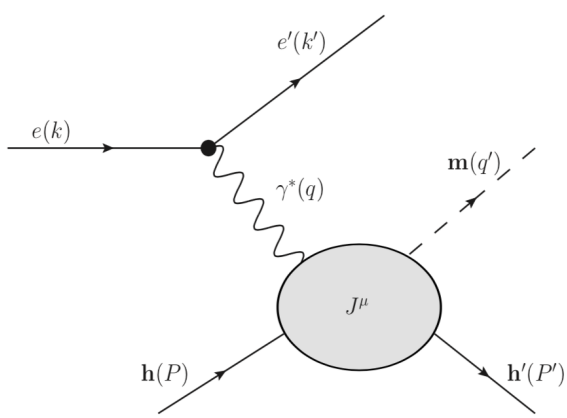

Fig. 3.1: Diagram of meson electroproduction, m, where the incoming electron interacts with a hadron via the virtual photon γ^* [2].

Most generally, without fixing the leptonic plane, the electroproduction differential cross section can be written as

$$d\sigma = \frac{d^5\sigma}{dydxdtd\phi_{k'}d\phi_{q'}} = \left[\frac{1}{(2\pi)^5}\frac{xy}{32Q^2\sqrt{1+\left(\frac{2Mx}{Q}\right)^2}}\right]\left\langle|\mathcal{M}_\lambda|^2\right\rangle$$

with the usual kinematic variables being, given the particles 4-momenta defined in **Fig. 3.1** and M being the target's mass,

$$\begin{aligned} Q^2 &:= -q^2 \\ x &:= Q^2/\left(2P\cdot q\right) \\ t &:= \left(P-P'\right)^2 \\ y &:= P\cdot q/P\cdot k \end{aligned} \quad , \tag{3.1}$$

where y is the fractional energy transferred from the electron to the virtual photon and $\phi_{k',q'}$ are the azimuthal angles of the scattered electron and produced meson with respect to the virtual photon, respectively.

The Lorentz invariant transition amplitude $\mathcal{M}_\lambda$ for beam helicty $\lambda \in \{\pm 1\}$ is obtained by the contraction of the leptonic and hadronic current tensors:

$$\left\langle \left|\mathcal{M}_\lambda\right|^2 \right\rangle = \left(\frac{e^2}{q^2}\right)^2 \mathcal{L}_\lambda^{\mu\nu}\mathcal{H}_{\mu\nu} \quad .$$

The hadronic tensor, $\mathcal{H}_{\mu\nu}$, can be expressed in terms of the hadronic currents, J_μ:

$$\mathcal{H}_{\mu\nu} = J_\mu^\dagger J_\nu$$

and the leptonic tensor, $\mathcal{L}_\lambda^{\mu\nu}$, can be expressed as:

$$\mathcal{L}_\lambda^{\mu\nu} = q^2\Lambda^{\mu\nu} + 2i\lambda\epsilon^{\mu\nu\alpha\beta}k_\alpha k'_\beta \quad ,$$

with

$$\Lambda^{\mu\nu} = g^{\mu\nu} + \frac{2}{q^2}\left(k^\mu k'^\nu + k'^\mu k^\nu\right) \quad .$$

Contracting the two tensors, under a single-photon exchange, gives a general but explicit expression for the transition amplitude:

$$\left\langle |\mathcal{M}_\lambda|^2 \right\rangle = \left(\frac{e^2}{q^2}\right)^2 \left[\frac{2q^2}{\epsilon - 1} \langle |\tau_{fi}| \rangle^2 + 2i\lambda\epsilon^{\mu\nu\alpha\beta} k_\alpha k'_\beta J^\dagger_\mu J_\nu\right] \tag{3.2}$$

where the symmetric term of the squared transition amplitude is

$$\begin{aligned} \langle |\tau_{fi}| \rangle^2 = \quad & \frac{1}{2}\left(|H_x|^2 + |H_y|^2\right) + \frac{\epsilon}{2}\left(|H_x|^2 - |H_y|^2\right) + \epsilon_L |H_z|^2 \\ & -\sqrt{\frac{1}{2}\epsilon_L (1+\epsilon)} \left(H_x^* H_z + H_z^* H_x\right) \end{aligned},$$

with H_i being the spatial components of the hadronic current J_i, the virtual photon polarization term being

$$\epsilon = \frac{\Lambda^{xx} - \Lambda^{yy}}{\Lambda^{xx} + \Lambda^{yy}} = -\frac{2M^2x^2y^2 + 2Q^2(y-1)}{2M^2x^2y^2 + Q^2(y^2 - 2y + 2)}$$

and its longitudinal component $\epsilon_L := \frac{Q^2}{\nu^2}\epsilon$. A direct measureable can be obtained from the beam spin asymmetry. For the interaction between longitudinally (denoted L) polarized electrons and an unpolarized (denoted U) target, the beam spin asymmetry (BSA), A_{LU}, is defined as:

$$A_{LU} := \frac{d^5\sigma_+ - d^5\sigma_-}{d^5\sigma_+ + d^5\sigma_-} \equiv \frac{\left\langle |\mathcal{M}_+|^2 \right\rangle - \left\langle |\mathcal{M}_-|^2 \right\rangle}{\left\langle |\mathcal{M}_+|^2 \right\rangle + \left\langle |\mathcal{M}_-|^2 \right\rangle} \tag{3.3}$$

where $d^5\sigma_\pm$ and $\left\langle |\mathcal{M}_\pm|^2 \right\rangle$ are the differential cross sections and squared-transition amplitudes with positive or negative beam helicity, respectively.

From **Eq. 3.2**, we see that the BSA separates the part that is symmetric under exchange of μ and ν with the asymmetric part (denominator and numerator of A_{LU}, respectively). For coherent π^0 production, to first order there is no interference from the any other competing process, thus the BSA measures any asymmetry in the hadronic tensor (i.e. if $\mathcal{H}^{\mu\nu} \neq \mathcal{H}^{\nu\mu}$).

In a general single-photon exchange formulation, the hadronic current from the electroproduction of pseudoscalar (PS) mesons off scalar targets, J^{μ}_{PS}, can be expressed with just a single form factor F_{PS} [2]:

$$J^{\mu}_{PS} = F_{PS}\epsilon^{\mu\nu\alpha\beta}q_{\nu}\bar{P}_{\alpha}\Delta_{\beta}$$

where the form factor, F_{PS}, depends only on the Lorentz invariant variables, Q^2, x, and t defined in **Eq. 3.1**; $\bar{P} := P + P'$; and $\Delta := P - P' = q - q'$.

By symmetry, under this formulation, the BSA should then be identically zero:

$$A_{LU} \sim \mathcal{L}^{\mu\nu}_{+}\mathcal{H}_{\mu\nu} - \mathcal{L}^{\mu\nu}_{-}\mathcal{H}_{\mu\nu} \equiv 0$$

since $\mathcal{H}_{\mu\nu}$ is symmetric,

$$\begin{aligned}\mathcal{H}_{\mu\nu} &= J^{\dagger}_{\mu}J_{\nu} \\ &= |F_{PS}|^2\,\epsilon_{\mu\alpha\beta\gamma}\epsilon_{\nu\alpha'\beta'\gamma'}q^{\alpha}\bar{P}^{\beta}\Delta^{\gamma}q^{\alpha'}\bar{P}^{\beta'}\Delta^{\gamma'} \\ &= \mathcal{H}_{\nu\mu}\end{aligned}$$

and is contracted to the antisymmetric Levi-Civita tensor $\epsilon^{\mu\nu\alpha\beta}$ from the leptonic tensor.

Therefore, the measurement of the BSA obtained from this analysis will directly test and provide an important benchmark measurement for the general formulation of the hadronic tensor, outlined in [2]. A zero BSA measurement can be used to provide constraints to the GPD formulation, whereas a nonzero BSA will show sensitivity to effects beyond the single-photon exchange and other non-leading order effects where internal degrees of freedom are not neglible. From this benchmark measurement, this study can then be extended to look into the incoherent channel where the symmetry arguments certainly no longer hold.

3.2 Measuring the Beam Spin Asymmetry

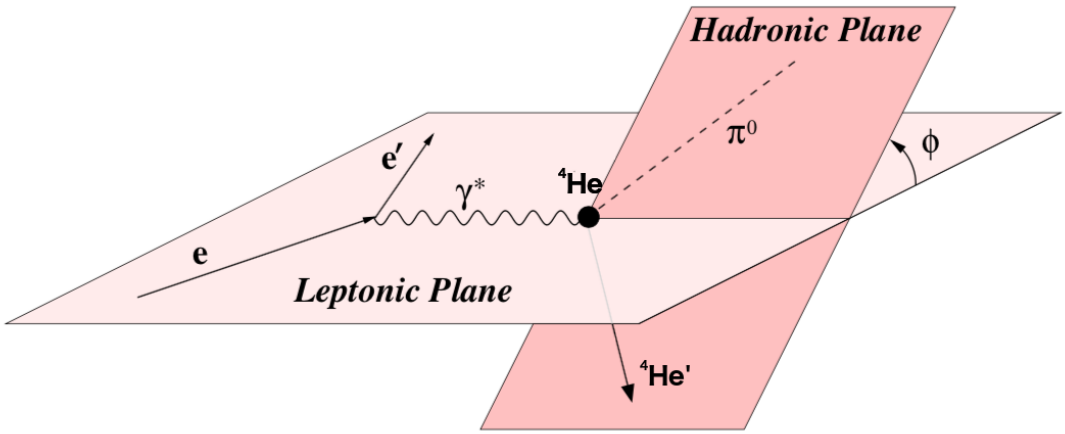

Fig. 3.2: Coherent DVMP on ^{4}He [40].

A schematic of coherent π^0 electroproduction off ^{4}He is shown in **Fig. 3.2**. If in fact A_{LU} is nonzero, it would be more useful to reexpress the BSA to be in-line with **Eq. 2.11**, following the Trento convention [41], where ϕ being the azimuthal angle between the two planes in relation to the virtual photon in the z-direction, calculated as the difference between $\phi_{k'}$ and $\phi_{q'}$. This way, a measurement of the variation in ϕ of the asymmetry can be made as to extract its amplitude.

Then the BSA, A_{LU}, is:

$$A_{LU} = \frac{\alpha \sin\phi}{1 + \beta\cos\phi + \gamma\cos 2\phi} \tag{3.4}$$

where the parameters, are shown in **Eq. 2.12**. In particular, a measurement A_{LU} $(\phi = 90°)$ will isolate the contributions involving the polarized structure function $\sigma_{L'T}$, directly

measuring

$$A_{LU}\left(90^{\circ}\right)=\frac{\sqrt{2\epsilon_L\left(\epsilon-1\right)}\sigma_{L'T}}{\sigma_T+\epsilon_L\sigma_L-\epsilon\sigma_{TT}}$$

These structure functions, in an analogous way to [43] and [44], can be expressed as (nuclear) helicity amplitudes that depend on the helicities of the virtual photon (ν), the produced π^0 ($\nu' \equiv 0$), the initial and final state target (μ and μ', respectively). Again, the advantage of the coherent channel here is that from the spin-0 target, there is no longer the notion of a helicity flip in the target as a whole. If we can decompose the target into some mixture of nucleonic helicity amplitudes, only non-helicity flip and even number helicity flip contributions can enter in, since the final state target is still ^{4}He.

Certainly, modifications to the nucleons' GPDs can be measured in the incoherent channel, where the spin flip contributions are not suppressed, but also possible is analogously parameterizing the nuclear helicity amplitudes in terms of nuclear GPDs. These nuclear GPDs can be constrained with this BSA measurement.

Chapter 4

CLAS EG6 Experimental Setup

Since particle identification of the electron, helium, and photons are required for exclusive DVπ^0P, this experimental setup section will only focus the detectors involved in identifying these particles and the systems involved in preparing the initial state particles (the accelerator and target). The rest of the detectors, all pictured in **Fig. 4.1b**, will be omitted as many of them are fully described in other theses and papers [4, 5, 9].

4.1 Existing CEBAF and CLAS

4.1.1 Continuous Electron Beam Accelerator Facility (CEBAF)

CEBAF is capable of delivering a continuous longitudinally polarized 6 GeV electron beam with beam current up to 150 nA. Polarized electrons start at the polarized photocathode injector with 67 MeV and are accelerated through 5 successive orbits of CEBAF, pictured in **Fig. 4.1a**, to achieve energies up to 6.064 GeV with up to 85% longitudinal polarization [4]. The beam is delivered to three experimental halls, A, B, and C end stations where different detectors are set up for various experiments.

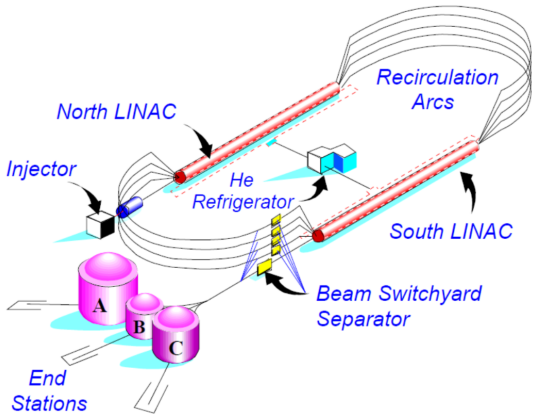

(a) CEBAF layout [4]

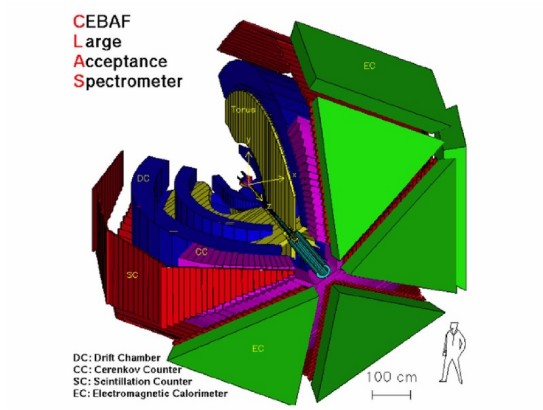

(b) Color-coded GEANT simulation view of CLAS [4]

Fig. 4.1: CEBAF (a) and CLAS (b) [4]

4.1.2 CEBAF Large Acceptance Spectrometer (CLAS)

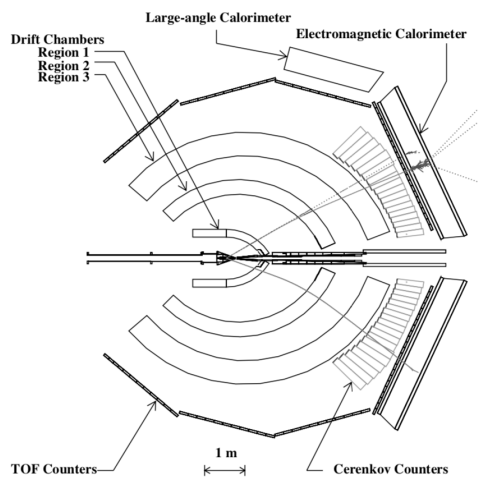

(a) CLAS profile

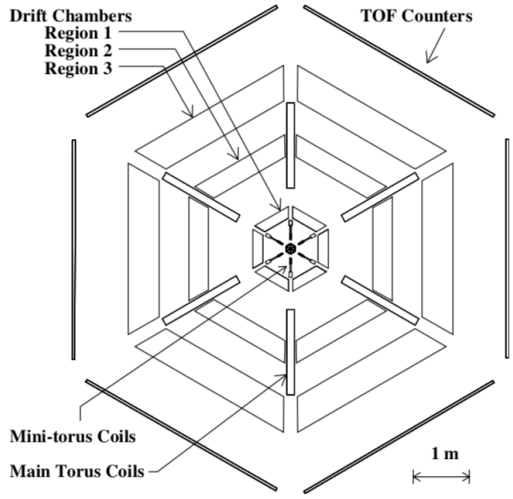

(b) CLAS face

Fig. 4.2: Schematic view of CLAS [57]

CEBAF delivered 120 nA of polarized electron beam to Hall B, where CLAS is housed, for the EG6 experiment achieving a luminosity of 10^{34} cm^{2}s^{-1} . The CLAS

detector array was designed to track and identify particles with a large 4π solid-angle coverage for high acceptance [57]. The hexagonal face of CLAS is conveniently divided into 6 azimuthal (with respect to the beam axis) triangular sectors as shown in **Fig. 4.2b**. The relevant parts that made up CLAS are described in the following subsections.

4.1.2.1 Superconducting Torus Magnet

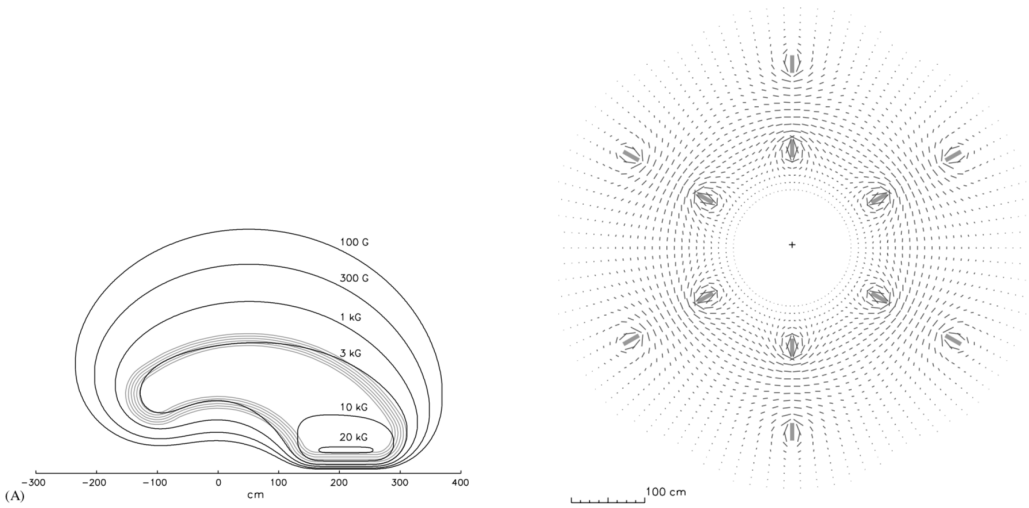

(a) Magnetic field map profile view

(b) Magnetic field map face view

Fig. 4.3: Torus magnet's field maps [57]

To accurately measure the momentum of charged particles, a strong magnetic field is needed to bend the trajectories of the scattered charged particles so that the radius of curvature can be extracted. A quick Lorentz force calculation determines the particles momentum, p in GeV:

$$p = 0.3qBR \tag{4.1}$$

where q is the particle's charge in units of elementary charge e (sign and charge tell whether the particle bends away or toward the beam-line), $B[T]$ is the applied magnetic field, and $R[m]$ is the radius of curvature.

4.1.2.2 Drift Chambers (DC)

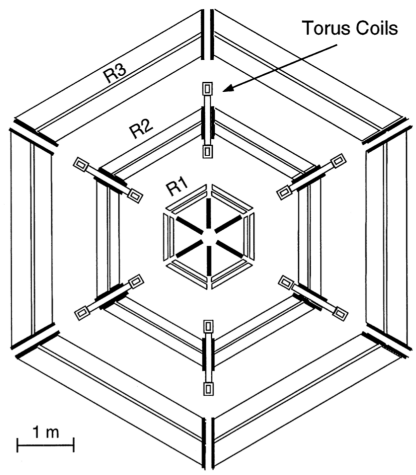

Fig. 4.4: The torus embedded inside the DC, extending from the 2nd DC region to 3rd [58].

In order to take full advantage of the bending fields produced by the torus magnet, the drift chambers allows for track reconstruction. The DC, with angular coverage of 8° to 154°, is comprised of three regions, in succession of radial distance from the target, filled with a 90% argon-10% CO_2 ionizing gas mixture and interwoven with sense wires hexagonally surrounded by field wires [58]. As particles traverse the gas mixture, the particle ionizes the gas along its path, and the ionized electrons are accelerated from the nearby field wires to their neighboring sense wires. A series of registered sense wire hits are strung together with drift times and distance of closest approach (DOCA) to determine the path of the particle (see **Fig. 4.5**).

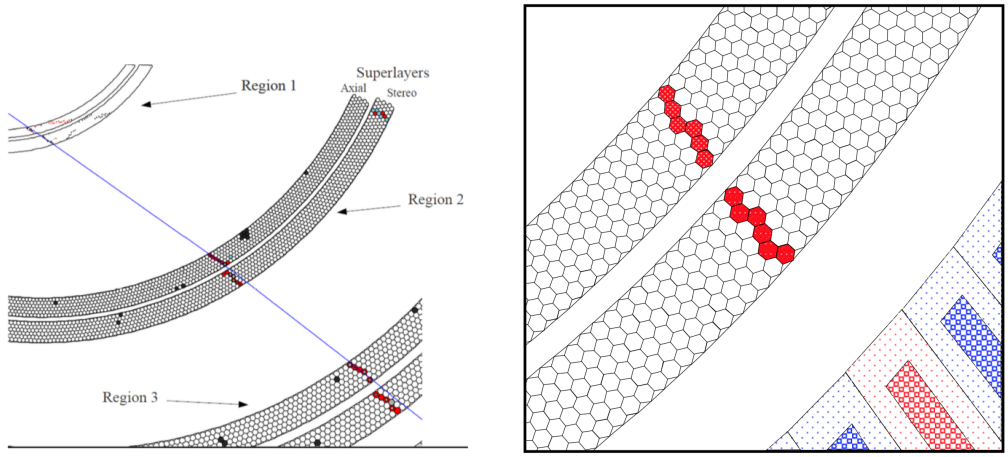

(a) Simulated track of particle traversing drift region (blue), triggering sense wires cells (red)

(b) Zoomed in of sense wires with red hexagonal cells representing hit

Fig. 4.5: DC track [57, 10, 6]

The negatively (positively) charged particle is bent toward (away from) the beam axis, under the influence of the toroid magnet's magnetic field. The bent track is fitted and the radius of curvature is measured to determine the charged particle's momentum via **Eq. 4.1**.

Overall, the DC achieves resolutions:

Variable	**Value**	**Units**
$\delta p/p$ (@1 GeV/c)	1.5	%
$\delta\theta$	1	mrad
$\delta\phi$	4	mrad

Table 4.1: DC resolutions

4.1.2.3 Time of Flight Scintillation Counters (SC)

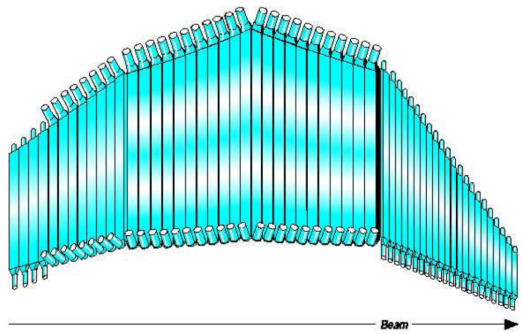

Fig. 4.6: Profile view of a sector of the SC: Pictured are the 57 scintillator strips and PMTs on each end of the strips. [4]

The SC provides timing information with the scattered electron as the trigger, using its time as the reference time. Paired together with the path length from the target, a particle's velocity can be determined. Connecting this timing information together with the momentum from the DC, the mass can be inferred.

The SC is equipped with 57 Bicron BC-408 scintillator strips with a magnetically shielded photomultiplier tube (PMT) on each end of the strip. The configuration in **Fig. 4.6** allows for timing resolutions between 120 and 250 ps depending on the kinematics, which is well below the needed timing resolution of 300 ps to separate out pions, kaons, and protons with momenta up to 2.5 GeV/c [4].

Variable	**Values**	**Units**
δt	$\in [120, 250]$	ps

Table 4.2: SC Resolutions [4]

4.1.2.4 Electromagnetic Calorimeter (EC)

The electromagnetic calorimeter is a sampling calorimeter with alternating layers of lead-scintillating material (see **Fig. 4.7**), with a lead:scintillator thickness ratio of 0.2. The EC measures energy deposited by particles with a polar angle coverage of 8° to 45° [59]. A particle impinges the EC and produces a shower that deposits its energy into both the insensitive lead and sensitive scintillating material. The EC is designed so that about a third of the energy is deposited into the scintillating material*.

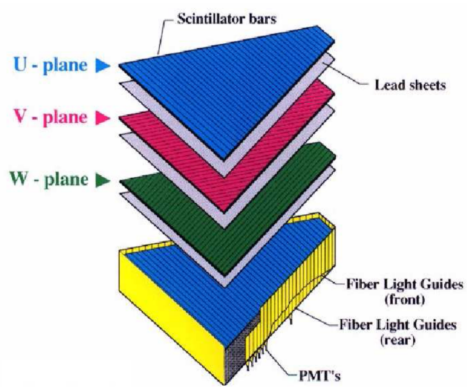

Fig. 4.7: The layers of the EC [4]

Additionally, the layers are arranged so that the scintillating bars of each successive layer are parallel to each of the three sides of the sector's equilateral triangle (see **Fig. 4.7**). This coordinate system, with positions u, v, and w, allows for reconstruction of the particle's position, as can be seen in **Fig. 4.8**. Ultimately, since photon trajectories are not affected by magnetic fields, the photon's momentum vector can be inferred.

* Calibration of this fraction is discussed in **Appendix B.3.1**.

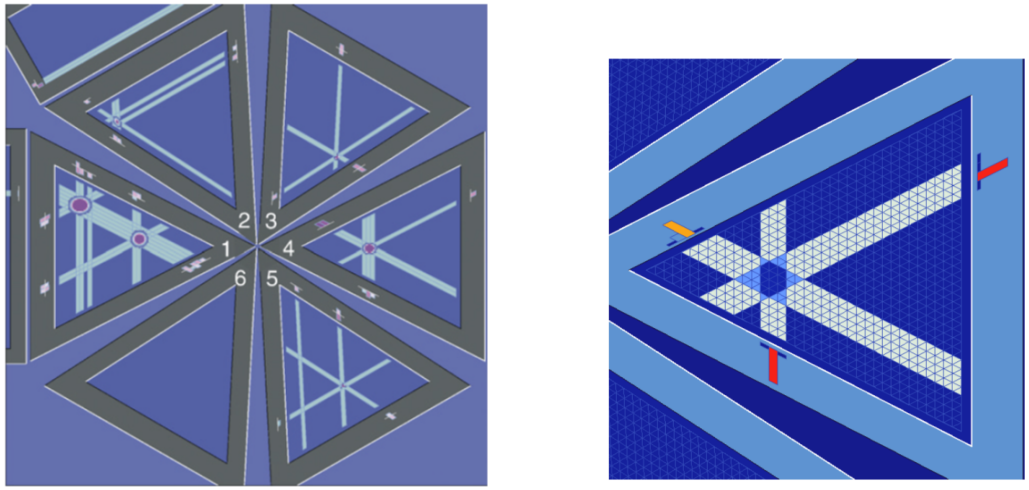

(a) Hits in the EC

(b) Sector view of EC hit

Fig. 4.8: EC hits [57, 10]: The strips that are hit are highlighted in light blue, showing that the position of the initial hit in the EC in red

The EC is able to achieve position, timing, and energy resolutions listed in **Table 4.3**. These resolutions together give a percent mass resolution below the 15% needed to distinguish π^0 and η in two-photon decays.

Variable	**Value(s)**	**Units**
$\delta E/E$ (@1GeV)	< 10	%
δx	2	cm
δt	1	ns
$\delta m/m$	< 15	%

Table 4.3: EC Resolutions [4]

4.2 EG6 Defining Features and Upgrades

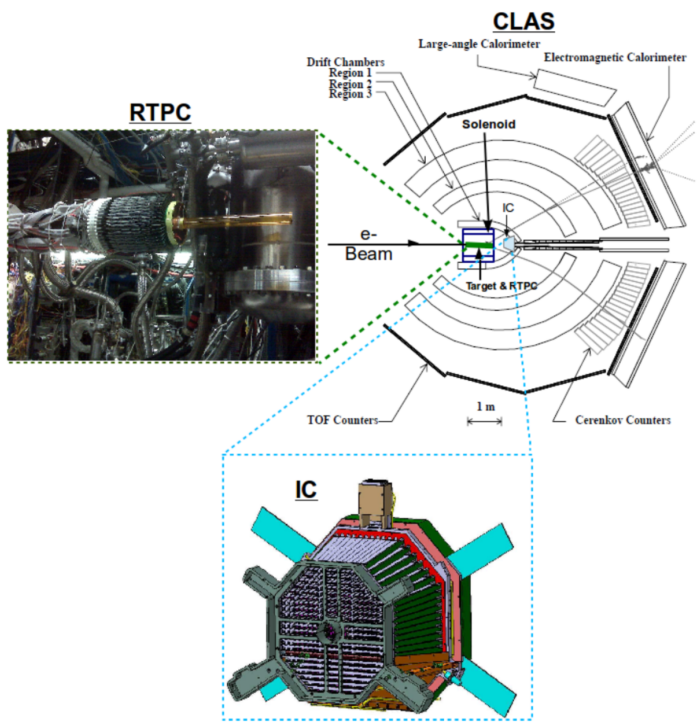

Fig. 4.9: The defining upgrades to the CLAS EG6 experiment [4]

In order to make a fully exclusive DVCS or DVMP measurement in the coherent channel, the topic of this study, additional components (detectors) were addd to the CLAS baseline detectors. These will be discussed in the following subsections.

4.2.1 Target

The first defining feature of CLAS EG6 is the target. The target, very similar to the previous CLAS EG4 experiment BoNuS, is a fixed ^{4}He gas target held at 6 atm. The cylindrical target, 6 mm in diameter and 200 mm in length, is enclosed by an insulating 27 μm thick Kapton film cylinder with end-cap windows of 15 μm thick aluminum [5].

4.2.2 Inner Calorimeter (IC)

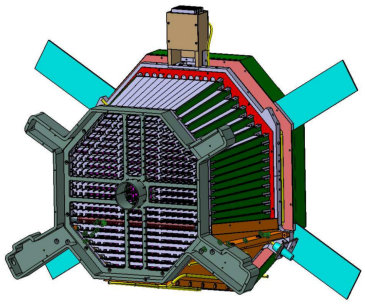

Fig. 4.10: The IC represented in GEANT [10]

Variable	Values	Units
$\delta E/E$	$\in [3,4]$	%
$\delta\theta$	$\in [3,5]$	mrad
$\delta\phi$	$\in [3,5]$	mrad

Table 4.4: IC resolutions [4] (for $E \in [2,5]$ GeV)

The IC, a part of a 2005 upgrade for the CLAS E1-DVCS experiment [60], shown in **Fig. 4.10**, allows for the measurement of the low-polar-angle photons that would otherwise never make it to CLAS: the EC is only sensitive to photons with polar angle between 8° and 45°. The need of coverage below 8° required by the kinematics of DVCS was addressed by the installation of the IC to cover polar angles between 5° and 15°. Incidentally, DVMP of the π^0 also requires the same angular coverage. Unlike the EC, the IC is outfitted with a projective array of 424 lead-tungstate ($PbWO_4$) crystals (see **Fig. 4.12**). This construction allows for improved resolutions given in **Table 4.4**.

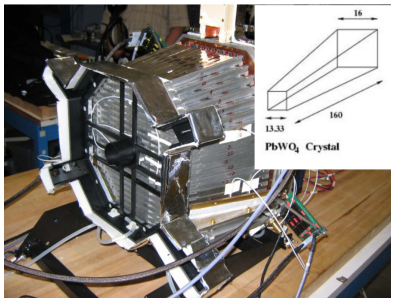

Fig. 4.11: The IC with dimensions in mm [5]

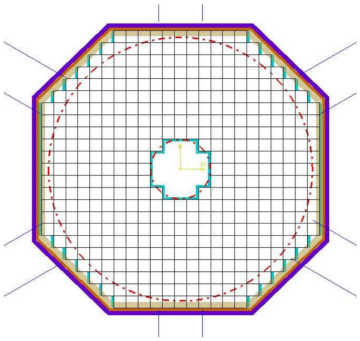

Fig. 4.12: Schematic of crystal array for IC[10]

4.2.3 Solenoid Magnet

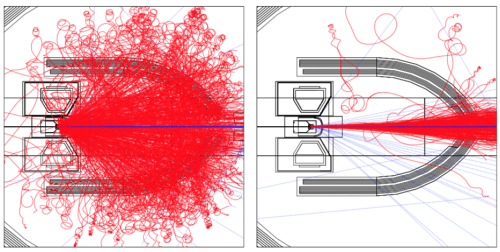

Fig. 4.13: Simulated Møller electrons in red with (right) and without (left) the solenoid field [4].

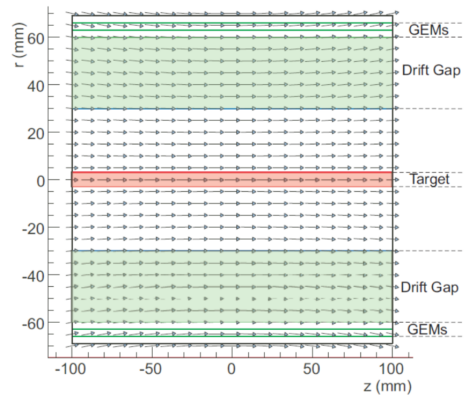

Fig. 4.14: Magnetic field map in the RTPC produced by the solenoid [4]

The use of the solenoid magnet, which produces a 4.5 T, essentially uniform, magnetic field parallel to the beam-line around the target, is two-fold. First, the solenoid magnet sends the low-lying, low-energy Møller electrons, produced at the target, spiraling down the beam-line, heavily reducing the contamination of the electrons of interest, as displayed in **Fig. 4.13** from simulation. Second, the solenoid magnet produces a magnetic field, shown in **Fig. 4.14**, that bends the path of the recoiled nuclei in the target to allow determination of its radius of curvature and, ultimately, its momentum. The beam, solenoid, and torus configurations are listed in **Table 4.5**.

Beam Energy [GeV]	Beam Current [nA]	Torus Current [A]	Solenoid Current [A]
1.204	150	2100	450
1.269	100	1900	450
5.700	100	1900	450
6.064	120-150	2100	450

Table 4.5: EG6 Run Configurations [4]

4.2.4 Radial Time Projection Chamber (RTPC)

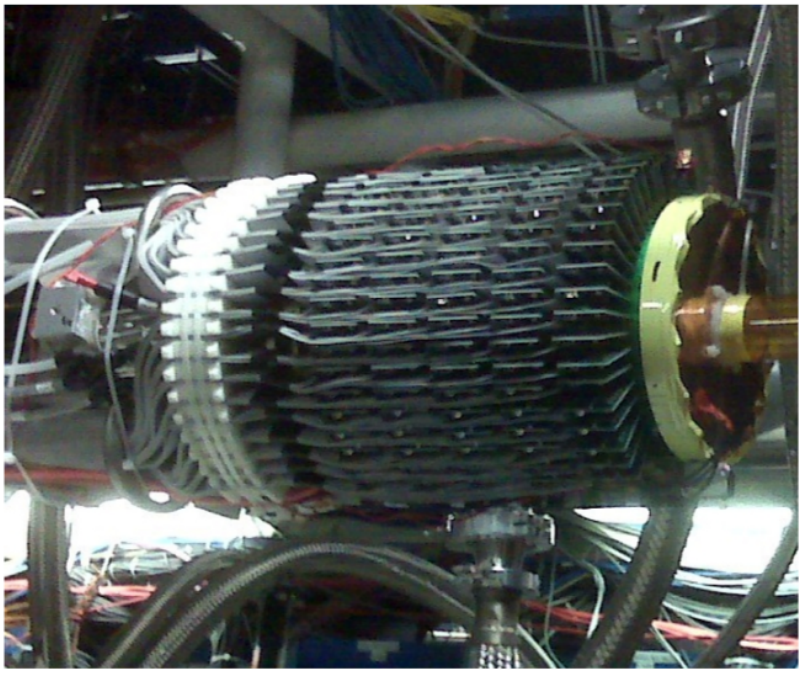

Fig. 4.15: The physical RTPC where the beam would be coming from the left [4].

Coupled with the solenoid, the RTPC measures the recoiling ^{4}He that would never make its way to CLAS. Coherent DVMP processes, where the target helium stays intact, has the recoiling helium with an average p/q of about 100 MeV/c [61]. The existing CLAS system, however, has a p/q threshold of 250 MeV/c [4].

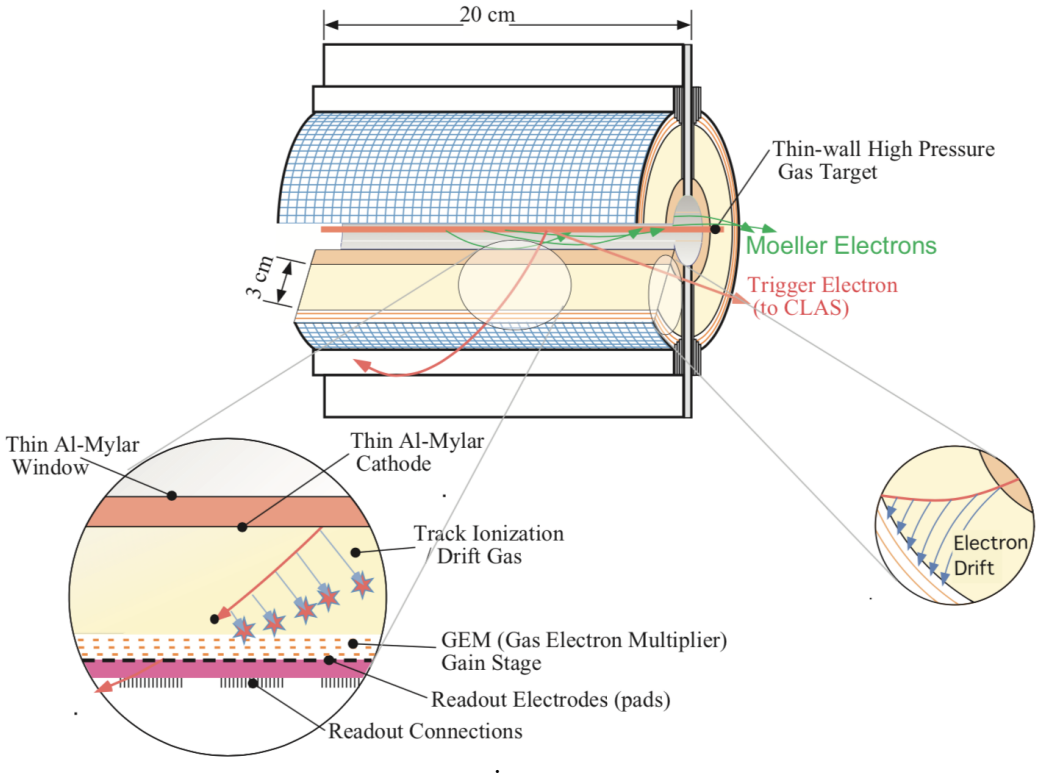

Fig. 4.16: The RTPC schematic [5]

The cylindrical RTPC, shown in **Fig. 4.16**, surrounds the 6 atm ^{4}He gas target with three gaps, in increasing radial distance:

1. A 1 atm ^{4}He gas region to reduce secondary interaction of the recoiled helium with Møller electrons

2. A region filled with the drift gas mixture

3. The drift region which is also filled with the drift gas but starts with a cathode foil that accelerates the drift electrons to the anode, the three subsequent gas electron multiplier (GEM) layers, pictured in **Fig. 4.18**, and to the 3200 readout pads. The GEM layers amplify the signal of the few drift electrons with a 400 V

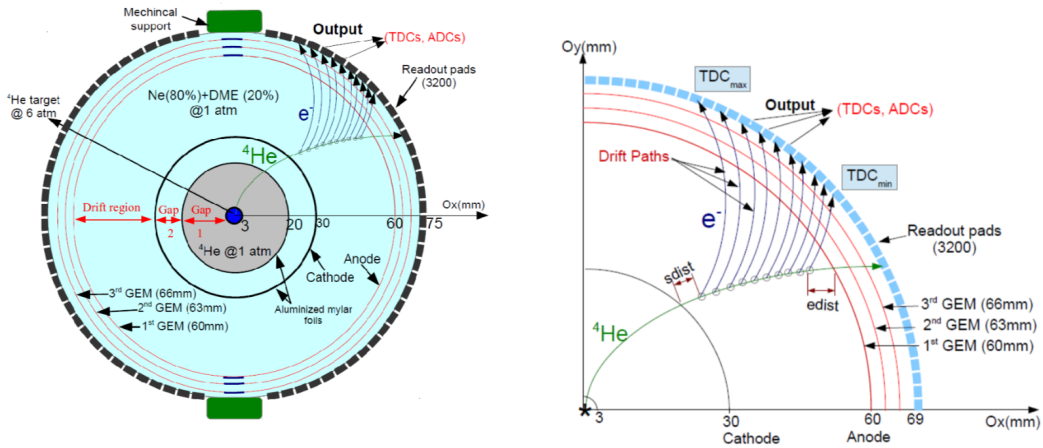

(a) Schematic of ^{4}He track, in green, with ionized electrons, in dark blue, in RTPC

(b) Zoomed quadrant of RTPC with GEM layers and readout pads shown

Fig. 4.17: RTPC track [6]

potential difference at each layer and a 150 V potential difference between each subsequent layer, giving an overall gain on the order of 10^6.

The drift region of the RTPC is comprised of a mixture of 80% neon, and 20% dimethyl ether (C_2H_6O). This gas mixture is chosen for its characteristics of low diffusivity and small Lorentz angles, the angle between the applied magnetic field's and electric field's forces on the drift electron. Effectively, these characteristics minimize the changes in drift speed of the ionized electrons used to determine the track of the helium in the RTPC.

As the helium traverses the RTPC drift region, it ionizes the drift gas and the ionized electrons are curled by the solenoid's magnetic field and accelerated toward the anode, by its potential difference with the cathode, as seen in the schematic **Fig. 4.17b**. The drift electrons cascade through each successive layer of the GEM and creates an

avalanche of secondary electrons that produce a sizable signal. Coupled with the hit position and the timing information from the TDCs, the point of ionization can be determined. A track fitting algorithm can then be used to string these points together to determine the track of the recoiled ^{4}He. With a good understanding of the energy loss along the path, the final state momentum of the ionizing particle can be determined by its track's radius of curvature using a modified version of **Eq. 4.1**.

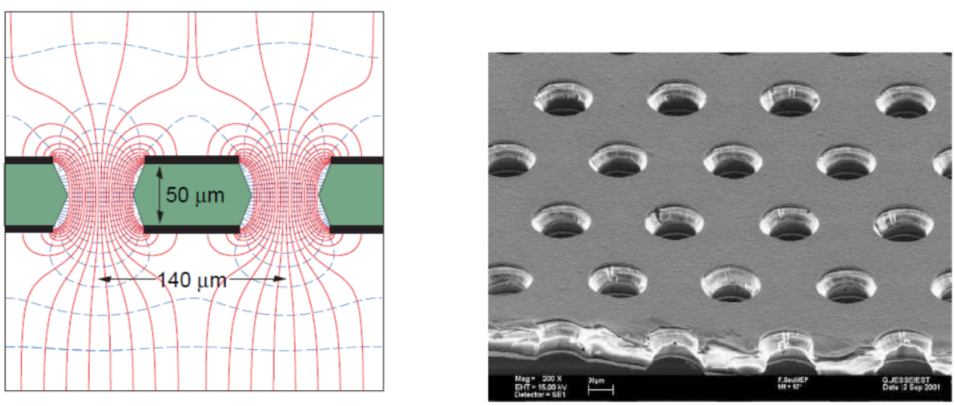

(a) Schematic of a GEM layer used at the anode of the RTPC

(b) Scanning Electron Microscope of a GEM layer

Fig. 4.18: GEM layers [6]

With the CLAS upgrades of the solenoid magnet, the IC, and the RTPC, the full exclusivity required in studying DVπ^0P, among other processes, can be realized.

Chapter 5

Particle Identification (PID)

$$e\ {}^4\mathrm{He} \rightarrow e'\ {}^4\mathrm{He}'\ \pi^0 \rightarrow e'\ {}^4\mathrm{He}'\ \gamma\ \gamma$$

To study coherent DVMP with a ^{4}He target, the particles that need to be identified are the scattered electron with CLAS, the recoiled helium with the RTPC , and the photons decayed from the produced π^0 with the IC and EC. This analysis' particle identification follows exactly the procedure outlined in [5] to evaluate the quality of the kinematic fitting event selection method.

The starting-point files, broken up into `2 GB` chunks, are accessible on the JLab scientific computing cluster, `ifarm` and can be found on the mass storage system, tape library:

`/mss/clas/eg6/production/pass2/6gev/HROOT/`

The files have the form:

$$\texttt{hroot\_}N_{\mathrm{run}}\texttt{\_}N_{\mathrm{file}}\texttt{\_pass2.root}$$

where $N_{\text{run}} \in \{\texttt{61510}, \ldots, \texttt{61930}\}$ is the run number and N_{file} is the two to three digit file number, starting from `00`.

The following histograms will be from just the `61510` run since they capture the signficance of each cut.

For clarity, some efforts are made to highlight the important aspects of each cut:

- In the following 1D histograms,
  - The light-blue filled histograms are the distributions that pass every other particle identifcation cut except its own.
  - The unfilled distributions have no cuts applied.
  - Dotted lines (.....) and dashed lines (----) are used to indicate the lower and upper limit of the cut, respectively. That is, all values greater than the low end and all values to lower than the high end are accepted.
- For 2D histograms, distributions that are of interest are colored and rejected distributions are in grayscale.
- Finally, psuedocode is provided to help clarify what was explicitly done.

5.1 Electron Identification (eID)

$$e\,^4\mathrm{He} \rightarrow e'\,^4\mathrm{He}'\gamma\gamma$$

Identification of the scattered electron is done by a series of cuts. Particles passing all of these cuts are accepted as electrons and will be subject to event selection after. No other particle identifcation is done if the particle fails any of the tests or cuts. For the following procedure, the iteration variable `ipart` will loop over the `EVNT` bank from 0 to `gpart`.

5.1.1 Pre-Cuts

Particles failing any one of these pre-cuts are skipped over entirely. These are the minimal requirements to identify the electron.

5.1.1.1 Status Cut

The status, stored in the array `stat` of the `EVNT` bank, tells whether the particle passed both hit-based tracking (HBT) and time-based tracking (TBT) for DC track reconstruction. In particular, if

```
stat[ipart] > 0 ,
```
(5.1)

the particle passes both HBT and TBT tracking. The distributions can be seen in **Fig. 5.1a**.

5.1.1.2 Charge Cut

The status cut tells us that the DC track reconstruction is good so we can tell whether the partcle traversing the DC is negatively charge, positively charge, or neutral by how it bends under the influence of the torus' magnetic field. Since we are looking for electrons, we want

$$\texttt{q[ipart] < 0} \ , \tag{5.2}$$

where the `q` array holds whether the particle is positively(`+1`)/negatively(`-1`) charged or neutral(`0`), as seen in **Fig. 5.1b**.

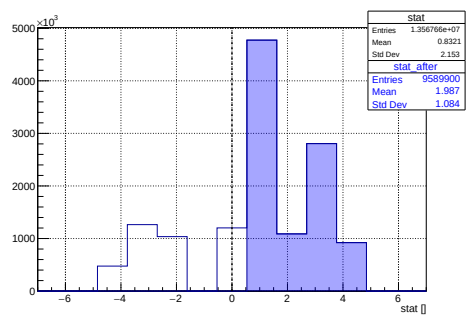

(a) Status Cut: Negative status are rejected.

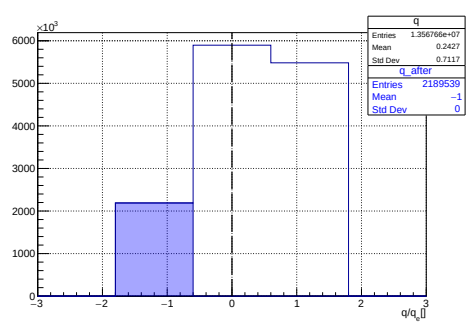

(b) Charge Cut: Only negative tracks pass this cut.

Fig. 5.1: Status and Charge distributions.

5.1.1.3 Sector Matching

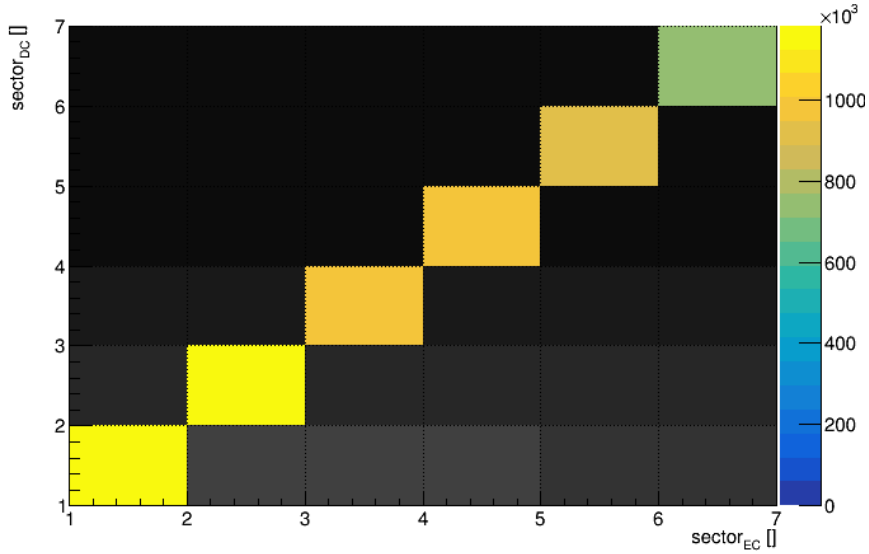

Fig. 5.2: DC sector vs. EC sector: Only matching sectors will pass this cut.

To minimize accidentals and sector edge effects, the sectors of the different detectors are matched:

```
dc_sect[dc[ipart]-1] == ec_sect[ec[ipart]-1]
sc_sect[sc[ipart]-1] == cc_sect[cc[ipart]-1] ,
dc_sect[dc[ipart]-1] == sc_sect[sc[ipart]-1]
```
(5.3)

where `dc_sect`, `ec_sect`, `sc_sect`, and `cc_sect` are fortran arrays in the `DCPB`, `ECPB`, `SCPB`, and `CCPB` banks, respectively. The `dc`, `ec`, `sc`, and `cc` are arrays in the `EVNT` that link the banks used for the DC, EC, SC, and the Cherenkov counters (CC) subdetectors into the `EVNT` bank. As can be seen in **Fig. 5.2**, only equal sectors, along the diagonal, pass this cut.

5.1.2 Vertex Cut

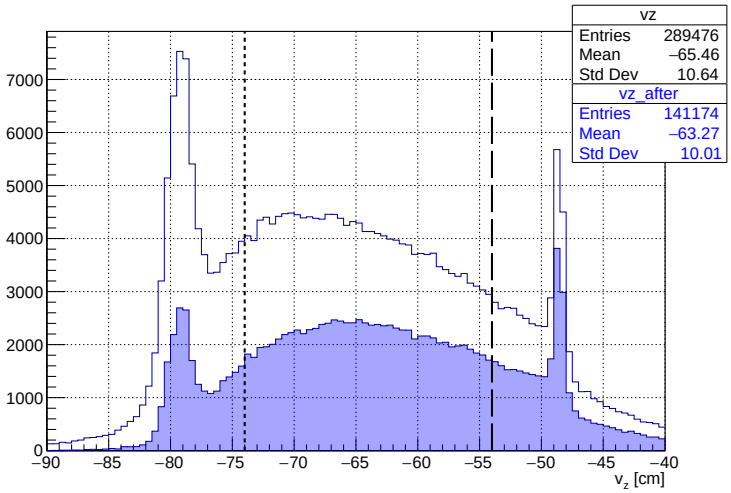

Fig. 5.3: Vertex Cut: Only particles coming from well inside the target walls are accepted.

An electron vertex cut is made to ensure that the detected scattered electron interacted with the target. The center of the target is placed upstream from the nominal center of CLAS at -64 cm. Thus, the walls of the target should be around -80 and -50 cm. Cuts are placed well within the target walls, with the length of the RTPC, to ensure the source of the interaction is well understood.

```
-74 < vz[ipart] && vz[ipart] < -54 ,
```
(5.4)

where `vz` is the array storing the z-component of the vertex in the `EVNT` bank in cm.

5.1.3 Solenoid Fiducial Cut

Although the solenoid is crucial in this experiment for reducing background Møller electrons and for measuring the momenum of the recoiling helium, scattered electrons

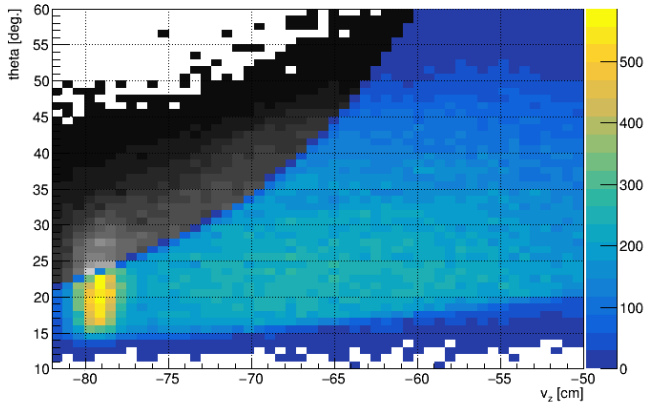

Fig. 5.4: Solenoid Fiducial Cut: Particles that have hit the solenoid are rejected.

with large polar angle will interact with the edge of the solenoid, making momentum reconstruction of these particles lousy.

Therefore, a polar angle cut depending on the electron vertex is introduced to eliminate these particles:

$$\texttt{cz[ipart] > cos(theta\_sol)}, \tag{5.5}$$

where

```
theta_sol = atan2(11, z_sol - vz_corr);
```

```
z_sol = -64 + 20.96/2 ,
```

where `vz_corr` is the z-component of the corrected electron vertex (see **Appendix B.1**), `z_sol` is the center of the solenoid with respect to CLAS, both in cm, and `cz` is the array of the direction cosines along the z-axis of the track.

5.1.4 DC Momentum Cut

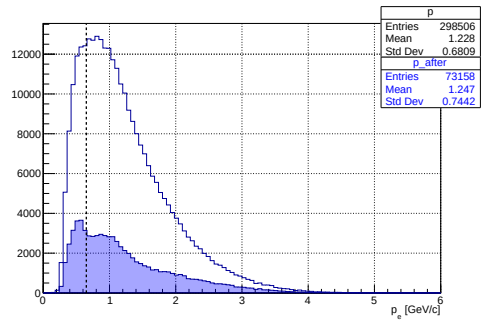

Fig. 5.5: Momentum cut: To protect against Møller electrons and π^- a cut on the momenum is applied.

To minimize radiative effects from low energy electrons and to separate from other negatively charged particles, namely π^-, a cut on the particle's momentum is at least 650 MeV:

```
p[ipart] > 0.65 ,
```
(5.6)

with `p` being the array in the `EVNT` that holds the momentum of the particle in GeV.

5.1.5 DC Fiducial Cut: IC-Shadow

Particles from the target, on their way to CLAS, that hit the IC lose energy so both track and energy reconstruction are compromised. To avoid this altogether, a fiducial cut is placed to rule out these poorly reconstructed particles:

```
!(geo->IsInside(x,y)) ,
```
(5.7)

where `geo` is a shape defined by successive connection of the points in **Table 5.1** and the exclamation mark (`!`) indicates logical negation. `x` and `y` are the x- and y- components

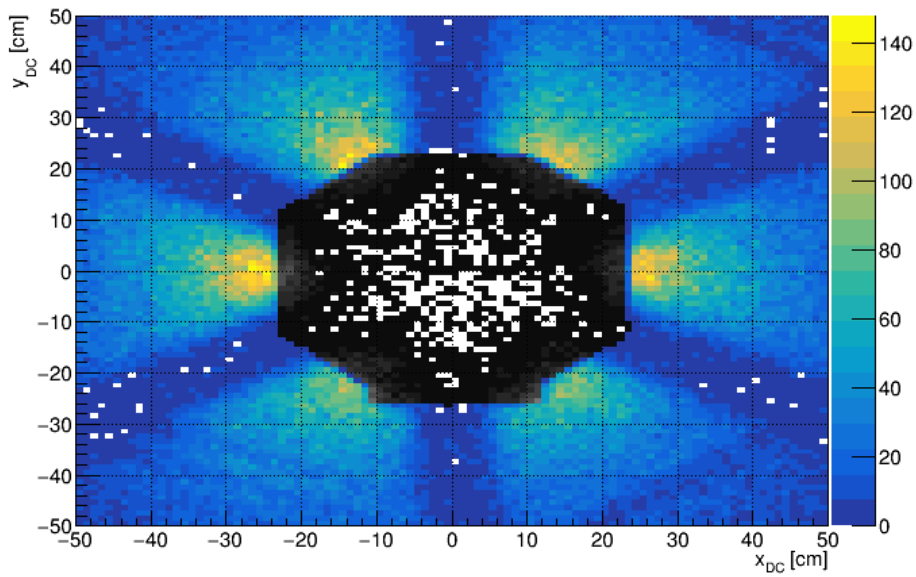

Fig. 5.6: DC Fid. Cut: Tracks directly coming from the IC have energy loss that is unaccounted for.

of $\vec{\boldsymbol{x}}_{\mathrm{IC}}$, which are back-projections of the DC hit to the IC:

$$\vec{\boldsymbol{x}}_{\mathrm{IC}} = \left(\frac{16}{z_{\mathrm{DC}}}\right)\vec{\boldsymbol{x}}_{\mathrm{DC}}$$

with

$$\vec{\boldsymbol{x}}_{\mathrm{DC}} = \begin{bmatrix} \texttt{tl1\_x[dc[ipart]-1]} \\ \texttt{tl1\_y[dc[ipart]-1]} \\ \texttt{tl1\_z[dc[ipart]-1]} \end{bmatrix}$$

being the DC track position, where `tl1_x`, `tl1_y`, and `tl1_z` are arrays in the `DCPB` bank that have the DC's track x-, y-, and z-positions in the first layer, respectively, all in cm.

As seen in **Fig. 5.6**, DC hits that are constructed on the interior of this geometry are rejected (grayscale), and hits on the exterior are accepted (colored).

Index i	x_i **[cm]**	y_i **[cm]**
1	-11.15	-26.07
2	-11.15	-23.10
3	-23.10	-12.85
4	-23.10	11.50
5	-10.30	22.95
6	9.91	22.95
7	23.73	13.10
8	23.73	-12.40
9	12.30	-22.36
10	12.30	-26.07
11	-11.15	-26.07

Table 5.1: Boundary of IC Shadow Fiducial Cut

5.1.6 EC Energy Cut

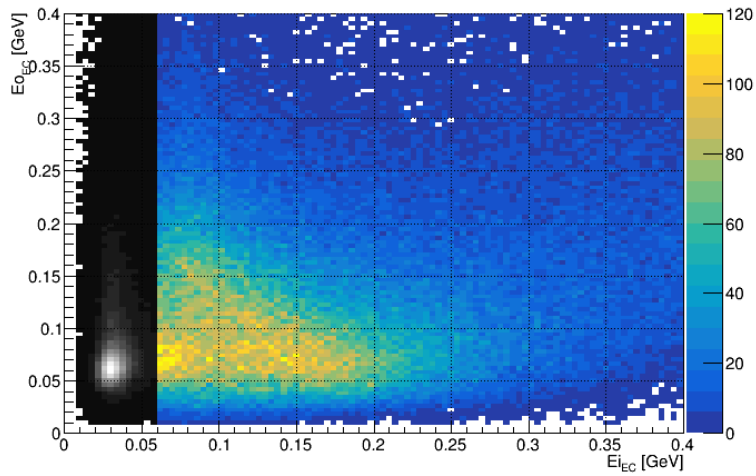

Fig. 5.7: EC Energy Cut: The minimum ionizing π^- imprint can be seen in grayscale are rejected.

Even with the DC momentum cut, there are still π^- that can contaminate the electron sample. This is dealt with by using an EC energy cut. Pions are minimum ionizing particles that lose its energy mostly through ionzination [62]. The EC layers is divided into two parts: an inner part made of thick 5 super-layers and a remaining outer part with 8 super-layers of the 3 cm lead-scintillating material. The pion's energy loss is propotional to the length of EC super-layers it traverses through at 2 MeV/cm, totalling to 60 Mev by the time it passes through the inner part of the EC.

A cut is made at 60 MeV to reject π^-:

$$\texttt{ec\_in[ec[ipart]-1] > 0.06} \ , \tag{5.8}$$

where `ec_in` is the array storing the energy deposited in the inner part of the EC, in GeV, in the `ECPB` bank. The effect can be seen in **Fig. 5.7**, where the π^- distribution can be seen in white with $\texttt{EI}_{EC} < 0.06$ GeV.

5.1.7 EC Sampling Fraction Cut

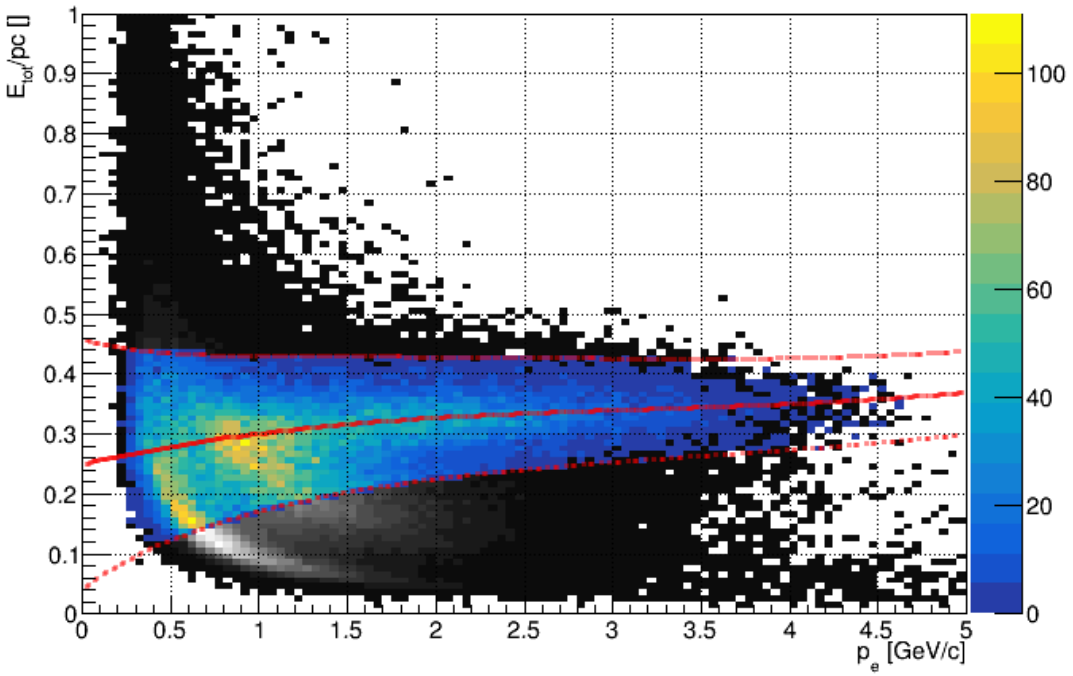

Fig. 5.8: EC Sampling Fraction Cut: The distributions of the energy and sector dependent EC sampling fraction as a function of momentum are shown (for sector 1). The dependence is fitted and measurements 3.5 σ outside the fit are rejected (shown in red).

The electron's sampling fraction, `SF`, is ratio of the measured energy in the EC to the momentum in the DC. If all of the energy is measured in the EC, this ratio should be more or less unity. However, because the EC is a sampling calorimeter with, energy deposited in the lead layers cannot be measured. The EC was designed and optimized through simulation to have this sampling fraction ratio at about 0.3 but due to energy loss, radiative effects, and produced shower geometry, especially at low momentum, the quality of energy reconstruction is hindered. To address this, a cut on the sampling

fraction is made:

```
abs( SF - mu ) < 3.5 * sigma ,
```
(5.9)

where `mu` and `sigma` are calculated from the electron's momentum:

$$\texttt{mu}\,(p) = a + bp + cp^2 + dp^3$$

$$\texttt{sigma}\,(p) = \frac{e}{\sqrt{f+p}}$$

with the parameters, a, b, c, d, e, and f are sector dependent, tabulated in **Table 5.2**.

	Paramter					
Sector	a	b	c	d	e	f
1	0.2490	0.0676	-0.0182	0.00190	0.0469	0.6123
2	0.2636	0.0557	-0.0132	0.00120	0.0508	1.3342
3	0.2721	0.0563	-0.0127	0.00125	0.0518	1.5067
4	0.2727	0.0507	-0.0117	0.00110	0.0427	0.6838
5	0.2593	0.0476	-0.0100	0.00090	0.0469	0.4713
6	0.2517	0.0562	-0.0137	0.00130	0.0440	0.4299

Table 5.2: Sampling Fraction Parameters (transpose can be found in [5])

The measured sampling fraction, `SF`, is the energy from the EC, taken to be the maximum between the total energy measured and the sum of the energy deposited in the inner and outer parts of the EC, in the `ECPB` bank over the momenum from the `EVNT` bank:

```
SF = max( Ei + Eo, Etot )/p[ipart];

          Ei = ec_ei[ec[ipart]-1]

          Eo = ec_eo[ec[ipart]-1]

        Etot =  etot[ec[ipart]-1]
```

`SF` outside the 3.5 `sigma` cut are thrown out and the resulting cut can be seen in **Fig. 5.8**.

5.1.8 EC Fiducial Cut

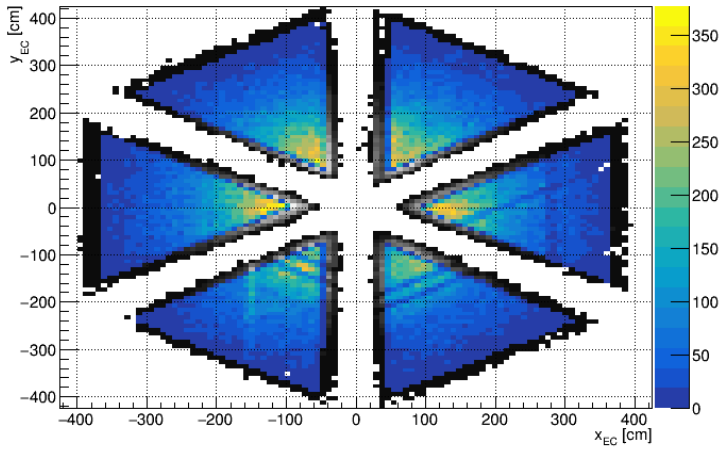

Fig. 5.9: EC Fid Cut: x- and y-coordinates of the face of the EC that are rejected (grayscale) and accepted (colored).

To reject partial energy reconstruction from particles hitting the edge of the EC, a fiducial cut is introduced.

The triangular coordinate system in the EC, where the u-, v-, and w-axes are parallel to the scintillating strips of a layer is utilized to conveniently define the edges of each EC sector. The cuts that are placed are then:

```
60 < u && u < 390
v < 360 ,
w < 390
```

(5.10)

The EC coordinates u, v, and w are shown explicitly in **Appendix C.1** in terms of the EC's Cartesian coordinates x, y and z.

If no electrons are identified for a given event, the event is skipped over since the identification of other particles rely on a good determination of the scattered electron. The electron takes the momentum:

$$P_e = (\vec{\boldsymbol{p}}_e, p_e)$$

where $p_e =$ `p[ipart]` and

$$\vec{\boldsymbol{p}}_e = p_e * \begin{bmatrix} \texttt{cx[ipart]} \\ \texttt{cy[ipart]} \\ \texttt{cz[ipart]} \end{bmatrix}$$

with `cx`, `cy`, and `cz` being arrays in the `EVNT` bank that house the x-, y-, and z- components of the unit direction vector.

5.2 Photon Identification (γID)

$$e\,^4\mathrm{He} \rightarrow e'\,^4\mathrm{He}'\gamma\gamma$$

Both calorimeters, the EC and IC are capable of detecting photons. The difference in geometry alone require different cuts for photon identification. Ultimately, the difference in detector makeup require entirely independent methods for qualifying whether a photon is "good" or not.

5.2.1 EC Photon Identification ($\gamma_{\mathbf{EC}}$ID)

The photons that make their way to the EC have larger polar angle and typically lower energies. To determine whether or not a photon has made it to the EC, the following cuts are applied. Note, since EC photons do not make it their way into the previous analysis [5], a slightly modified version of Hattawy's particle identification [4], which now includes other EC corrections (see **Appendix B.3**), is applied. Again, the index variable, `ipart`, loops over the `EVNT` bank from 0 to `gpart` and the `ec` array translate the indices of `EVNT` bank to the `ECPB` bank that holds the EC's information.

5.2.1.1 Charge Cut

We only want neutral particles, so a cut is made on the charge:

```
q[ipart] == 0 ,
```
(5.11)

`q` again is the array in the `EVNT` bank that holds the charge of the particle.

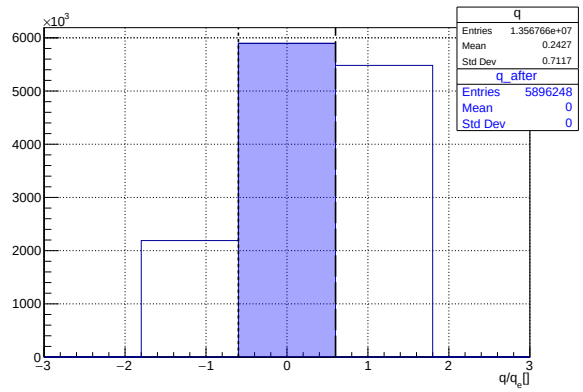

Fig. 5.10: Charge Cut: Neutral particles are accepted.

5.2.1.2 β Cut

To reject other neutral particles, like the neutron, a cut to the normalized velocity, $\beta = v/c$, is applied to all neutral particles.

```
abs( b[ipart] - 1 ) < 0.07 ,
```
(5.12)

`b` is the array in the `EVNT` bank that holds the measured β values. The resulting cut is shown in **Fig. 5.11a**.

5.2.1.3 Energy Cut

Photon reconstruction becomes increasingly difficult at low energies, especially with a sampling calorimeter; the low energy photon can only make it through a few layers of the lead and scintillating material and the showers produced may be fully absorbed in the insensitive layer of lead, never making it to the next scintillating layer.

```
E > 0.3 ,
```
(5.13)

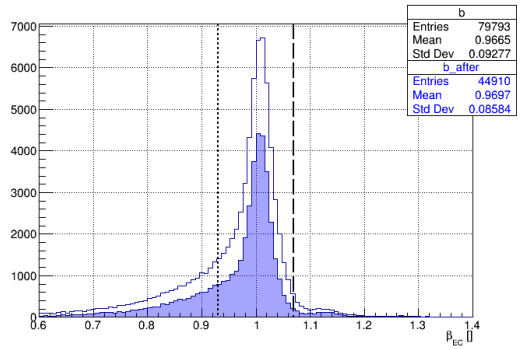

(a) β Cut: To reject neutrons, a β cut is applied to accept the much faster photons.

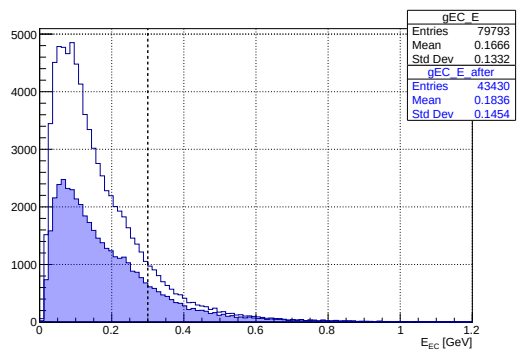

(b) Energy Cut: Lower energy particles are poorly reconstructed. These particles are rejected.

where `E` is the photon's total energy taken to be

```
E = max( Etot, Ei + Eo )/ 0.273 ,
```

with `Etot`, `Ei`, and `Eo` are defined previously in **Section 5.1.7** and 0.273 is the nominal sampling fraction, the optimized and designed value of the ratio of the energy deposited to the total energy in the EC. The accepted and rejected distributions are shown in **Fig. 5.11b**.

5.2.1.4 EC Fiducial Cut

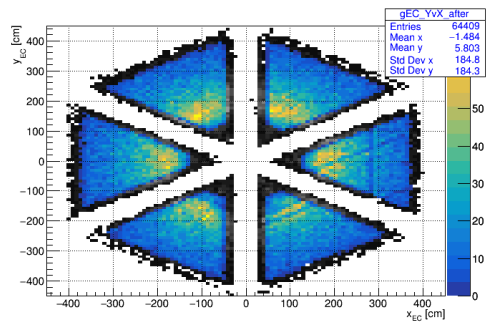

Fig. 5.12: EC Fid. Cut: Reject particles hitting the edges of the EC.

To reject partial energy reconstruction from particles hitting the edge of the EC, the fiducial cut is used:

$$\begin{aligned} \texttt{100 < u \&\& u < 390} \\ \texttt{v < 360} \\ \texttt{w < 390} \end{aligned} \tag{5.14}$$

where `u`, `v`, and `w` are constructed in the same way as it is in **Section 5.1.8**.

\- -

Accepted EC photons take momentum

$$P_\gamma = (\vec{\boldsymbol{p}}_\gamma, E_\gamma)$$

where

$$\vec{\boldsymbol{p}}_\gamma = E_\gamma \begin{bmatrix} \texttt{cx[ipart]} \\ \texttt{cy[ipart]} \\ \texttt{cz[ipart]} \end{bmatrix}$$

with

$E_\gamma =$ `E * scaleFac( E );`

`E = max( Etot, Ei + Eo )/ sampFrac(runnb, evntid, sector)`

`sampFrac`, which depends on the run number (`runnb`), event number (`evntid`), and sector, is the time and sector dependent EC sampling fraction correction done by N. Baltzell [63], as discussed in **Section B.3.1**. `scaleFac`, which depends on the measured energy, `E`, is energy dependent EC scaling factor correction done in this study, as discussed in **Appendix B.3.2**.

5.2.2 IC Photon Identification ($\gamma_{\mathbf{IC}}$ID)

The geometry and position of the IC dictate the kinematics of what photons can be identified; they are lower angle (between 8° and 15°), high energy photons. Again, the procedure to pick out good photons follows the previously done work [5]. The following procedure will have index `iic` to loop over the `ICPB` bank ranging from 0 to `icpart`.

5.2.2.1 Energy Cut

Similar to the EC, lower energy photons are difficult to reconstruct. In the IC, the shower produced by lower energy photons are shallower but broader, making both energy and position reconstruction poor. An energy cut is applied:

$$\texttt{etc[iic] > 0.2} \ , \tag{5.15}$$

with `etc` being the array in the `ICPB` bank that has the energy in GeV. The distributions and cut can be seen in **Fig. 5.13a**.

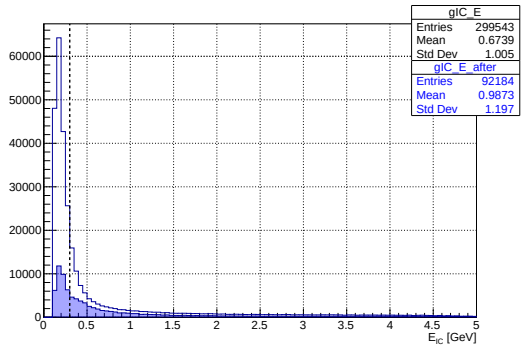

(a) Energy Cut: Lower energy particles are poorly reconstructed due to energy loss and radiative effects. These particles are rejected.

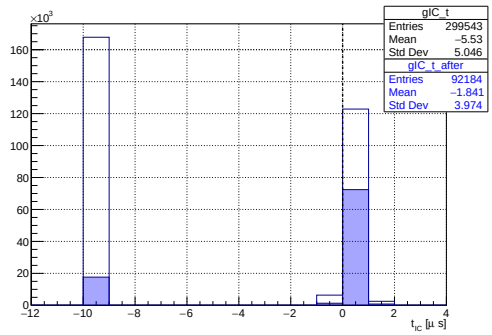

(b) Timing Cut: Particles with no IC cluster timing information are just background when forming photon pairs [5].

5.2.2.2 Timing Cut

Events that do not have cluster timing information are automatically placed at some fixed negative value. To exclude these poorly reconstructed particles, a cut on the cluster time is applied:

$$\texttt{tc[iic] > 0} \ , \tag{5.16}$$

with `tc` being the array in the `ICPB` bank that has cluster timing information in ns. The disitribution, in μs, and cuts can be seen in **Fig. 5.13b**.

5.2.2.3 Møller Electron Cut

The number of pesky Møller electrons are minimized by the field produced by the solenoid but some still make it to the IC since the IC is designed to have acceptance of

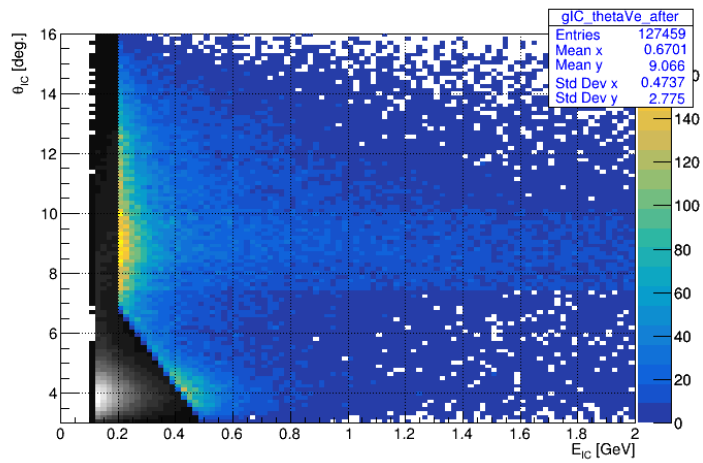

Fig. 5.14: Møller Electron Cut: A geometric cut is applied to reject low-energy, low-angle Møller electrons

low-polar angle photons. A geometrical cut is introduced to deal with these:

$$\texttt{!isInMollerRegion(etc[iic], theta)}, \tag{5.17}$$

where `theta`, in degrees, is obtained from the position vector $\vec{\boldsymbol{r}}_{\mathrm{IC}}$:

$$\vec{\boldsymbol{r}}_{\mathrm{IC}} = \begin{bmatrix} \texttt{xc[iic]} \\ \texttt{yc[iic]} \\ \texttt{zc[iic] - vz\_e} \end{bmatrix}$$

with `vz_e` being the z-component of the trigger electron's vertex and `xc`, `yc`, and `zc` being IC hit positions in cm.

Explicitly, `isInMollerRegion` can be expressed as

```
isInMollerRegion( theta, E ){
  if( E < m * theta + b ) return true
  return false
}
```

with `m` the slope and `b` is the intercept of the cut having values:

```
m = -0.3/4
b =  2.9/4
```

5.2.2.4 Hot Channels Cut

Over the course of the experiment, some crystals were overheated and were registering many more hits than all other crystals. To deal with this, we reject these hot crystals:

```
!isInICHotChannel(ix, iy)
```
(5.18)

where

```
ix = (int) round(x_ichb/dx)

iy = (int) round(y_ichb/dy)
```

are the pixel indices for `x_ichb` and `y_ichb`, the x- and y- positions, in cm, of the `ICHB` bank given by

```
x_ichb = ich_xgl[ihit]

y_ichb = ich_ygl[ihit]
```

with `ihit` being the hit ID in the `ICHB` bank given by

```
ihit = (statc[iic] - statc[iic]%10000) / 10000 - 1 .
```

The hard-coded values `dx` and `dy` are the width and height of each crystal with values tabulated in **Table 5.3**.

Variable	Value	Units
dx	1.346	cm
dy	1.360	cm

Table 5.3: Hard-Coded IC Values

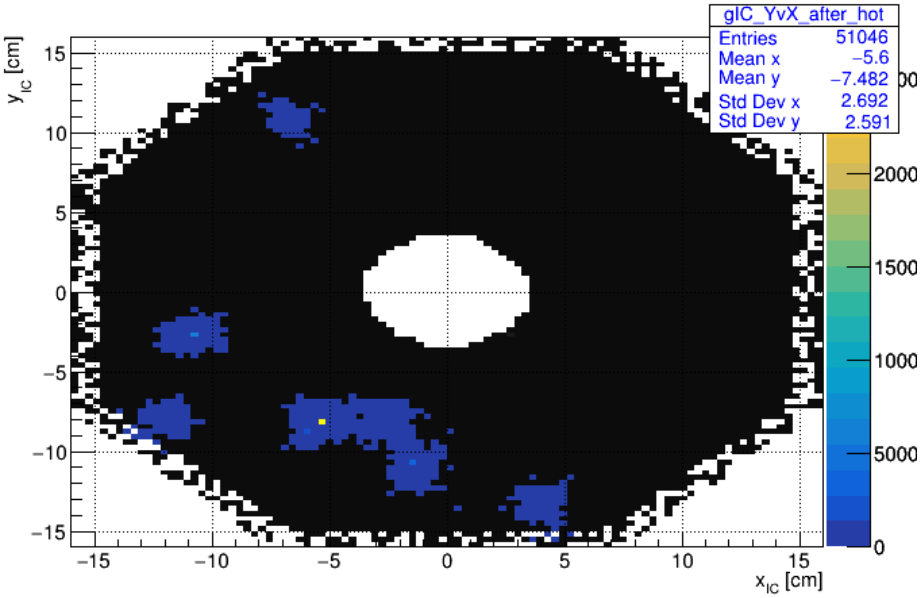

(a) Rejected hot channels.

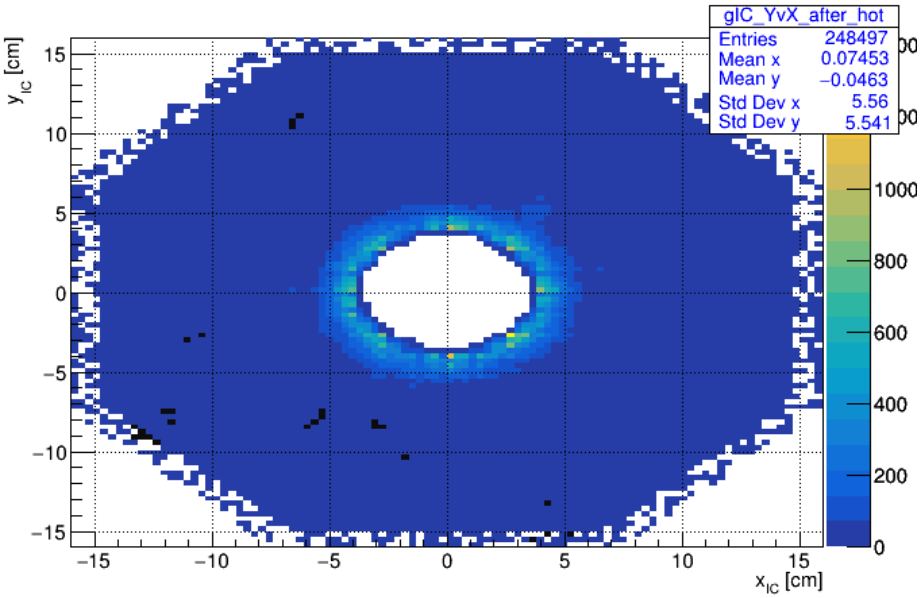

(b) Accepted channels.

Fig. 5.15: Hot Channels Cut: The position of the hits in the IC that are rejected (5.15a) and accepted (5.15b) by the cut.

5.2.2.5 IC Fiducial Cut

To ignore poor reconstruction of photons hitting the edges of the IC, are ignored. The fiducial cut follows the procedure outlined by F.X. Girod [45]:

$$\texttt{isInICFiducial(x,y)} \tag{5.19}$$

here `isInICFiducial` is a method that depends on the IC hit positions, `x` and `y` and can be broken down into two parts:

```
isInICFiducial(x,y){
  if( isOutICOuterEdge(x,y) ) return false
  if( isInICnnerEdge(x,y)   ) return false
  return true
}
```

The x- and y- positions of the hits, `x` and `y` are given by:

```
x = xc[iic]
y = yc[iic]
```

where `xc` and `yc` are arrays from the `ICPB` bank that hold the x- and y- positions of the hit in cm.

`isOutICOuterEdge` returns whether or not the point (`x,y`) is outside the outer edge of the IC and `isInICInnerEdge` returns whether or not the point is inside the inner edge of the IC. Their explicit psuedocode is given in **Appendix C.3**.

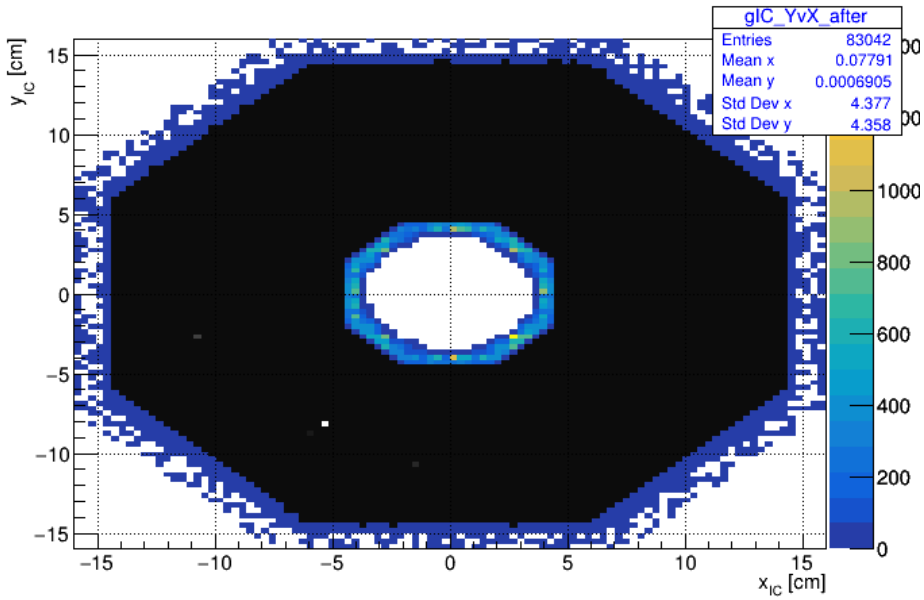

(a) Rejected IC hits.

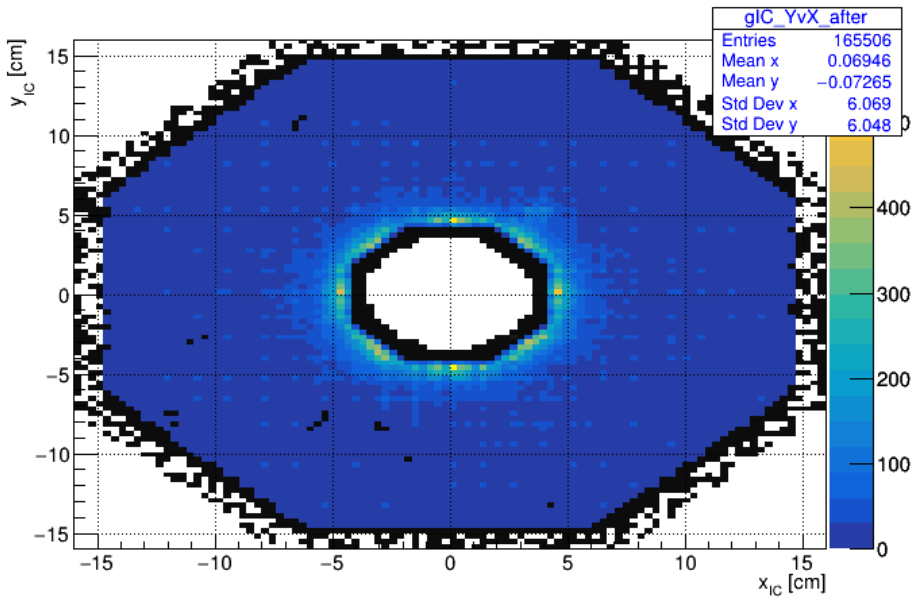

(b) Accepted IC hits that pass both the Hot Channels and IC Fiducial Cuts.

Fig. 5.16: IC Fiducial Cut: The position of the hits in the IC that are rejected (5.16a) by the cut and accepted (5.16b) by both the Hot Channels and Fiducial Cuts (to see features).

The accepted IC photons take momentum

$$P_\gamma = (\vec{\boldsymbol{p}}_\gamma, E_\gamma)$$

where

$$\vec{\boldsymbol{p}}_\gamma = E_\gamma \hat{\boldsymbol{r}}_{\mathrm{IC}}$$

$\hat{\boldsymbol{r}}_{\mathrm{IC}}$ being the direction vector coming from the IC hit position vector w.r.t target, $\vec{\boldsymbol{r}}_{\mathrm{IC}}$, defined in **Section 5.2.2.3** and the energy is:

$$E_\gamma = \texttt{etc[iic]}$$

5.3 Helium Identification (^{4}He**ID**)

$$e^4\mathrm{He} \rightarrow e'^4\mathrm{He}'\gamma\gamma$$

The recoiled ^{4}He identification is done by its own series of tests/cuts. Particles passing all of these tests are taken to be good tracks and will be subjected to event selection after.

For the following procedure, the iteration variables `igcpb` will loop over the `GCPB` bank from 0 to `gcpart` and `irtpc` will loop over the `RTPC` bank from 0 to `rtpc_npart`.

5.3.1 Pre-Cuts

Particles failing any one of these pre-cuts are skipped over entirely. These are the minimal requirements to identifying the helium.

5.3.1.1 Number of Pads Cut

Poor track reconstruction in the RTPC is due to too few pads firing. We therefore cut on:

$$\texttt{npd\_track[igcpb] > 3} \ , \tag{5.20}$$

where `npd_track` is the `GCPB` bank array that is filled with the number of pads fired for a given track.

5.3.1.2 Charge Cut

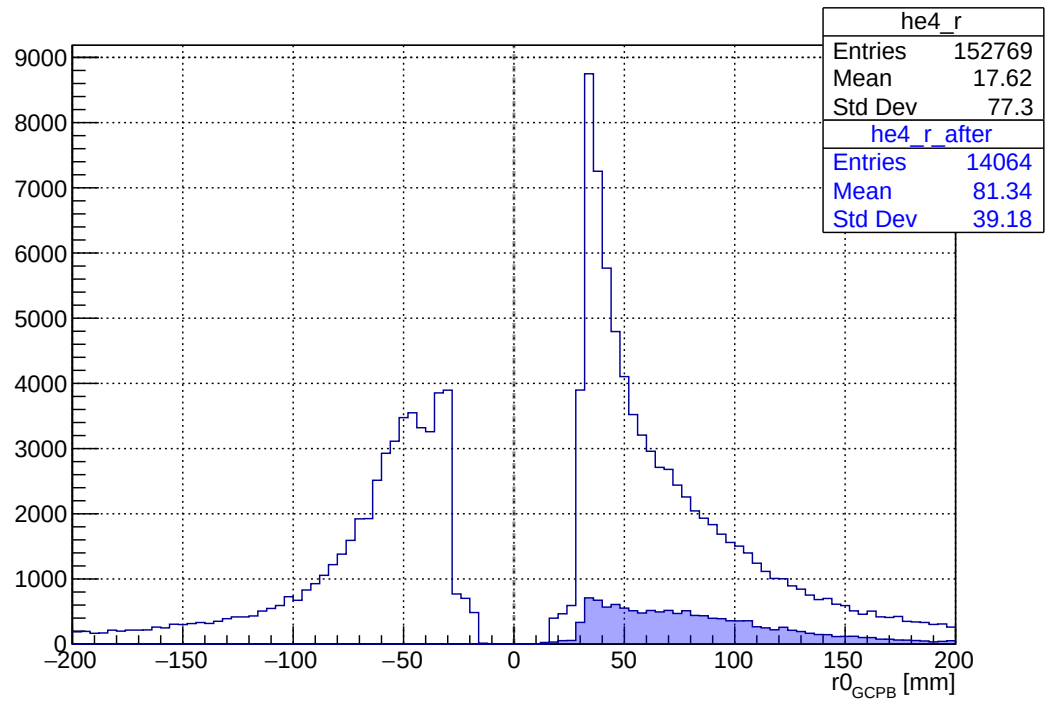

Fig. 5.17: Charge Cut: Negatively charged tracks (negative radius of curvature) are thrown out.

To remove tracks of negatively charged particles, we throw away all tracks except for the ones with positive radius of curvature:

$$\texttt{r\_0[igcpb] > 0} \ , \tag{5.21}$$

where `r_0` is the `GCPB` bank array that is filled with the radius of curvature in mm, where the sign of the curvature corresponds to the sign of the particle.

5.3.2 χ^2 Cut

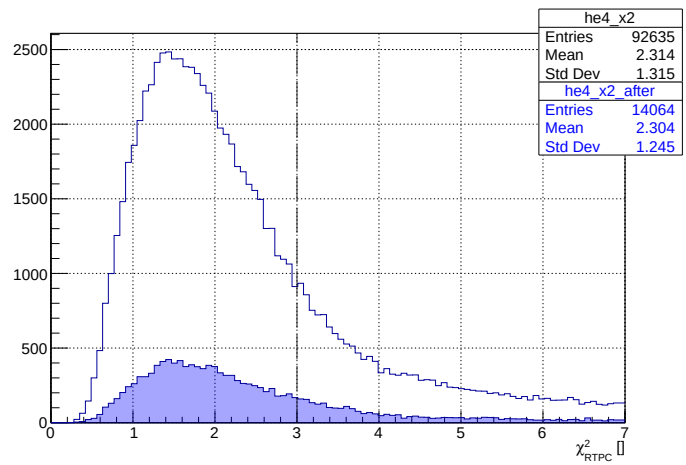

Fig. 5.18: χ^2 Cut: The χ^2-distribution obtained from fitting the RTPC tracks correspond to how well the ionization points are fit. High χ^2, corresponding to poor fits, are rejected.

The quality of the track fit is encompassed by the χ^2-distribution. A low χ^2 signifies the fit to the hypothesized modified helix is satisfactory for the given number of degrees of freedom. A preliminary cut to the χ^2 distribution is made to immediately throw away poorly reconstructed tracks:

```
x2[igcpb] < 3 ,
```
(5.22)

where `x2` is the `GCPB` bank array that is filled with the calculated χ^2 for each track.

5.3.3 `edist` Cut

The end-distance, or `edist`, is the distance from the last point of ionization to the anode. Positive values indicate ionization points are reconstructed in the drift region, between the anode and cathode, and negative values are points reconstructed past the

anode (see **Fig. 4.17b**). This cut removes tracks where the last ionization point is too far from the anode. These tracks statistically have fewer ionizations points which lead to fewer constraints (and likely poor reconstruction) in track fitting. Good tracks are within:

```
-5 < edist[igcpb] && edist[igcpb] < 10 ,
```
(5.23)

where `edist` is the `GCPB` bank array that is filled with the end-distance in mm. The distributions and the cuts can be seen in **Fig. 5.19a**.

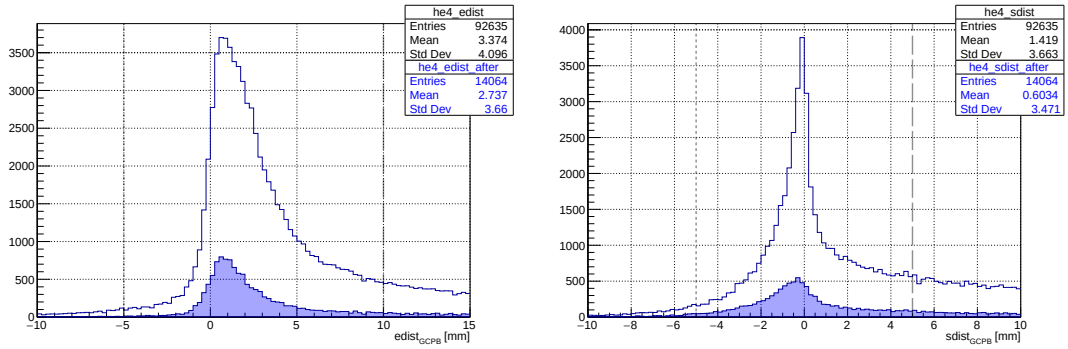

(a) `edist` Cut: Ionization too far from the anode are rejected.

(b) `sdist` Cut: Ionization too far from the cathode are rejected.

Fig. 5.19: Ionization Cuts for all tracks

5.3.4 `sdist` Cut

The start-distance, or `sdist`, is the distance from the first ionization point to the cathode. Again, positive values here indicate ionization points are reconstructed in the drift region, between the anode and cathode, but negative values are points reconstructed before the cathode (see **Fig. 4.17b**). For similar reasons to **Section 5.3.3**, a cut is

placed on the `sdist` distributions:

$$\texttt{-5 < sdist[igcpb] \&\& sdist[igcpb] < 5} \ , \tag{5.24}$$

where `sdist` is the `GCPB` bank array that is filled with the start-distance in mm. The distributions and the cuts can be seen in **Fig. 5.19b**.

5.3.5 $\theta_{\mathbf{RTPC}}$ Cut

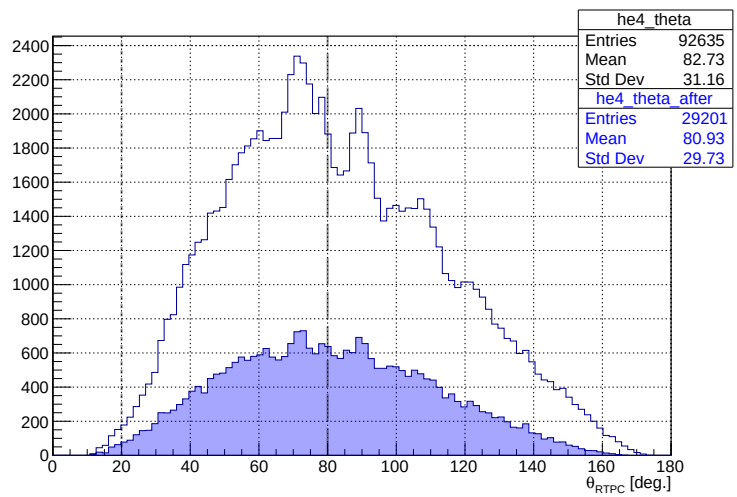

Fig. 5.20: θ Cut: Backward traveling tracks are rejected.

Backward tracks, w.r.t the beam, and low polar-angle tracks are rejected. Polar angles in the range

$$\texttt{20 < theta}_{\texttt{deg}}\texttt{ \&\& theta}_{\texttt{deg}}\texttt{ < 80} \ , \tag{5.25}$$

are accepted, where $\texttt{theta}_{\texttt{deg}}$ is the corrected θ_{RTPC} (see **Appendix B.2.1**) in degrees. θ_{RTPC} is originally extracted from the dip angle in the helical track fitting procedure. The resulting distributions are shown in **Fig. 5.20**.

5.3.6 Vertex Cut

To ensure that the track is coming from inside the target and the RTPC, a vertex cut is applied:

$$\texttt{abs(vz\_mm) < 110 ,} \tag{5.26}$$

where `vz_mm` is the corrected vertex vz_{RTPC} (see **Section B.2.2**) but in mm. The distributions of no cuts, all other cuts are shown in **Fig. 5.21b**, with the cuts shown as lines.

5.3.7 Vertex Coincidence Cut

To reasonably tie the track to coincide with the scattered electron, the vertex coincidence, `Dvz` distribution is cut on:

$$\texttt{abs(Dvz - mu\_Dvz) < 3.5 sigma\_Dvz ,} \tag{5.27}$$

where

```
mu_Dvz    = -0.043
sigma_Dvz =  0.673
```

are previously studied means and widths for the distribution (extracted from residual distributions) and `Dvz` is the distance between the corrected vertex (see **Section B.2.2**) and the electron's vertex, are all in cm. The distributions are shown in **Fig. 5.21b**.

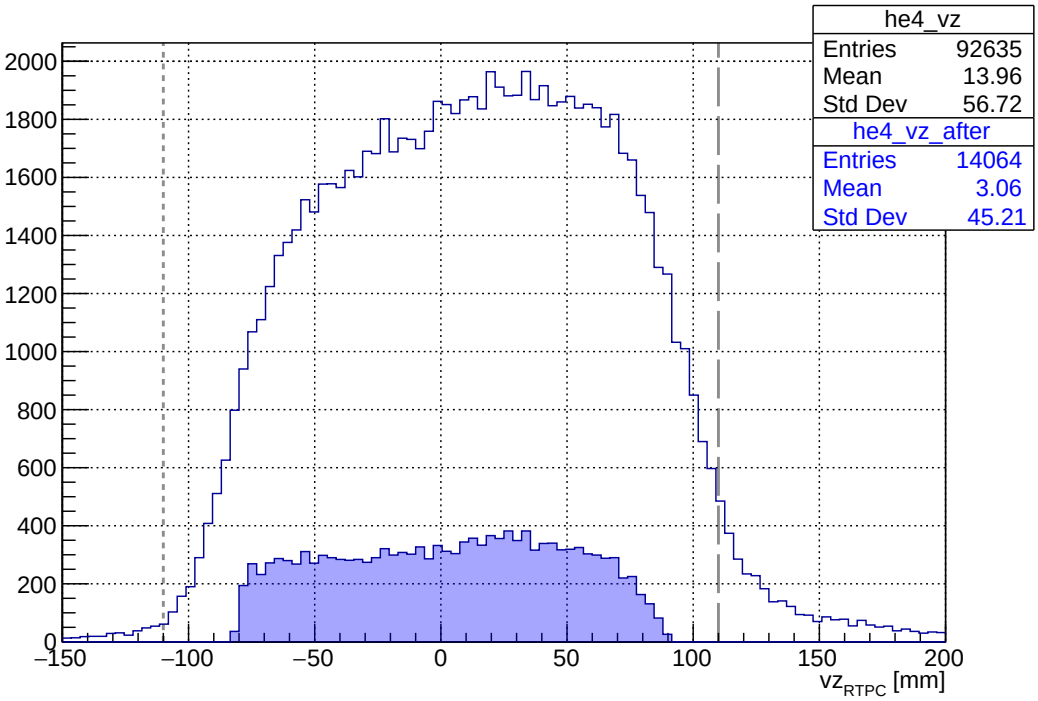

(a) Vertex Cut: Corrected, reconstructed vertices from outside the RTPC are rejected.

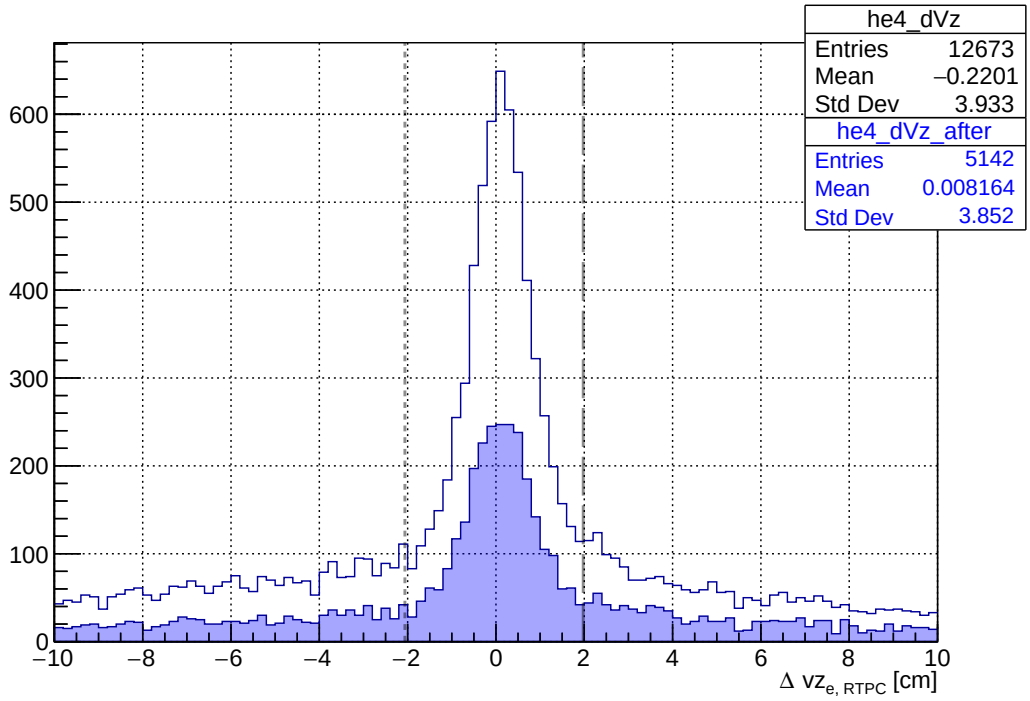

(b) Vertex Coincidence Cut: Vertices that are too far from the trigger electron are rejected.

Fig. 5.21: RTPC Vertex Cuts for all tracks

5.3.8 RTPC Fiducial Cuts

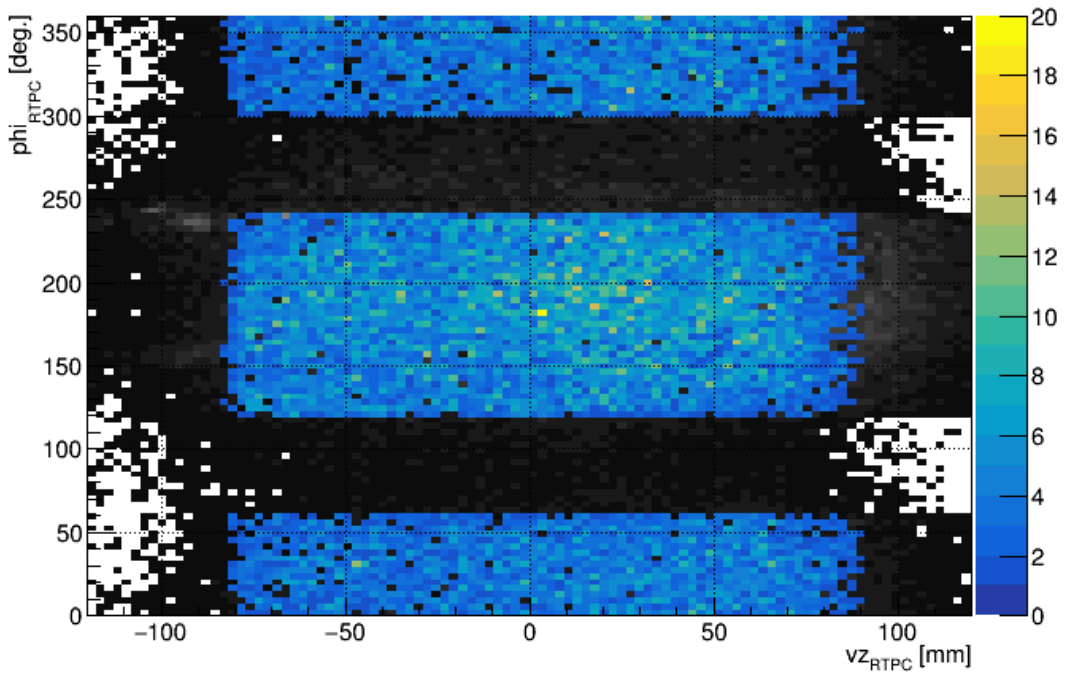

Fig. 5.22: RTPC Fiducial Cuts: Distributions of the RTPC hits that fail the cuts are grayscale and the hits that pass are in color.

For good track reconstruction, the particle should (1) be within the anode and cathode, (2) not hit the top or bottom support regions, and (3) not hit the upstream target holder nose. A fiducial cut is applied to reject these troublesome tracks:

$$\texttt{isInRTPCFiducial(vz, theta, phi)} \tag{5.28}$$

here `isInRTPCFiducial` is a method that depends on the track's corrected vertex, `vz`, corrected polar angle `theta`, and azimuthal angle, `phi`.

It is a test that passes only if all three of subtests pass (all of which are explicitly shown in **Appendix ??**).

```
isInRTPCFiducial(vz, theta, phi){
  if( !isInRTPCDrift(vz, theta)   ) return false
  if(  isInRTPCSupport(phi)       ) return false
  if(  isInRTPCHolder(vz, theta)  ) return false
  return true
}
```

5.3.9 Distinguishing ^{4}He

Up until now, only positive tracks within the fiducial region have been selected. From these selected tracks, the determination of whether the particle traversing the drift region is actually ^{4}He is done by monitoring how much energy is deposited along the track. This energy deposition rate, dE/dx (determined from the charge collected in the GEMs), depends on the momentum per charge, p/q (determined by the track's radius of curvature and applied magnetic field), and is characteristic of the mass. The dependence can be seen in **Fig. 5.23** with the expected Bethe-Bloch curves for the possible positively charged particles superimposed over the histograms.

It is clear that the resolution is not there to distinguish the tracks into different particles. However, an algorithm was used to sort out the closest Bethe-Bloch curves for a given track's measured (p/q, dE/dx) [4]. In summary, the residual distance from

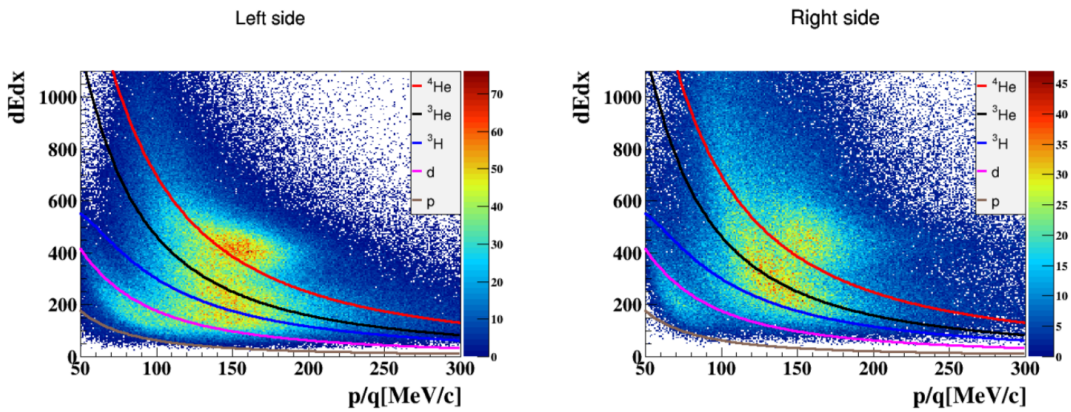

Fig. 5.23: Bethe-Bloch curves overlaying the dE/dx vs. p/q distributions for the left and right sides of the RTPC [4].

`pid_i`	**Particle**
47	^{4}He
49	^{3}He
46	^{3}H
45	d
2212	p

Table 5.4: Index table for `pid_i`

(p/q, dE/dx) to each of the curves is calculated, then each associated particle ID (`pid` in **Table 5.4**) is sorted with the smallest residual `pid` stored in `rtpc_id1` through to the largest residual `pid` stored in `rtpc_id5`. Correspondingly, the momentum is calculated and stored in an array `rtpc_p1`, ..., `rtpc_p5` for each of these assumptions.

For a given track indexed by `irtpc`, the track is considered to be ^{4}He if the

smallest residual corresponds to the ^{4}He Bethe-Bloch curve:

```
rptc_id1[irptc] == 47
```
(5.29)

The ^{4}He track then takes momentum

$$P_{^4\mathrm{He}} = (\vec{\boldsymbol{p}}_{^4\mathrm{He}}, E_{^4\mathrm{He}})$$

where

$$\vec{\boldsymbol{p}}_{^4\mathrm{He}} = p_{^4\mathrm{He}} \hat{\boldsymbol{r}}_{\mathrm{RTPC}}$$

with $\hat{\boldsymbol{r}}_{\mathrm{RTPC}}$ being the directional unit vector, defined by azimuthal `rtpc_phi[irtpc]` and the corrected polar θ_{RTPC} (see **Appendix B.2.1**) angles. The magnitude $p_{^4\mathrm{He}}$ in GeV/c is:

$$p_{^4\mathrm{He}} = \texttt{rtpc\_p1[irptc] / 1000} \quad .$$

`rtpc_phi`, `rtpc_p1`, and `rtpc_id1` are `RTPC` bank arrays with `rtpc_phi` holding the azimuthal angle in rad. and `rtpc_p1` holding the energy-loss corrected momentum at vertex in MeV/c. Finally, the energy is:

$$E_{^4\mathrm{He}} = \sqrt{p_{^4\mathrm{He}}^2 + M_{^4\mathrm{He}}^2} \quad ,$$

where $M_{^4\mathrm{He}}$ is the nominal value for the helium mass of 3.7284 GeV/c^2.

Chapter 6

Event Selection Method I: Exclusivity Cuts

Before going into kinematic fitting, an overview of the standard and previously used technique [5, 6] of exclusivity cuts is shown. First, definitions of the exclusivity variables are introduced. Then, distributions of these variables will be subjected to the cuts that will later be compared to the distributions produced from kinematic fitting.

6.1 Exclusivity Variable Definitions

Index i	**Configuration**
0	$e\ {}^4\mathrm{He} \rightarrow e'\ {}^4\mathrm{He}'\ \pi^0$
1	$e\ {}^4\mathrm{He} \rightarrow e'\ {}^4\mathrm{He}'\ \pi^0$
2	$e\ {}^4\mathrm{He} \rightarrow e'\ {}^4\mathrm{He}'\ \pi^0$

Table 6.1: Configurations: Grayed out particles are not measured.

Let X_i denote the missing particle in the final state configuration, indexed by i, listed in **Table 6.1**; P_{Beam} the initial eletron 4-momentum; and P_{Targ} the initial target ^{4}He 4-momentum. Then the following subsections define the exclusivity varibles to cut on.

6.1.1 Missing Mass^2

For missing 4-momentum P_{X_i},

$$P_{X_i} = P_{\text{Beam}} + P_{\text{Targ}} - P_{\text{fin},i} \quad ,$$

where $P_{\text{fin},i}$ is the sum of the final state particles not grayed out in **Table 6.1**. We define the missing mass^2, $M^2_{X_i}$, to be

$$M^2_{X_i} = P^2_{X_i} = E^2_{X_i} - \|\vec{\boldsymbol{p}}_{X_i}\|^2 \quad .$$

The expected value, of a perfect measurement, of $M^2_{X_i}$ would be the nominal value-squared of the grayed out particle for the i-th configuration in **Table 6.1**.

6.1.2 Missing Momentum

There are three components to the missing momenta to consider when applying exclusivity cuts: px_{X_2}, py_{X_2}, and pt_{X_2}.

py_{X_2} and py_{X_2} are the transverse x- and y- components and pt_{X_2} the magnitude of P_{X_2}:

$$pt_{X_2} = \sqrt{px^2_{X_2} + py^2_{X_2}} \quad .$$

The expected value, in a perfect measurement would have all of these be identically zero.

6.1.3 Missing Energy

The missing energy, E_{X_2} is just the energy component of P_{X_2}. The expected value, in a perfect measurement, would have this be identically zero.

6.1.4 Cone angle

Cone angle, θ, is the angle between the 3-vectors of the missing and measured particle, following from:

$$\cos\theta = \frac{\vec{\boldsymbol{p}}_{X_2} \cdot \vec{\boldsymbol{p}}_{\pi^0}}{\|\vec{\boldsymbol{p}}_{X_2}\|\|\vec{\boldsymbol{p}}_{\pi^0}\|} \quad .$$

The expected value, in a perfect measurement, would have this be identically zero.

6.1.5 Coplanarity Angle

The coplanarity angle measures how coplanar $^4\mathrm{He}'$ and the produced particle, π^0. Practically, this is measured by measuring the angle between the normal vectors of the plane defined by the virtual photon and final state helium; and the virtual photon and the produced particle. Let the norms to the planes $P1$ and $P2$ be defined as:

$$\begin{aligned} \vec{\boldsymbol{p}}_{P1} &= \vec{\boldsymbol{p}}_{^4\mathrm{He}} \times \vec{\boldsymbol{p}}_{\gamma^*} \\ \vec{\boldsymbol{p}}_{P2} &= \vec{\boldsymbol{p}}_{^4\mathrm{He}} \times \vec{\boldsymbol{p}}_{\pi^0} \end{aligned} \quad .$$

Then $\Delta\phi$ follows from

$$\cos\Delta\phi = \frac{\vec{\boldsymbol{p}}_{P1} \cdot \vec{\boldsymbol{p}}_{P2}}{\|\vec{\boldsymbol{p}}_{P1}\|\|\vec{\boldsymbol{p}}_{P2}\|} \quad .$$

The expected value, in a perfect measurement, would have this be identically zero.

6.2 Cuts Applied to EG6

6.2.1 Exclusivity Cuts

Table 6.2 outlines the means (μ), widths (σ), mins, and maxes of the exclusivity cuts used in the previous analysis [5]. A 3σ and θ cut is applied to all events.

	Mean (μ)	**Width (σ)**	**Units**
$M^2_{X_0}$	1. 4079e+01	1.138e+00	$(\mathrm{GeV}/c^2)^2$
$M^2_{X_2}$	−0. 0050e+00	0.016e+00	$(\mathrm{GeV}/c^2)^2$
$\Delta\phi$	1. 4000e−01	0.460e+00	deg.
	Min.	**Max.**	**Units**
θ	0. 0	2.5	deg.

Table 6.2: Coherent DVπ^0P Cut Values [5]

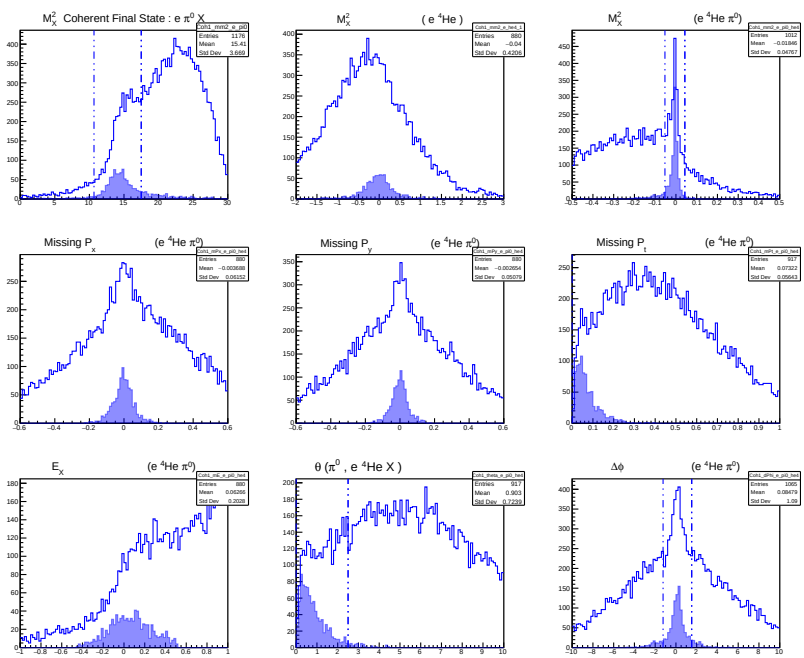

Fig. 6.1: Exclusivity cuts on 4 variables shown with dashed vertical lines. The events passing all other cuts except for its own cut are highlighted in light blue. All other events detecting an electron, helium-4, and two photons is the unshaded histogram.

6.2.2 Additional Photon and Photon Pair Cuts

To compare event selection methods between previous work and this work, involving kinematic fitting, additional cuts [5] were applied to the exclusivity cuts. These cuts involve photon pairs and were made in an effort to help clean the signal. Since we are looking for π^0's, an invariant mass cut of two photons of 3σ (see **Table 6.3**) is applied to all events. Additionally, cuts were made to characterize the produced π^0 in the given kinematics, listed in **Table 6.3**.

	Mean (μ)	**Width (σ)**	**Units**
$M_{\gamma\gamma}$	0.134	0.01	GeV/c^2
	Min.	**Max.**	**Units**
$\Delta X_{\gamma_1,\gamma_2}$	3.00	7.00	cm
p_{π^0}	3.00	—	GeV/c
p_{γ_2}	0.40	—	GeV/c

Table 6.3: Photon and Photon Pair Cuts

Here,

- $\Delta X_{\gamma_1,\gamma_2}$ is the distance between the two photons on the face of the IC.
- p_{π^0} is the momentum magnitude of the π^0 formed from the two photons.
- p_{γ_2} is the momentum magnitude of the lower energy photon.

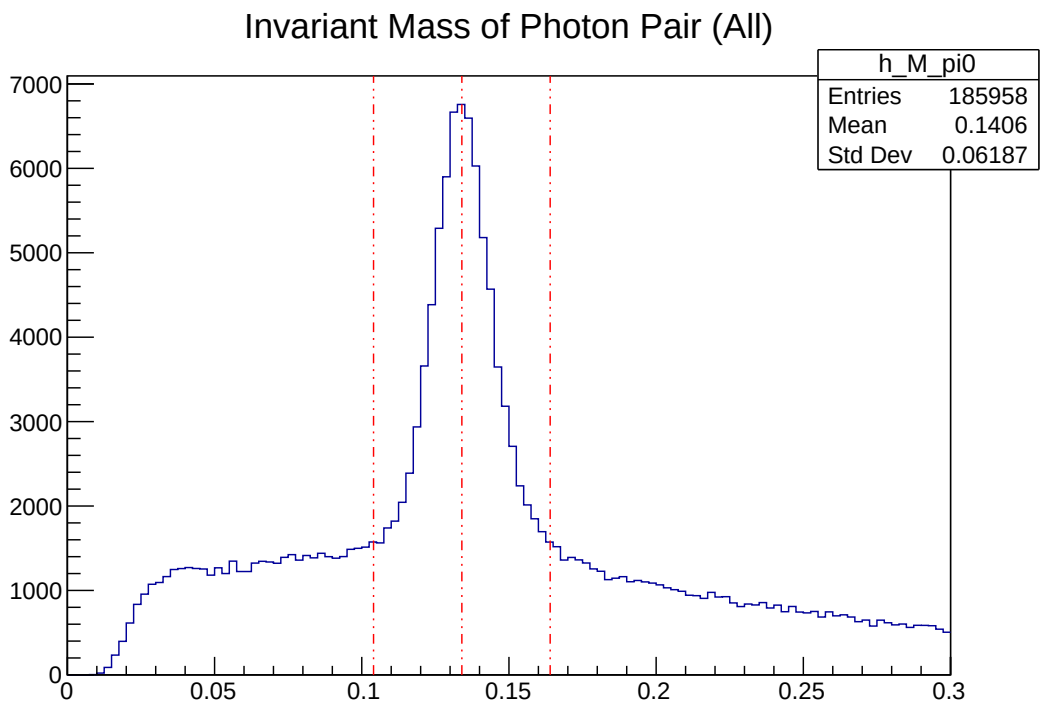

Fig. 6.2: The invariant mass distribution of two photons in the IC. The central vertical dashed line is the nominal value and the ones to the left and right are the $\pm 3\sigma$ cut values.

Events passing all of these cuts are taken to be coherent DVπ^0P events. These events will be used to extract a beam spin asymmetry.

Chapter 7

Event Selection Method II: Kinematic Fitting

7.1 Formalism

An alternative to selecting events from a series of user-defined cuts is to apply kinematic fitting. Kinematic fitting takes in a set of measurements; the detectors' known resolutions and studied errors; a set of constraints; and produces a set of measurements that better satisfies the constraints. Measurements of momentum vectors along with conservation of momentum and energy of an exclusive process are ideal candidates for this procedure and additional constraints can be added as needed.

7.1.1 Pre-fit: Setting up

This method is a least squares fit that follow the recipe using Lagrange multipliers. The Lagrange multipliers are free parameters that extremizes a Lagrangian that balances the minimization of a χ^2 while satisfying a set of constraints. Thus, the ingredients that need to be constructed are χ^2 and a set of constraints. The following sections uses notation mostly from [14, 15] and a bit from [13, 18].

7.1.1.1 Constructing Constraints

Let $\vec{\boldsymbol{\eta}}$ be a vector of n-measured variables. Then the true vector of the n-variables, $\vec{\boldsymbol{y}}$, will have an associated error vector of n-variables, $\vec{\boldsymbol{\varepsilon}}$. They are related simply by:

$$\vec{\boldsymbol{y}} = \vec{\boldsymbol{\eta}} + \vec{\boldsymbol{\varepsilon}}$$

If there are, say m, unmeasured variables too, then they can be put in a vector, $\vec{\boldsymbol{x}}$. The two vectors, $\vec{\boldsymbol{x}}$ and $\vec{\boldsymbol{y}}$, are then related by r constraint equations, indexed by k:

$$f_k\left(\vec{\boldsymbol{x}}, \vec{\boldsymbol{y}}\right) = 0$$

Suppose $\vec{\boldsymbol{x}}^0$ and $\vec{\boldsymbol{y}}^0$ are our best guess or measurements of the vectors $\vec{\boldsymbol{x}}$ and $\vec{\boldsymbol{y}}$, respectively. Then Taylor expanding to first order each $f_k\left(\vec{\boldsymbol{x}}, \vec{\boldsymbol{y}}\right)$ about $\vec{\boldsymbol{x}}^0$ and $\vec{\boldsymbol{y}}^0$ gives:

$$f_k\left(\vec{\boldsymbol{x}}, \vec{\boldsymbol{y}}\right) \approx f_k\left(\vec{\boldsymbol{x}}^0, \vec{\boldsymbol{y}}^0\right) + \sum_{i=0}^{m} \left(\frac{\partial f_k}{\partial x_i}\right)\Bigg|_{\left(\vec{\boldsymbol{x}}^0, \vec{\boldsymbol{y}}^0\right)} \left(x_i - x_i^0\right) + \sum_{j=0}^{n} \left(\frac{\partial f_k}{\partial y_j}\right)\Bigg|_{\left(\vec{\boldsymbol{x}}^0, \vec{\boldsymbol{y}}^0\right)} \left(y_j - y_j^0\right)$$

where x_i, y_j are the ith and jth components of $\vec{\boldsymbol{x}}$, $\vec{\boldsymbol{y}}$

and x_i^0, y_j^0 are the ith and jth components of $\vec{\boldsymbol{x}}^0$, $\vec{\boldsymbol{y}}^0$, respectively.

If the initial guesses or measurements are insufficient (i.e. χ^2 not minimized, see **Section 7.1.1.2**), better $\vec{\boldsymbol{y}}$ and $\vec{\boldsymbol{x}}$ can be obtained from repeated linearization. So for the ν-th iteration, we have:

$$f_k^\nu := f_k\left(\vec{\boldsymbol{x}}^\nu, \vec{\boldsymbol{y}}^\nu\right) \approx f_k\left(\vec{\boldsymbol{x}}^{\nu-1}, \vec{\boldsymbol{y}}^{\nu-1}\right) + \sum_{i=0}^{m}\left(\frac{\partial f_k}{\partial x_i}\right)^\nu \left(x_i^\nu - x_i^{\nu-1}\right) + \sum_{j=0}^{n}\left(\frac{\partial f_k}{\partial y_j}\right)^\nu \left(y_j^\nu - y_j^{\nu-1}\right) \tag{7.1}$$

that depends just on the previous, $(\nu-1)$-th iteration, where *

$$\begin{aligned}\left(\frac{\partial f_k}{\partial x_i}\right)^\nu &:= \left(\frac{\partial f_k\left(\vec{\boldsymbol{x}}, \vec{\boldsymbol{y}}\right)}{\partial x_i}\right)\Bigg|_{\left(\vec{\boldsymbol{x}}^{\nu-1}, \vec{\boldsymbol{y}}^{\nu-1}\right)} \\ \left(\frac{\partial f_k}{\partial y_j}\right)^\nu &:= \left(\frac{\partial f_k\left(\vec{\boldsymbol{x}}, \vec{\boldsymbol{y}}\right)}{\partial y_j}\right)\Bigg|_{\left(\vec{\boldsymbol{x}}^{\nu-1}, \vec{\boldsymbol{y}}^{\nu-1}\right)}\end{aligned} .$$

For convenience, let's introduce

$$\begin{aligned} A_{ij}^\nu &:= \left(\frac{\partial f_i}{\partial x_j}\right)^\nu \\ B_{ij}^\nu &:= \left(\frac{\partial f_i}{\partial y_j}\right)^\nu \\ c_i^\nu &:= f_i\left(\vec{\boldsymbol{x}}^{\nu-1}, \vec{\boldsymbol{y}}^{\nu-1}\right)\end{aligned} , \tag{7.2}$$

and

$$\begin{aligned} \vec{\boldsymbol{\xi}}^\nu &:= \vec{\boldsymbol{x}}^\nu - \vec{\boldsymbol{x}}^{\nu-1} \\ \vec{\boldsymbol{\delta}}^\nu &:= \vec{\boldsymbol{y}}^\nu - \vec{\boldsymbol{y}}^{\nu-1} \\ \vec{\boldsymbol{\epsilon}}^\nu &:= \vec{\boldsymbol{y}}^\nu - \vec{\boldsymbol{\eta}} = \vec{\boldsymbol{y}}^\nu - \vec{\boldsymbol{y}}^0\end{aligned} .$$

* The reasons for labeling the iteration index for the derivatives ν and not $(\nu-1)$ will become apparent later in implementing the fit.

Then, since $f_k(\vec{\boldsymbol{x}}, \vec{\boldsymbol{y}}) \equiv 0 \;\; \forall k$, **Eq. 7.1** can be written in succinct matrix form as:

$$\vec{\mathbf{0}} \equiv A^{\nu} \vec{\boldsymbol{\xi}}^{\nu} + B^{\nu} \vec{\boldsymbol{\delta}}^{\nu} + \vec{\boldsymbol{c}}^{\nu} \tag{7.3}$$

where A^{ν} and B^{ν} are $(r \times n)$ and $(r \times m)$ matrices with components A^{ν}_{ij} and B^{ν}_{ij}, respectively, as defined by **Eqs. 7.2**. These will be our constraints moving forward.

7.1.1.2 Constructing χ^2

Now, if the correlations between the measured values are well understood, a covariance matrix, C_{η}, can be constructed from a vector of the resolution errors of $\vec{\boldsymbol{\eta}}$ (namely, $\vec{\boldsymbol{\sigma}}_{\eta}$), and a symmetric correlation matrix, ρ_{η}, whose components, $(\rho_{\eta})_{ij} \in [-1, 1]$, house pairwise correlations coefficients between components η_i and η_j:

$$C_{\eta} = \vec{\boldsymbol{\sigma}}_{\eta} \rho_{\eta} \vec{\boldsymbol{\sigma}}^{T}_{\eta} \quad .$$

Then let's define χ^2, to account for correlations, for the ν-th iteration, as:

$$\chi^2_{\nu} = (\vec{\boldsymbol{\epsilon}}^{\nu})^T \, C^{-1}_{\eta} \, \vec{\boldsymbol{\epsilon}}^{\nu}.$$

Note, if there are no correlations, then ρ_{η} is the unit matrix and so the covariance matrix becomes just a diagonal matrix of the variances, $C_{\eta} = \mathrm{diag}\left(\overrightarrow{\boldsymbol{\sigma}^{\mathbf{2}}_{\boldsymbol{\eta}}}\right)$. In this case:

$$\sum_{i=0}^{n} \frac{\left(y^{\nu}_i - y^0_i\right)^2}{\left(\sigma^2_{\eta}\right)_i} = \sum_{i=0}^{n} \frac{\left(y^{\nu}_i - \eta_i\right)^2}{\left(\sigma^2_{\eta}\right)_i} = \sum_{i=0}^{n} \frac{\left(\epsilon^{\nu}_i\right)^2}{\left(\sigma^2_{\eta}\right)_i}$$

becomes the recognizable χ^2, that follows a χ^2-distribution for n degrees of freedom.

7.1.2 Fitting

Given this χ^2 and the set of constraints above, we naturally introduce a Lagrangian, $\mathcal{L}$, with Lagrange multipliers $\vec{\boldsymbol{\mu}}$ such that:

$$\mathcal{L}\left(\vec{\boldsymbol{\mu}}, \vec{\boldsymbol{\delta}}, \vec{\boldsymbol{\xi}}\right) = \vec{\boldsymbol{\epsilon}}^T C_\eta^{-1} \vec{\boldsymbol{\epsilon}} + 2\vec{\boldsymbol{\mu}}^T \left(A\vec{\boldsymbol{\xi}} + B\vec{\boldsymbol{\delta}} + \vec{\boldsymbol{c}}\right) \tag{7.4}$$

is to be minimized.

7.1.2.1 Solving for Fitted Values

Explicitly, with the iteration index ν, the minimization conditions are:

$$\begin{aligned}
\vec{\boldsymbol{0}} &\equiv \frac{1}{2}\left(\frac{\partial \mathcal{L}}{\partial \vec{\boldsymbol{\delta}}}\right)^\nu = C_\eta^{-1} \vec{\boldsymbol{\epsilon}}^\nu + (B^\nu)^T \vec{\boldsymbol{\mu}}^\nu \\
\vec{\boldsymbol{0}} &\equiv \frac{1}{2}\left(\frac{\partial \mathcal{L}}{\partial \vec{\boldsymbol{\mu}}}\right)^\nu = A^\nu \vec{\boldsymbol{\xi}}^\nu + B^\nu \vec{\boldsymbol{\delta}}^\nu + \vec{\boldsymbol{c}}^\nu \\
\vec{\boldsymbol{0}} &\equiv \frac{1}{2}\left(\frac{\partial \mathcal{L}}{\partial \vec{\boldsymbol{\xi}}}\right)^\nu = (A^\nu)^T \vec{\boldsymbol{\mu}}^\nu
\end{aligned} \tag{7.5}$$

Solving for such $\vec{\boldsymbol{\mu}}^\nu$, $\vec{\boldsymbol{\delta}}^\nu$, $\vec{\boldsymbol{\xi}}^\nu$ that satisfy **Eqs. 7.5**s' conditions results in:

$$\begin{aligned}
\vec{\boldsymbol{\xi}}^\nu &= -C_x^\nu \left(A^\nu\right)^T C_B^\nu \vec{\boldsymbol{r}}^\nu \\
\vec{\boldsymbol{\mu}}^\nu &= C_B^\nu \left(A^\nu \vec{\boldsymbol{\xi}}^\nu + \vec{\boldsymbol{r}}^\nu\right) \\
\vec{\boldsymbol{\delta}}^\nu &= -C_\eta \left(B^\nu\right)^T \vec{\boldsymbol{\mu}}^\nu - \vec{\boldsymbol{\epsilon}}^{\nu-1}
\end{aligned} \tag{7.6}$$

where C_B, C_x, and $\vec{\boldsymbol{r}}^\nu$ are defined for convenience as

$$\begin{aligned}
C_B^\nu &:= \left[B^\nu C_\eta \left(B^\nu\right)^T\right]^{-1} \\
C_x^\nu &:= \left[\left(A^\nu\right)^T C_B^\nu A^\nu\right]^{-1} \\
\vec{\boldsymbol{r}}^\nu &:= \vec{\boldsymbol{c}}^\nu - B^\nu \vec{\boldsymbol{\epsilon}}^{\nu-1}
\end{aligned} \tag{7.7}$$

To see this explicitly, see **Appendix D**.

With these vectors that satisfy the minimization condition, we can finally form our new fitted vectors $\vec{\boldsymbol{x}}$ and $\vec{\boldsymbol{y}}$:

$$\begin{aligned} \vec{\boldsymbol{x}}^{\nu} &= \vec{\boldsymbol{x}}^{\nu-1} + \vec{\boldsymbol{\xi}}^{\nu} \\ \vec{\boldsymbol{y}}^{\nu} &= \vec{\boldsymbol{y}}^{\nu-1} + \vec{\boldsymbol{\delta}}^{\nu} \end{aligned} \tag{7.8}$$

7.1.2.2 Minimizing χ^2

A simple minimization of χ^2 is deployed by iterating (at least twice and no more than 100 times) over the fit and stopping when one of the conditions in the following algorithm are met (let χ^2_ν represent χ^2 for the last iteration, `n_iterations` represent the current number of iterations, `n_consecutive_increases` represent the current number of consecutive χ^2 increases, and CL is the current confidence level):

```
if( n_iterations == 0 )
```
$\quad \chi^2_\nu = \chi^2_{\nu+1}$
```
  reiterate
if( n_consecutive_increases > 1 )
  stop
```
if($\left|\chi^2_{\nu+1} - \chi^2_\nu\right| / \chi^2_\nu < 10^{-5}$)
```
  stop
```

...

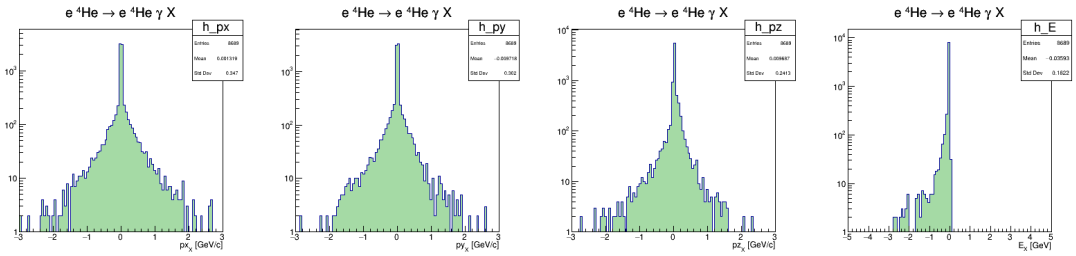

Fig. 7.1: Evaluated constraints of fitted variables

```
if( CL < 10^-8 )
    stop
if ( χ²_{ν+1} > χ²_ν )
    n_consecutive_increases++
else
    n_consecutive_increases = 0
    χ²_ν = χ²_{ν+1}
    reiterate
```

The choice to have a preliminary cut on the confidence level (CL) becomes evident when looking at the evaluated constraints. Consider the dataset used for coherent DVCS [6], which best illustrates this. The fitted values of the evaluated constraints for p_x, p_y, p_z and E of what is left over, X, in the process $e\ ^4\text{He} \rightarrow e\ ^4\text{He}\ \gamma X$, can be seen before this preliminary cut (**Fig. 7.1**). The tails in these distributions demonstrates that χ^2 is not minimized within the default number of iterations (100).

The cut is made at $CL = 10^{-8}$ which corresponds to events with large χ^2. These events start with very low confidence level/high χ^2 have a very low probability that the χ^2 would minimize and in turn that the fit algorithm will constrain the variables sufficiently. **Fig. 7.2a** shows events failing this preliminary cut do indeed account for these tail. The events passing this cut do constrain these fits appropriately, as seen in **Fig. 7.2b**. This threshold cut's effect on the constraints also holds true for the process of interest in this analysis, $e\ {}^4\text{He} \rightarrow e\ {}^4\text{He}\ \pi^0$. This χ^2 minimization process will be used going forward.

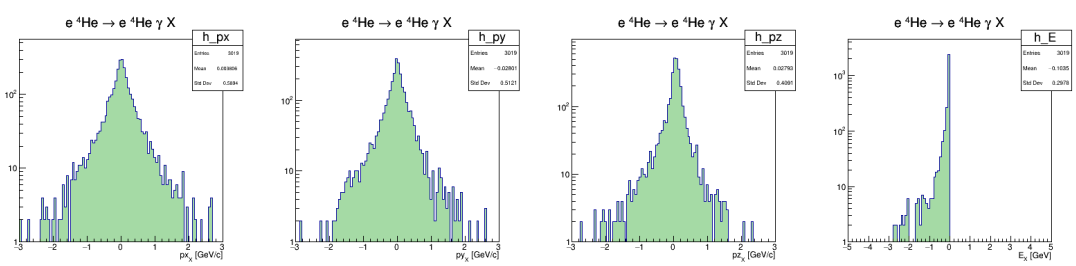

(a) $CL \leq 10^{-8}$ events

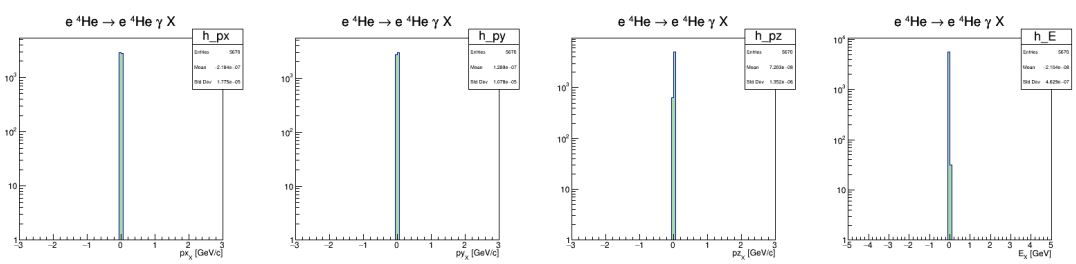

(b) $CL \geq 10^{-8}$ events

Fig. 7.2: Evaluated constraints of fitted variables before and after threshold cut

7.1.2.3 New Errors from Fit

The new covariance matrices, obtained from propagation of errors (See [13]), are C_x^ν (See **Eq. 7.7**) and C_y^ν :

$$\begin{aligned} C_y^\nu &= \left(\frac{\partial \vec{\boldsymbol{y}}}{\partial \vec{\boldsymbol{\eta}}}\right) C_\eta \left(\frac{\partial \vec{\boldsymbol{y}}}{\partial \vec{\boldsymbol{\eta}}}\right)^T \\ &= C_\eta - C_\epsilon^\nu \end{aligned} ,$$

where C_ϵ^ν and its intermediate matrices are defined as:

$$\begin{aligned} C_\epsilon^\nu &:= C_\eta G^\nu C_\eta - C_\eta H^\nu C_x^\nu \left(H^\nu\right)^T C_\eta; \\ G^\nu &:= \left(B^\nu\right)^T C_B^\nu B^\nu \\ H^\nu &:= \left(B^\nu\right)^T C_B^\nu A^\nu \end{aligned} .$$

7.1.3 Post-fit: Fit Quality

To check on the quality of the fit, we look to two sets of distributions: The **Confidence Level distribution** and the **Pull distributions**. Again, omission of the iteration index ν denotes the best fitted, final values.

7.1.3.1 Confidence Level

Since $\chi^2 (= \vec{\boldsymbol{\epsilon}}^T C_\eta^{-1} \vec{\boldsymbol{\epsilon}})$ will produce an χ^2-distribution for N degrees of freedom, let's define the confidence level, CL, as:

$$CL := \int_{x=\chi^2}^{\infty} f_N\left(x\right) \mathrm{d}x$$

where $f_N\left(x\right)$ is the χ^2 probability density function (PDF) with N degrees of freedom. For a kinematic fit, $N = n_{\text{constraints}} - n_{\text{unmeas.}}$. The fit is said to be an NC-fit.

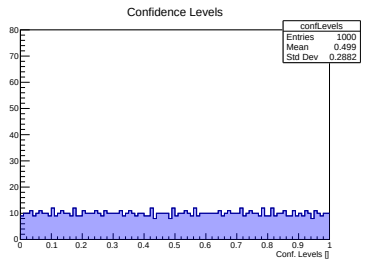

Fig. 7.3: Example of confidence level distribution without background using toy data.

Characteristics

Since this is the complement of a cumulative distribution function (CDF), we can expect it to have certain characteristics:

- If there is no background in the fit, the distribution is uniform/flat (See **Fig. 7.3**).
- In the presence of background, which need not follow a χ^2-distribution, there will be a sharp rise as $CL \to 0$, corresponding to large calculated χ^2 (See **Fig. 7.4a**).

Cutting out the sharp rise as $CL \to 0$ will cut out the much of the background while keeping much of the signal intact (See **Fig. 7.4b**). This is the confidence level cut (CLC).

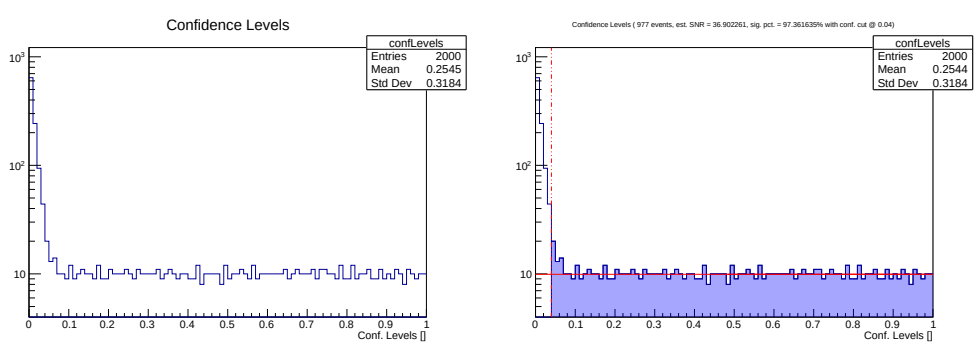

(a) Signal + background of toy model. **(b)** Selected events from cut (highlighted in blue).

Fig. 7.4: Confidence level distributions of toy model before (left) and after (right) CLC.

7.1.3.2 Pull Distributions

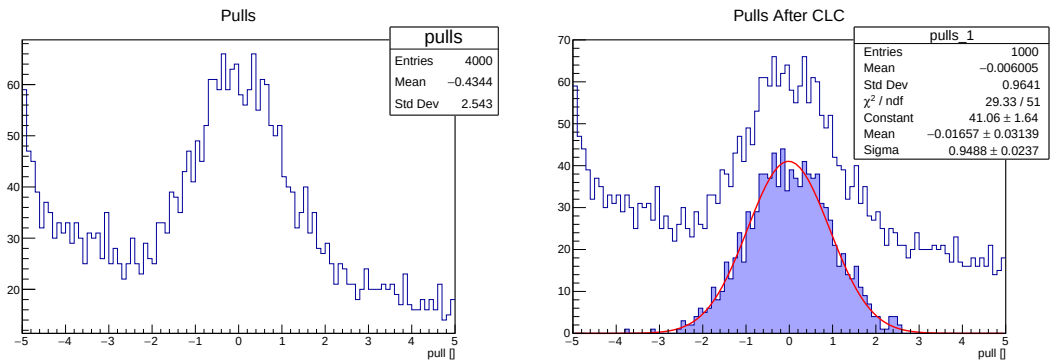

(a) Pull distribution of all events. **(b)** Pull distribution after CLC (highlighted in blue).

Fig. 7.5: Pull distribution before (left) and and after (right) a CLC.

Background can creep in with low χ^2 since background need not follow any particular distribution. To protect against this, pulls are also calculated and their distributions are observed. Additionally, the pull distributions after the CLC gives insight into whether the covariance matrix is correctly taking into account all pairwise correlations between the variables.

Let's introduce $\vec{z}$ to house the pulls, z_i, defined as

$$z_i := \frac{\epsilon_i}{\sigma_{\epsilon_i}} = \frac{y_i - \eta_i}{\sqrt{\sigma^2_{y_i} - \sigma^2_{\eta_i}}} \quad .$$

Then these pull distributions allows us to see how well both the covariance matrix, along with the CLC does by showing how much the accepted measured variables have to move to satisfy the constraints with respect to the resolutions of the covariance matrix.

Characteristics

Since these are normalized differences, the distributions should be normally distributed and have:

- Mean: 0
- Width: 1

All of these characteristics are exhibited in **Fig. 7.5b**, the pull distribution for a single measured variable, where the blue highlighted distribution are the events selected from the confidence level cut.

Now that kinematic fitting is defined and its characteristics are laid out, we can now mold a kinematic fit appropriate for exclusive processes the EG6 experiment seeks to study.

Chapter 8

Kinematic Fitting Applied to EG6

Kinematic fitting was written, compiled, and implemented into a library for this dissertation. Although it was written for this analysis, the open source library [64] is generally formulated with other current and future analyses in mind:

- Any number of custom constraint functions are taken as inputs to kinematic fitting class
- Any number of particles (implemented as a class) involved are taken as inputs
  - Measured and inferred variables are self-contained within particle class
  - Covariance matrices can be taken as in several forms, also self-contained within particles
- Monitoring system to check quality of fit and effect on physical variables. Class provides Confidence level distribution , Pull distributions , and Exclusivity varible distributions

Steps are currently being taken to have it fully implemented with the new CLAS12 era simulations and analyses.

8.1 Assembling Inputs for Covariance Matrix

The most nontrivial aspect of kinematic fitting is having the correct covariance matrix to capture the errors and correlations between measured variables on an event-by-event basis.

For this analysis, a simple approximation of the full covariance matrix is modeled based on simulations studies used to characterize the resolutions. The validity of how representative this approximation of the full covariance matrix is can be checked by observing the quality of all of the pull distributions simultaneously. The resolution studies were done for the original CLAS [57] and then extended to include the IC [8].

The latter showed that the original resolutions needed to be rescaled to match simulated data to experimental data. In the following tables, the variable SF denotes these scaling factors. Since the goal is to study exclusive coherent production of π^0 off ^{4}He, and to check DVCS, the only resolutions that are relevant are the ones involving the scattered electron, the recoiled helium, and any detected photons.

Let $\oplus$ denote the square-root quadrature sum. That is,

$$a \oplus b \oplus c \oplus \ldots := \sqrt{a^2 + b^2 + c^2 + \ldots} \quad .$$

Then with this notation, the explicit forms of the widths are shown in the following subsections. All input momenta will be in GeV/c, all input angles are in units denoted by the subscripts, and all parameters are in units given in the tables.

8.1.1 Electron (DC)

Parameter [Units]	SF_{p1} [ ]	SF_{p2} [ ]	A_p [deg.]	B_p [ ]	C_p [A]	D_p [A]	E_p [1/GeV]	F_p [ ]
Value	3.4	1.5	35	0.7	3375	2099	0.0033	0.0018

Table 8.1: Parameters used to characterize DC p widths

Parameter [Units]	**Index** i [ ]	SF_i [ ]	A_i [rad]	B_i [GeV · rad]
Value	θ	2.5	0.55/1000	1.39/1000
	ϕ	4.0	3.73/1000	3.14/1000

Table 8.2: Parameters used to characterize DC angle widths

The DC widths obtained from simulation studies are

$$\begin{aligned}
\sigma_{p_e}[\text{GeV}] &= p\left(\frac{SF_{p1}}{SF_{p2}}\right)\left(\frac{\theta_{\text{deg.}}}{A_p}\right)^{B_p}\left(\frac{C_p}{D_p}\right)\left[(E_p p)\oplus\frac{F_p}{\beta}\right] \\
\sigma_{\theta_e}[\text{rad}] &= SF_\theta\left[A_\theta\oplus\frac{B_\theta}{p\beta}\right] \\
\sigma_{\phi_e}[\text{rad}] &= SF_\phi\left[A_\phi\oplus\frac{B_\phi}{p\beta}\right]
\end{aligned} \tag{8.1}$$

where

- β is the normalized velocity ($\beta := pc/E$),
- SF_i are the scaling factors used to scale up the resolutions extracted from simulation to better match experiment [8], and
- the parameters A_i through F_i, which account for contributions coming from measurement errors as well as multiple scattering [57], are listed in **Table 8.1** and **Table 8.2** above.

8.1.2 Photon (IC)

Parameter [Units]	SF_E [ ]	A_E [ ]	B_E $\left[\sqrt{\text{GeV}/c}\right]$	C_E [GeV/c]
Value	1.33	0.024	0.033	0.019

Table 8.3: Parameters used to characterize IC momentum width

Parameter [Units]	SF_x [ ]	**Index** i [ ]	A_i $[\sqrt{\text{GeV}/c}\cdot\text{rad}]$	B_i [ ]
Value	1.20	θ	0.003	0.013
		ϕ	0.003	–

Table 8.4: Parameters used to characterize IC angle widths

- -

The IC widths are

$$\begin{aligned}
\sigma_{p_\gamma}[\text{GeV}] &= p\,(SF_E)\left[A_E \oplus \frac{B_E}{\sqrt{p}} \oplus \frac{C_E}{p}\right] \\
\sigma_{\theta_\gamma}[\text{rad}] &= SF_x\left[\frac{A_\theta}{\sqrt{p}} \oplus (B_\theta \theta_{\text{rad.}})\right] \qquad (8.2) \\
\sigma_{\phi_\gamma}[\text{rad}] &= SF_x\left[\frac{A_\phi}{\sqrt{p}}\right]
\end{aligned}$$

where the parameters A_i through C_i are listed in **Table 8.3** and **Table 8.4** above and SF_i are the scaling factors [8].

8.1.3 Photon (EC)

	$\boldsymbol{\delta\theta}$ (rad.)	$\boldsymbol{\delta\phi}$ (rad.)
EC (Photon)	0.004	0.004

Table 8.5: Resolutions for EC

Parameter	$\boldsymbol{A_p}$ $[\sqrt{\mathrm{GeV}/c}]$
Value	0.116

Table 8.6: Parameter used to characterize EC momentum width

The EC widths are

$$\begin{aligned} \sigma_{p_\gamma}[\mathrm{GeV}] &= A_p\sqrt{p} \\ \sigma_{\theta_\gamma}[\mathrm{rad}] &= \delta\theta_{EC} \\ \sigma_{\phi_\gamma}[\mathrm{rad}] &= \delta\phi_{EC} \end{aligned} \tag{8.3}$$

8.1.4 Helium (RTPC)

	$\boldsymbol{\delta p/p}$ (%)	$\boldsymbol{\delta\theta}$ (deg.)	$\boldsymbol{\delta\phi}$ (deg.)
RTPC (Helium)	10.00	4.00	4.00

Table 8.7: Resolutions for RTPC

A complete study of the RTPC errors has not yet been done so they are independent of the kinematics, taking fixed values of their nominal resolutions:

$$\begin{aligned} \sigma_{p_{^4\mathrm{He}}}[\mathrm{GeV}] &= p\,(\delta p/p) \\ \sigma_{\theta_{^4\mathrm{He}}}[\mathrm{rad}] &= \delta\theta_{\mathrm{rad}} \\ \sigma_{\phi_{^4\mathrm{He}}}[\mathrm{rad}] &= \delta\phi_{\mathrm{rad}} \end{aligned} \quad . \tag{8.4}$$

Chapter 9

Validation: $4C$-fit on nuclear DVCS in CLAS EG6

With the procedure outlined and a way to measure the quality of the fit, we can apply it to experimental data and/or simulation. For now, kinematic fitting is used to select events. These events passing a kinematic fit will be compared to events passing exclusivity cuts outlined in **Chapter 6**.

The following kinematic fitting is a $4C$-fit, using the conservation of momentum and energy in an exclusive process as the constraints. The fitting is applied to momentum vectors of the final state particles in the exclusive process:

$$e\,^4\mathrm{He} \rightarrow e'\,^4\mathrm{He}'\gamma \quad .$$

That is, since all particles of this process are measured in CLAS EG6, with the help of the RTPC and IC, there are no unmeasured variables. The measured variables for the fit will be $\bigcup_{\beta}\{p_\beta, \theta_\beta, \phi_\beta\}$, where β loops over all final state particles.

9.1 Setting Up Inputs

9.1.1 Covariance Matrix

A simple approximation of the 9×9 (9 measured variables) covariance matrix with correlations embedded in the variances (See **Section ??**) along the diagonal and zeros elsewhere is used:

$$C_\eta = \mathrm{diag}\left(\sigma^2_{p_e}, \sigma^2_{\theta_e}, \sigma^2_{\phi_e}, \sigma^2_{p_{^4\mathrm{He}}}, \sigma^2_{\theta_{^4\mathrm{He}}}, \sigma^2_{\phi_{^4\mathrm{He}}}, \sigma^2_{p_\gamma}, \sigma^2_{\theta_\gamma}, \sigma^2_{\phi_\gamma}\right) = \begin{bmatrix} \sigma^2_{p_e} & 0 & \dots & \dots & \dots & 0 \\ 0 & \sigma^2_{\theta_e} & \ddots & \ddots & \ddots & \vdots \\ \vdots & \ddots & \ddots & \ddots & \ddots & \vdots \\ \vdots & \ddots & \ddots & \ddots & \ddots & \vdots \\ \vdots & \ddots & \ddots & \ddots & \sigma^2_{\theta_\gamma} & 0 \\ 0 & \dots & \dots & \dots & 0 & \sigma^2_{\phi_\gamma} \end{bmatrix}.$$

Contrary to its appearance, it is important to note that the covariance matrix is constructed event by event, since each width is dependent on combinations of p, θ, and ϕ of each measured particle.

9.1.2 Input Kinematic Vectors

Before constructing our input vectors for the kinematic fit, it would be convenient to introduce some 4-momenta:

$$P_{\mathrm{init}} := P_e + P_{^4\mathrm{He}}$$

$$P_{\mathrm{fin}} := P_{e'} + P_{^4\mathrm{He}'} + P_\gamma$$

Then

$$P_{\text{Exc}} := P_{\text{init}} - P_{\text{fin}} \tag{9.1}$$

houses our 4 constraint equations for exclusivity, since all components of this vector should be zero.

Now, since there are no unmeasured vectors and all measurements in input vectors are final state particles, let's omit the primes (’). The input vectors are then:

$$\vec{\boldsymbol{y_0}} = \vec{\boldsymbol{\eta}} = \begin{bmatrix} p_e \\ \theta_e \\ \phi_e \\ p_{^4\text{He}} \\ \theta_{^4\text{He}} \\ \phi_{^4\text{He}} \\ p_\gamma \\ \theta_\gamma \\ \phi_\gamma \end{bmatrix} \qquad \vec{\boldsymbol{c}} = \begin{bmatrix} (P_{\text{Exc}})_x \\ (P_{\text{Exc}})_y \\ (P_{\text{Exc}})_z \\ (P_{\text{Exc}})_E \end{bmatrix} .$$

9.1.3 Input Kinematic Matrices

In this $4C$-fit, there are no unmeasured variables so B is the only input matrix:

$$B = \begin{bmatrix} \frac{\partial c_1}{\partial \eta_1} & \cdots & \frac{\partial c_1}{\partial \eta_9} \\ \vdots & \ddots & \vdots \\ \frac{\partial c_4}{\partial \eta_1} & \cdots & \frac{\partial c_4}{\partial \eta_9} \end{bmatrix}$$

To see the matrix explicitly, introduce D_β:

$$D_\beta := \begin{bmatrix} -\sin\theta_\beta\cos\phi_\beta & -p_\beta\cos\theta_\beta\cos\phi_\beta & p_\beta\sin\theta_\beta\sin\phi_\beta \\ -\sin\theta_\beta\sin\phi_\beta & -p_\beta\cos\theta_\beta\sin\phi_\beta & -p_\beta\sin\theta_\beta\cos\phi_\beta \\ -\cos\theta_\beta & p_\beta\sin\theta_\beta & 0 \\ -\frac{p_\beta}{E_\beta} & 0 & 0 \end{bmatrix} \tag{9.2}$$

where β is a placeholder for a particle. We can now form the 4×9 (4 constraints, 9 measured variables) matrix, B, by concatenating the three 4×3 (4 constraints, 3 sets of 3 measured variables)D_β matrices:

$$B = \begin{bmatrix} D_e & D_{^4\mathrm{He}} & D_\gamma \end{bmatrix}$$

9.2 Fit Outputs

From just these inputs, all other vectors and matrices from **Section 7.1.2.1** can be constructed and a set of fitted final state momenta can be extracted from the final fitted vector $\vec{\boldsymbol{y}}$.

9.2.1 Confidence Level Distribution

To see how this kinematic fit fared, we look at the confidence level distribution. From **Fig. 9.1**, we see that there is some background from the peak at 0 and a plateau thereafter.

The plateau in the confidence level distribution signifies that there is an underlying distribution that follows our hypothesis that the particles involved are part of an exclusive process, conserving momentum and energy. Otherwise, the calculated χ^2 would not be

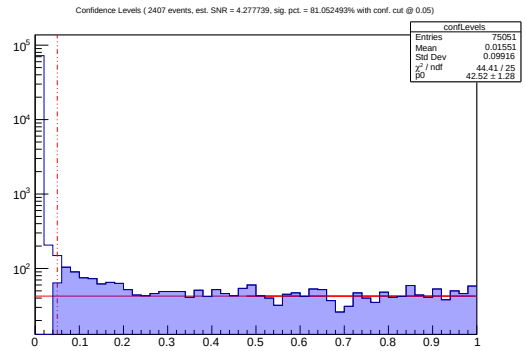

Fig. 9.1: Confidence levels with a cut at 0.05, represented by the red vertical dashed line. Selected events are highlighted light blue (the right half is fitted to straight line to estimate the signal to noise ratio).

coming from a χ^2-distribution and the resulting confidence level distribution would not look uniform at any point (See **Section 7.1.3.1** and [13]). Note that this is the only user-based cut in the entire event selection process.

9.2.2 Pull Distributions

To see how well the confidence level cut does, we look to the pull distributions. If we see each pull normally distributed with a width of 1 and a mean of 0, the quality of the fit along with the confidence level cut are satisfactory. From **Fig. 9.2**, the pull distributions look reasonable. At the very least, the distributions resemble the red curves they ought to be qualitatively.

The pull distributions tell us that although the covariance matrix is diagonal, correlations are reasonably accounted for: the variances along the diagonal have the pair-wise correlations between a particle's p, θ, ϕ embedded in them (See **Eqs. 8.1, 8.2, 8.4**). Additionally, the confidence level cut is rejecting most of the background (events that

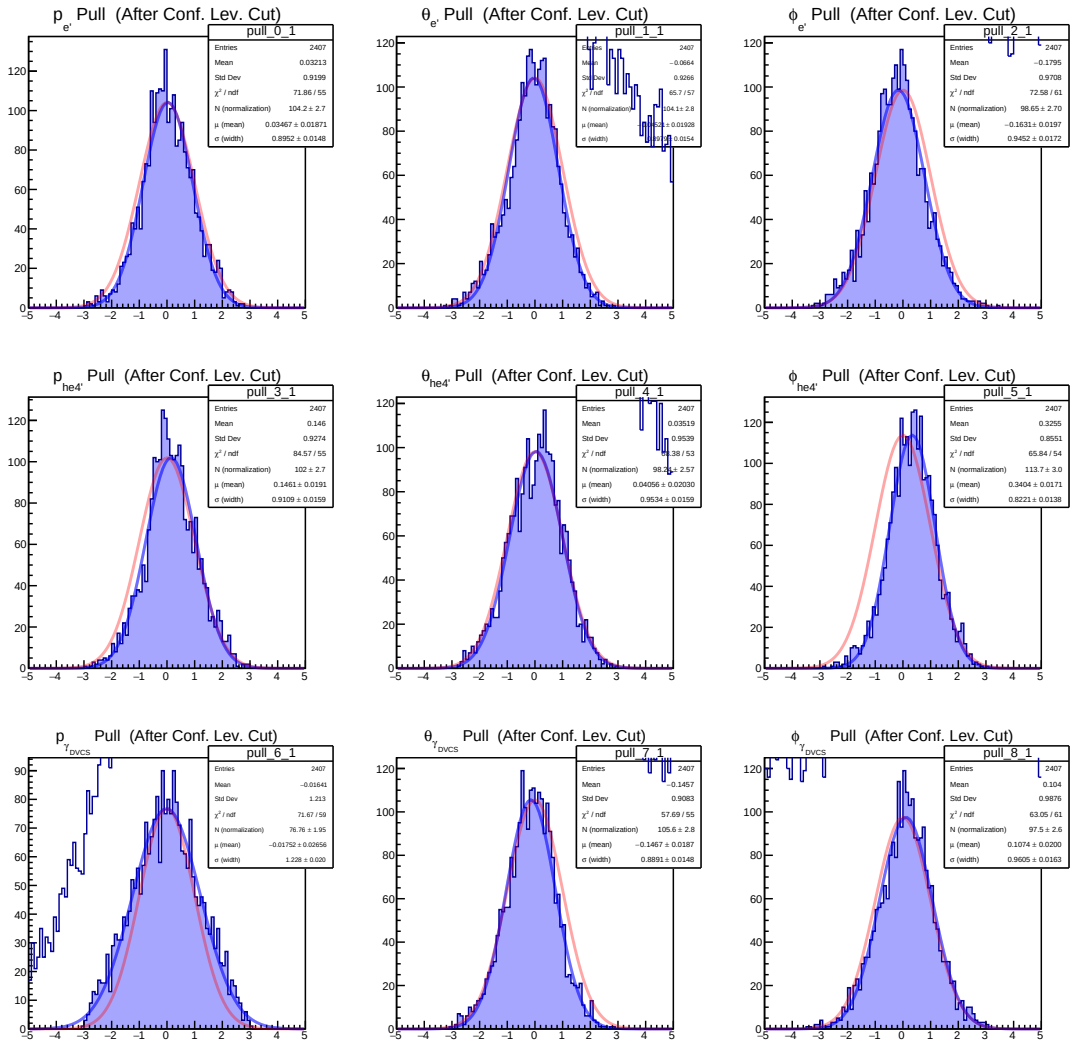

Fig. 9.2: Pull distributions for p, θ, ϕ (left to right) for $e, {}^4\text{He}, \gamma$ (top to bottom). The blue and red curve are a fit to the distribution and what it should be, respectively.

do not conserve momentum and energy of an exclusive process within detectors' errors).

9.3 Fit Results

The quality of the fit as shown in the previous section, **Section 9.2**, shows that the fit is satisfactory for the confidence level cut. The next subsections will show the resulting measured (in blue) and fitted (shaded green) distributions and asymmetries, as compared to the ones in the previous study [6] (in red).

9.3.1 Exclusivity Variable Distributions

The confidence and pull distributions show that it was a good fit but what do the selected events look like? The exclusivity variable distributions show how well the events selected conserve momentum and energy. Ideally, the exclusivity variable distributions will all be δ-function distributions centered at the expected values discussed in **Chapter 6**. Detector resolutions naturally smear these distributions and background events dilute the signal. The goal is to get at the underlying signal.

For the exclusivity cuts in **Chapter 6**, each cut applied shapes all other distributions. With kinematic fitting described in this section, a single cut shapes all of these distributions: the confidence level cut. **Fig. 9.3** shows a comparison between the measured events obtained from exclusivity cuts (in red) and the kinematic fit (in blue); and the fitted events from the kinematic fit (in green).

The measured exclusivity variable distributions are very similar with the exception that the tails from the events passing the kinematic fit are suppressed.

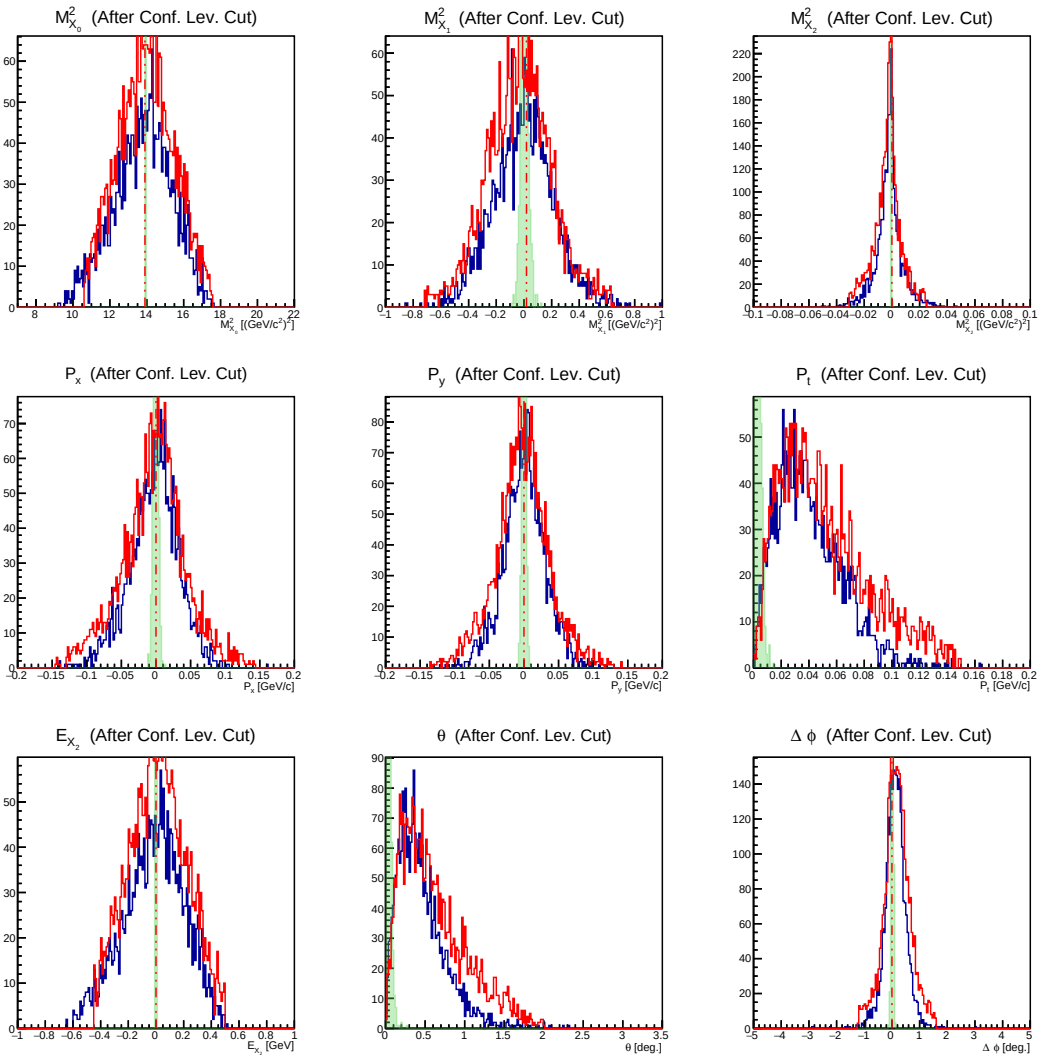

Fig. 9.3: Exclusivity variable distributions for:

- Measured events passing exclusivity cuts (red)

- Measured events passing kinematic fit with 0.05 conf. level cut (blue)

- Fitted events passing kinematic fit with 0.05 conf. level cut (highlighted green)

9.3.2 Beam Spin Asymmetry

The raw* beam spin asymmetry are shown in **Fig. 9.4**. Following from the fact that the exclusivity variable distributions do not look too disimilar between events selected through exclusivity cuts and kinematic fitting, nothing sticks out in the raw asymmetries.

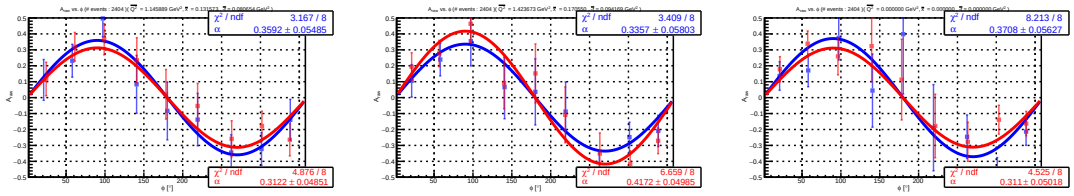

(a) Q^2 bins with edges $\{1.00, 1.28, 1.58, 5.00\}$ $(\mathrm{GeV}/c^2)^2$, integrated over all $x, -t$ bins.

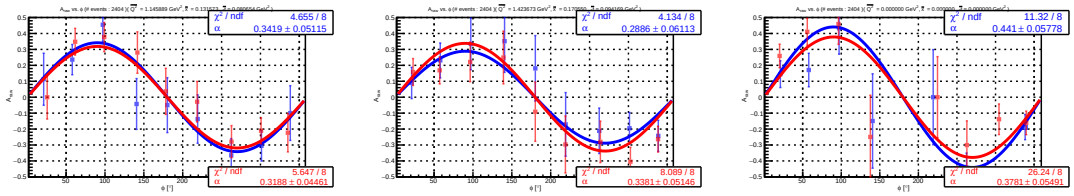

(b) x bins with edges $\{0.000, 0.152, 0.190, 0.500\}$, integrated over all $Q^2, -t$ bins.

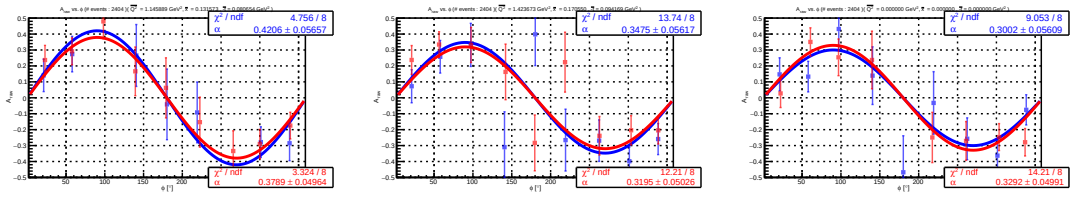

(c) $-t$ bins (with edges $\{0.065, 0.087, 0.103, 1.000\}$) $(\mathrm{GeV}/c^2)^2$, integrated over all Q^2, x bins.

Fig. 9.4: Raw beam spin asymmetry (**Figs. 9.4a, 9.4b, 9.4c**) for:

- Measured events passing exclusivity cuts (red)
- Measured events passing kinematic fit with 0.05 conf. level cut (blue)

* purely statistical: no particular background subtraction or dilution studies applied

Chapter 10

Natural Extension: $4C$-fit on DVπ^0P

The kinematic fitting on DVCS events produced similar events to that which was done with exclusivity cuts, in turn producing similar beam spin asymmetries. This gives confidence into applying it to a much rarer process, coherent electroproduction of π^0 off ^{4}He. The following kinematic fitting is a $4C$-fit, using the conservation of momentum and energy in an exclusive process as the constraints. The fitting is applied to momentum vectors of the final state particles in the exclusive process:

$$e\,^4\mathrm{He} \rightarrow e'\,^4\mathrm{He}'\pi^0 \rightarrow e'\,^4\mathrm{He}'\gamma\gamma \quad .$$

That is, the measured variables for the fit will be $\bigcup_\beta \{p_\beta, \theta_\beta, \phi_\beta\}$, where β loops over all final state particles: $e', {}^4\mathrm{He}', \gamma_1, \gamma_2$.

10.1 Setting Up Inputs

10.1.1 Covariance Matrix

The kinematic fit applied on DVCS seemed to work quite well so the same event by event covariance matrix is constructed:

$$C_\eta = \mathrm{diag}\left(\sigma^2_{p_e}, \sigma^2_{\theta_e}, \sigma^2_{\phi_e}, \sigma^2_{p_{^4\mathrm{He}}}, \sigma^2_{\theta_{^4\mathrm{He}}}, \sigma^2_{\phi_{^4\mathrm{He}}}, \sigma^2_{p_{\gamma_1}}, \sigma^2_{\theta_{\gamma_1}}, \sigma^2_{\phi_{\gamma_1}}, \sigma^2_{p_{\gamma_2}}, \sigma^2_{\theta_{\gamma_2}}, \sigma^2_{\phi_{\gamma_2}}\right)$$

10.1.2 Input Kinematic Vectors and Matrices

Again let's introduce some 4-momenta for convenience:

$$P_{\text{init}} := P_e + P_{^4\text{He}}$$

$$P_{\text{fin}} := P_{e'} + P_{^4\text{He}'} + P_{\gamma_1} + P_{\gamma_2}$$

Then

$$P_{\text{Exc}} := P_{\text{init}} - P_{\text{fin}} \tag{10.1}$$

will hold our constraints.

Omitting the primes(’), the input kinematic vectors and matrix are:

$$\vec{\boldsymbol{y_0}} = \vec{\boldsymbol{\eta}} = \begin{bmatrix} p_e \\ \theta_e \\ \phi_e \\ p_{^4\text{He}} \\ \theta_{^4\text{He}} \\ \phi_{^4\text{He}} \\ p_{\gamma_1} \\ \theta_{\gamma_1} \\ \phi_{\gamma_1} \\ p_{\gamma_2} \\ \theta_{\gamma_2} \\ \phi_{\gamma_2} \end{bmatrix} \quad , \quad \vec{\boldsymbol{c}} = \begin{bmatrix} (P_{\text{Exc}})_x \\ (P_{\text{Exc}})_y \\ (P_{\text{Exc}})_z \\ (P_{\text{Exc}})_E \end{bmatrix} \quad , \quad B = \begin{bmatrix} \frac{\partial c_1}{\partial \eta_1} & \cdots & \frac{\partial c_1}{\partial \eta_{12}} \\ \vdots & \ddots & \vdots \\ \frac{\partial c_4}{\partial \eta_1} & \cdots & \frac{\partial c_4}{\partial \eta_{12}} \end{bmatrix}$$

with no unmeasured inputs.

Explicitly,

$$B = \begin{bmatrix} D_e & D_{^4\mathrm{He}} & D_{\gamma_1} & D_{\gamma_2} \end{bmatrix}$$

where D_β is defined in **Eq. 9.2**.

10.2 Fit Outputs

10.2.1 Confidence Level Distribution

The $4C$-fit produces a confidence level distribution seen in **Fig. 10.1**. A CLC is made at 0.05.

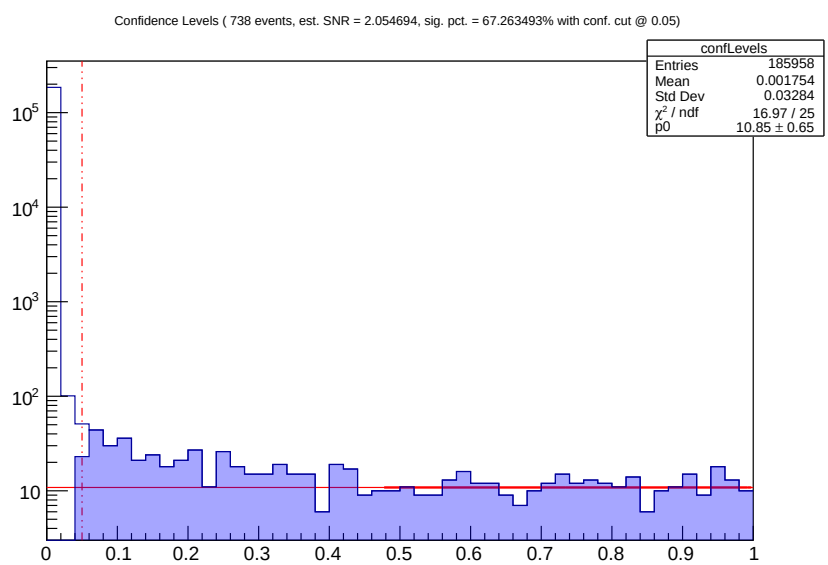

Fig. 10.1: Confidence level distribution with a cut at 0.05, represented by the red vertical dashed line. The events passing the cut are represented by the blue highlighted distribution which the right half is fitted to straight line to estimate the signal to noise ratio.

10.2.2 Pull Distributions

The kinematic fit with the CLC produces the pull distributions in **Fig. 10.2**. These pull distributions too look reasonable.

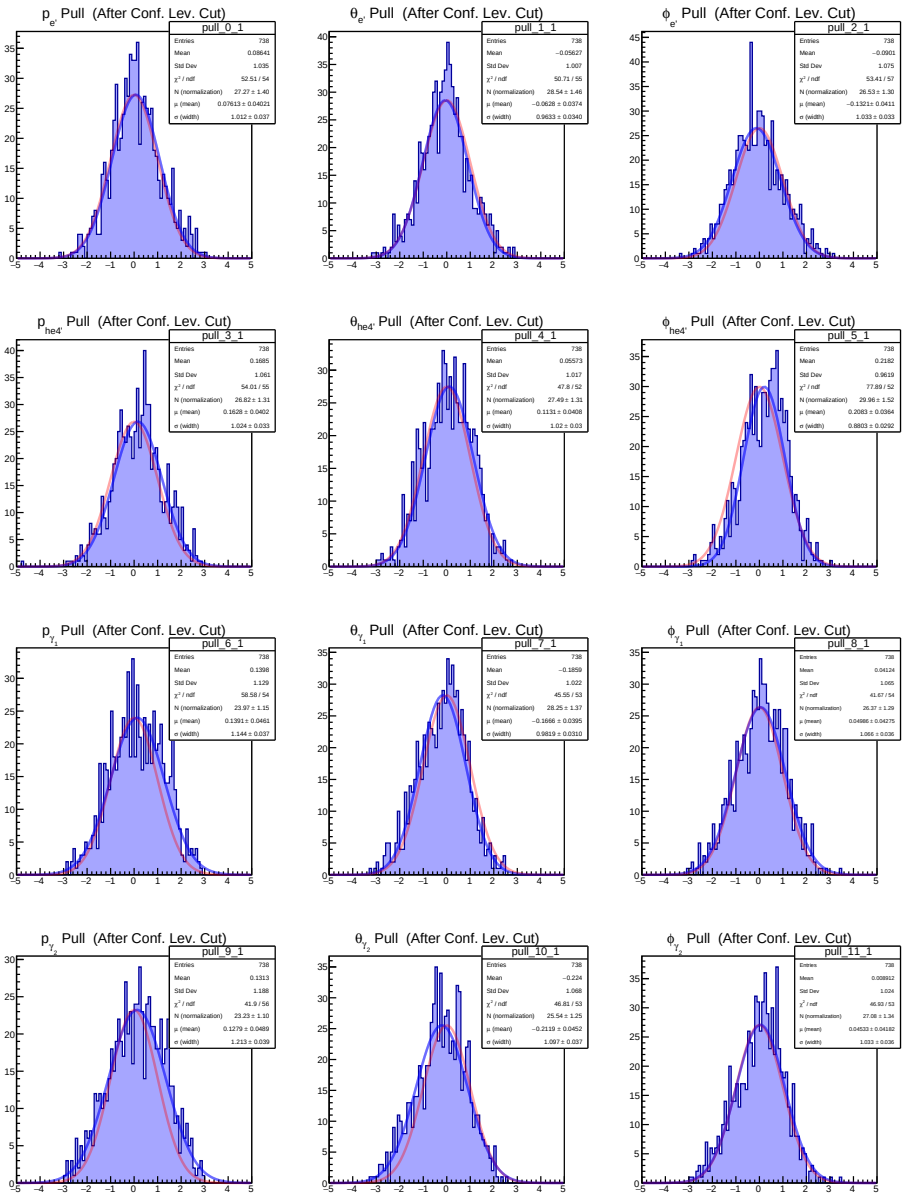

Fig. 10.2: Pull distributions for p, θ, ϕ (left to right) for $e, {}^4\text{He}, \gamma_1, \gamma_2$ (top to bottom). The blue and red curve are a fit to the distribution and what it should be, respectively.

10.3 Fit Results

The quality of the fit as shown in the previous section, **Section 10.2**, shows that the fit is satisfactory for the confidence level cut. The next subsections will show the resulting measured (in blue) and fitted (shaded green) distributions and asymmetries, as compared to the ones in the previous study [5] (in black).

10.3.1 Exclusivity Variable Distributions

Along with the invariant mass distribution, the exclusivity variable distributions show the quality of events selected. For the exclusivity cuts in **Section 6.1**, each cut applied shaped all other distributions. With kinematic fitting described in this section, a single cut shapes all of these distributions: the confidence level cut. **Fig. 10.3** shows a comparison between the measured events obtained from exclusivity cuts (in black) and the kinematic fit (in blue); and the fitted events from the kinematic fit (in green).

The measured exclusivity variable distributions are similar but the tails of missing energy, transverse momentum, and θ_{X_1,π^0} distributions are all sizably suppressed.

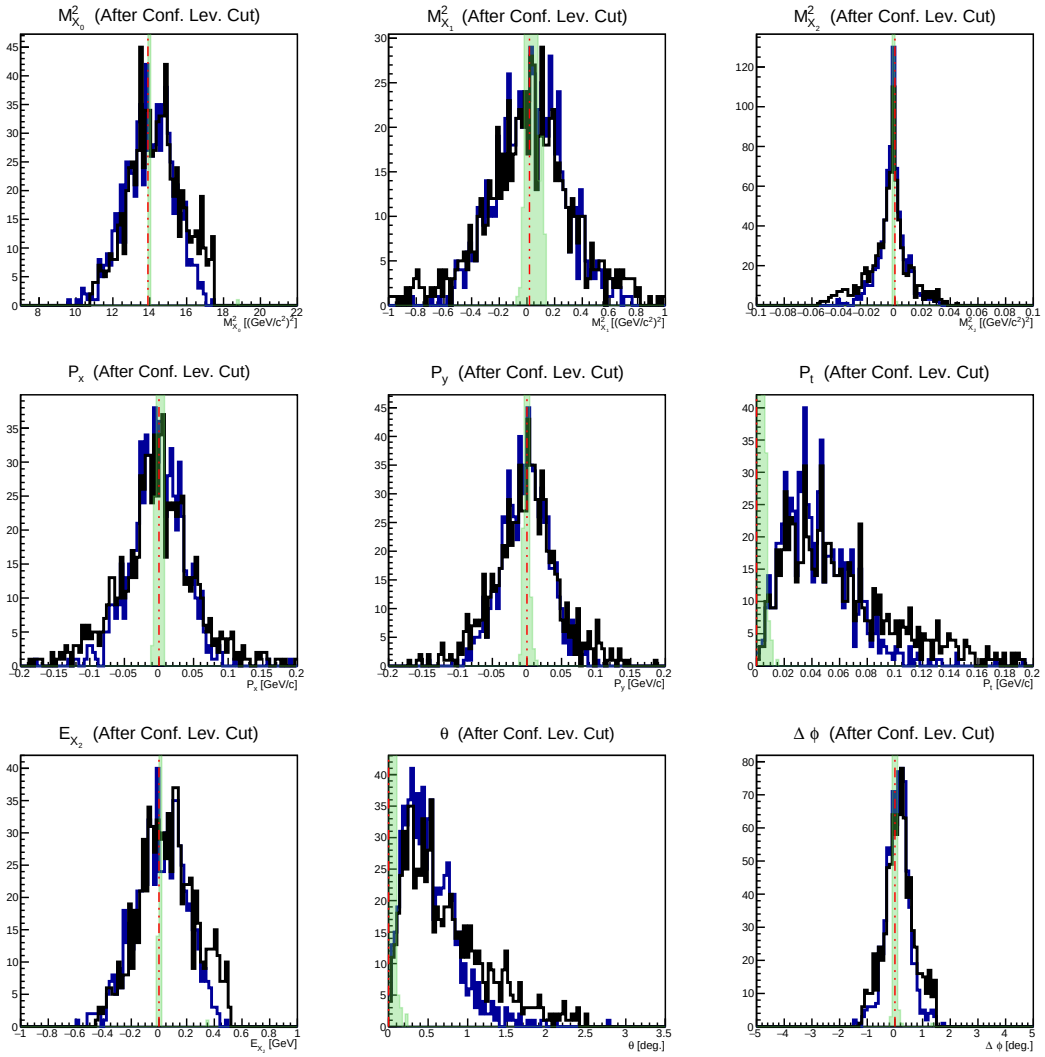

Fig. 10.3: Exclusivity variable distributions, and the expected value (red vertical dashed line) for:

- Measured events passing exclusivity cuts (black)

- Measured events passing kinematic fit with 0.05 conf. level cut (blue)

- Fitted events passing kinematic fit with 0.05 conf. level cut (highlighted green)

10.3.2 Invariant Mass Distribution

Perhaps what best displays the power of kinematic fitting is the fact that even though invariant mass of the π^0 is nowhere mentioned in the fitting, the invariant mass distribution of the two photons shows a clear peak at the nominal value (see **Fig. 10.4**). Using measured 4-momenta, the kinematic fit with conservation of momentum and energy for the exclusive process

$$e\,^4\mathrm{He} \rightarrow e'\,^4\mathrm{He}'\gamma\gamma$$

is already enough to rule out many of the background photon pairs (as compared to **Fig. 6.2**).

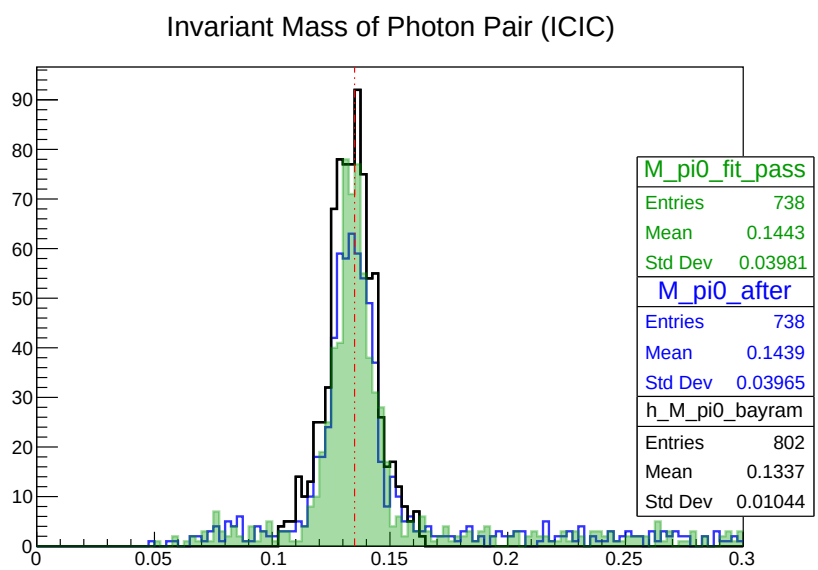

Fig. 10.4: Invariant mass distributions of photon pairs with the nominal PDG π^0 mass being the red dashed line with the same color scheme as the exclusivity variable distribution in **Fig. 10.3**

10.4 Adding π^0 Cut

To clean up the background and to have a better comparison between the exclusivity cuts and the kinemtic fit, the same 3σ invariant mass cut (see **Table 6.3**) is applied to the measured invariant photon pair of the previous section.

This is one way to clean the events but we can do better, discussed in the next section.

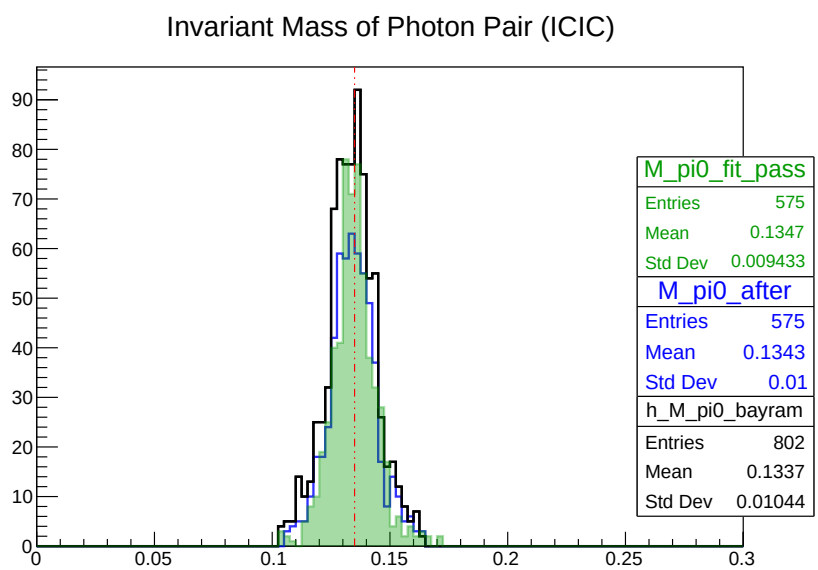

Fig. 10.5: Invariant mass distributions of photon pairs with the nominal PDG π^0 mass being the red dashed line with the same color scheme as the exclusivity variable distribution in **Fig. 10.3**

Chapter 11

Final Fit: $5C$-fit on DVπ^0P

Instead of just relying on exclusivity of

$$e^4\text{He} \rightarrow e'^4\text{He}'\gamma\gamma \quad ,$$

we can fold in that the two photons come from the decay of π^0. That is, we create a $5C$-fit, that simulataneously conserves momentum and energy of the two processes:

$$e^4\text{He} \rightarrow e'^4\text{He}' X_{\pi^0}$$

$$X_{\pi^0} \rightarrow \gamma\gamma$$

Since the momentum of the π^0 is not directly measured but reconstructed from the two photons, there will now be unmeasured variables associated with the missing particle, X_{π^0} $(p_{X_{\pi^0}}, \theta_{X_{\pi^0}}, \phi_{X_{\pi^0}})$. The measured variables for the fit will be the same $\bigcup_\beta \{p_\beta, \theta_\beta, \phi_\beta\}$, where β loops over all final state particles: $e', {}^4\text{He}', \gamma_1, \gamma_2$. This will also fold the invariant mass "cut" into the confidence level cut, leaving one less systematic to worry about. Additionally, the invariant mass "cut" will know about the detectors' resolutions.

11.1 Setting Up Inputs

11.1.1 Covariance Matrix

The covariance matrix is the exact same as the previous one, as there are no additional measured variables added:

$$C_\eta = \mathrm{diag}\left(\sigma^2_{p_e}, \sigma^2_{\theta_e}, \sigma^2_{\phi_e}, \sigma^2_{p_{^4\mathrm{He}}}, \sigma^2_{\theta_{^4\mathrm{He}}}, \sigma^2_{\phi_{^4\mathrm{He}}}, \sigma^2_{p_{\gamma_1}}, \sigma^2_{\theta_{\gamma_1}}, \sigma^2_{\phi_{\gamma_1}}, \sigma^2_{p_{\gamma_2}}, \sigma^2_{\theta_{\gamma_2}}, \sigma^2_{\phi_{\gamma_2}}\right)$$

11.1.2 Input Kinematic Vectors

Before constructing our input vectors for the kinematic fit, let's define some momenta for the π^0:

$$\begin{aligned}
\vec{\boldsymbol{p}}_{X_{\pi^0}} &:= \vec{\boldsymbol{p}}_{\gamma_1} + \vec{\boldsymbol{p}}_{\gamma_2} \\
E_{X_{\pi^0}} &:= \sqrt{\|\vec{\boldsymbol{p}}_{X_{\pi^0}}\|^2 + M^2_{\pi^0}} \quad , \\
P_{X_{\pi^0}} &:= \left(\vec{\boldsymbol{p}}_{X_{\pi^0}}, E_{X_{\pi^0}}\right)
\end{aligned}$$

Here, we explicitly use the nominal PDG value of the π^0 invariant mass, $M_{\pi^0} = 0.1349766\ \mathrm{GeV}/c^2$ [3]. From this we can immediately define our unmeasured/inferred variables:

$$\vec{\boldsymbol{x}}^0 = \begin{bmatrix} p_{X_{\pi^0}} \\ \theta_{X_{\pi^0}} \\ \phi_{X_{\pi^0}} \end{bmatrix} \quad .$$

Similar to previously constructed, the exclusivity constraints come from:

$$\begin{aligned}
P_{\mathrm{init}} &:= P_e + P_{^4\mathrm{He}} \\
P_{\mathrm{fin}} &:= P_{e'} + P_{^4\mathrm{He}'} + P_{X_{\pi^0}}
\end{aligned} \quad .$$

Then our $5C$ constraints are:

$$\begin{aligned} P_{\text{Exc}} &:= P_{\text{init}} - P_{\text{fin}} \\ P_{\text{Decay}} &:= P_{X_{\pi^0}} - (P_{\gamma_1} + P_{\gamma_2}) \end{aligned} .$$

Omitting primes(’), the rest of the input vectors are:

$$\vec{\boldsymbol{y}}^0 = \vec{\boldsymbol{\eta}} = \begin{bmatrix} p_e \\ \theta_e \\ \phi_e \\ p_{^4\text{He}} \\ \theta_{^4\text{He}} \\ \phi_{^4\text{He}} \\ p_{\gamma_1} \\ \theta_{\gamma_1} \\ \phi_{\gamma_1} \\ p_{\gamma_2} \\ \theta_{\gamma_2} \\ \phi_{\gamma_2} \end{bmatrix} , \qquad \vec{\boldsymbol{c}} = \begin{bmatrix} (P_{\text{Exc}})_x \\ (P_{\text{Exc}})_y \\ (P_{\text{Exc}})_z \\ (P_{\text{Exc}})_E \\ (P_{\text{Decay}})_x \\ (P_{\text{Decay}})_y \\ (P_{\text{Decay}})_z \\ (P_{\text{Decay}})_E \end{bmatrix} .$$

Initially, the x-, y-, and z-components of P_{Decay} will be identically zero by definition but after the first iteration, the values will change accordingly.

11.1.3 Input Kinematic Matrices

In this $5C$-fit, there are both measured and unmeasured variables so we have both matrices B and A:

$$B = \begin{bmatrix} \frac{\partial c_1}{\partial \eta_1} & \cdots & \frac{\partial c_1}{\partial \eta_{12}} \\ \vdots & \ddots & \vdots \\ \frac{\partial c_8}{\partial \eta_1} & \cdots & \frac{\partial c_8}{\partial \eta_{12}} \end{bmatrix}$$

$$A = \begin{bmatrix} \frac{\partial c_1}{\partial x_1^0} & \cdots & \frac{\partial c_1}{\partial x_3^0} \\ \vdots & \ddots & \vdots \\ \frac{\partial c_8}{\partial x_1^0} & \cdots & \frac{\partial c_8}{\partial x_3^0} \end{bmatrix} .$$

We can now form the 8×12 (8 constraint equations, 12 measured variables) matrix, B, and 8×3 (8 constraint equations, 3 unmeasured/inferred variables) matrix, A, by concatenating the eight 4×3 (2 sets of 4 constraint equations, 3 variables for each particle) D_β matrices for B and two 4×3 D_β for A:

$$B = \begin{bmatrix} D_e & D_{^4\mathrm{He}} & 0 & 0 \\ 0 & 0 & D_{\gamma_1} & D_{\gamma_2} \end{bmatrix} , \tag{11.1}$$

$$A = \begin{bmatrix} D_{X_{\pi^0}} \\ -D_{X_{\pi^0}} \end{bmatrix} . \tag{11.2}$$

where D_β is defined in **Eq. 9.2**. The zeros from **Eq. 11.1** are 4×3 matrices with all entries 0.

11.2 Fit Outputs

11.2.1 Confidence Level Distribution

The $5C$ fit produced the CL distribution seen in **Fig. 11.1** and a cut at 0.05 is applied. Note that this is the only user-based cut in the entire event selection process.

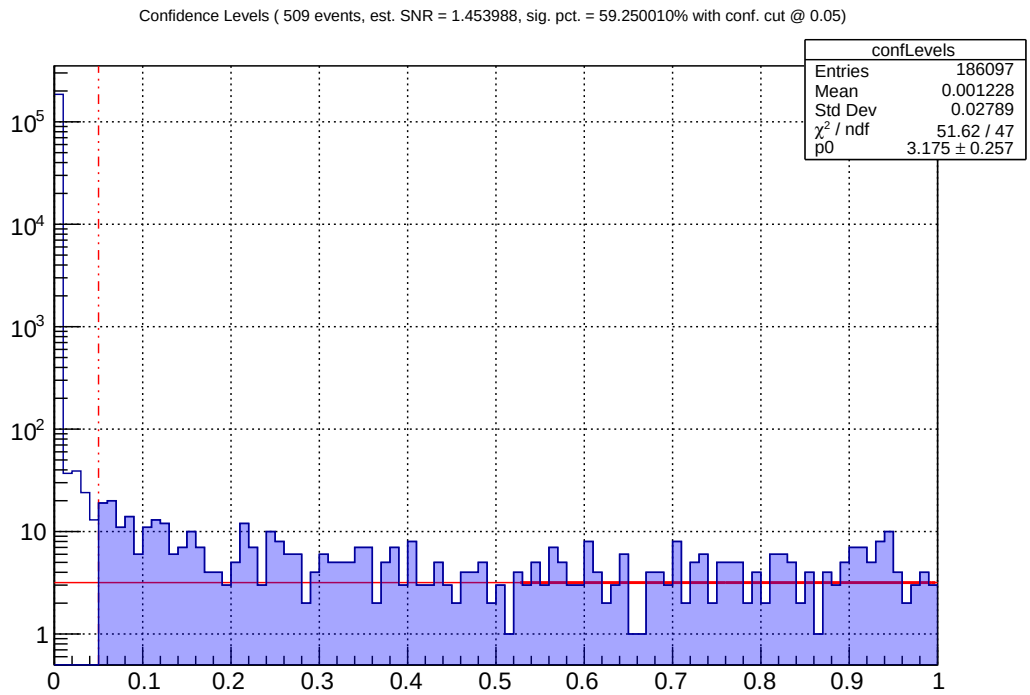

Fig. 11.1: CL for $5C$ kin. fit

11.2.2 Pull Distributions

The resulting pull distributions, **Fig. 11.2**, also look reasonable.

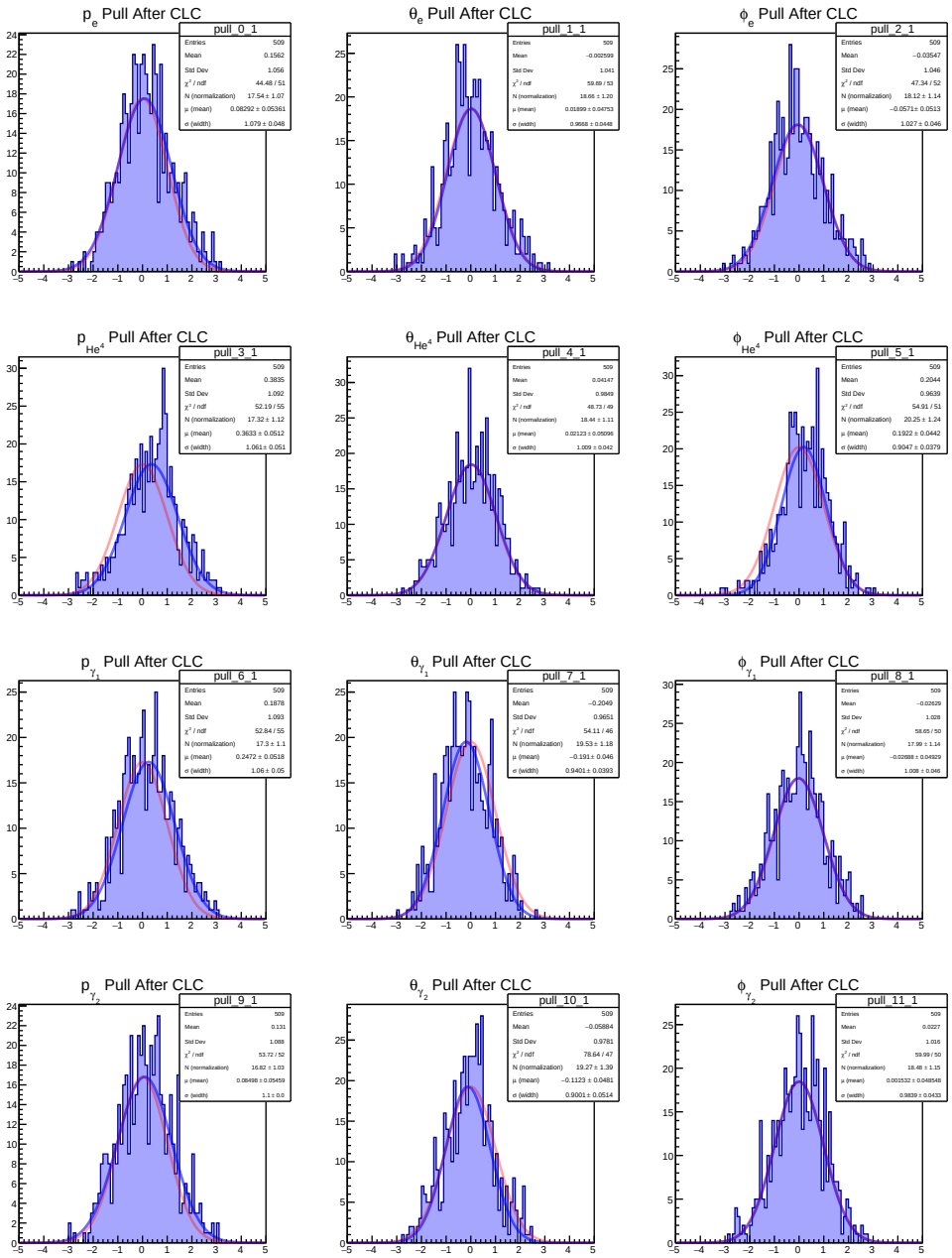

Fig. 11.2: Pull distributions for p, θ, ϕ (left to right) for $e, {}^4\text{He}, \gamma_1, \gamma_2$ (top to bottom). The blue and red curve are a fit to the distribution and what it should be, respectively.

11.3 Fit Results

Like the previous studies, the CLC and pull distributions show a reasonable fit. We now focus on what the events passing the CLC looks like.

11.3.1 Exclusivity Variable Distributions

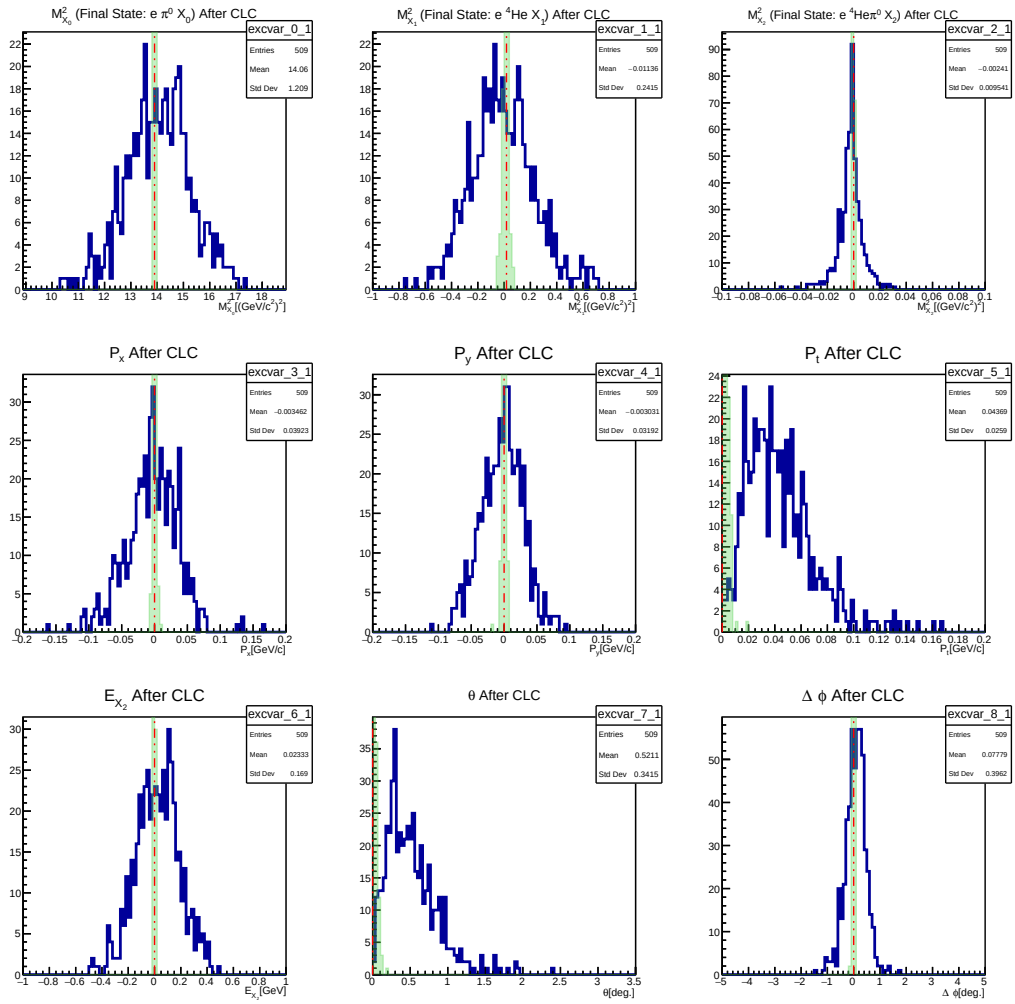

Fig. 11.3: Exclusivity variable distributions, and the expected value (red vertical dashed line) for:
- Measured events passing exclusivity cuts (black)
- Measured events passing kinematic fit with 0.05 CLC (blue)
- Fitted events passing kinematic fit with 0.05 CLC (highlighted green)

11.3.2 Invariant Mass Distribution

The invariant mass distribution photon pairs selected from the CLC is shown in **Fig. 11.4** are within the previous study's cut but are not applied. Note that the fitted distribution (green) is more like a δ-function distribution with this additional constraint.

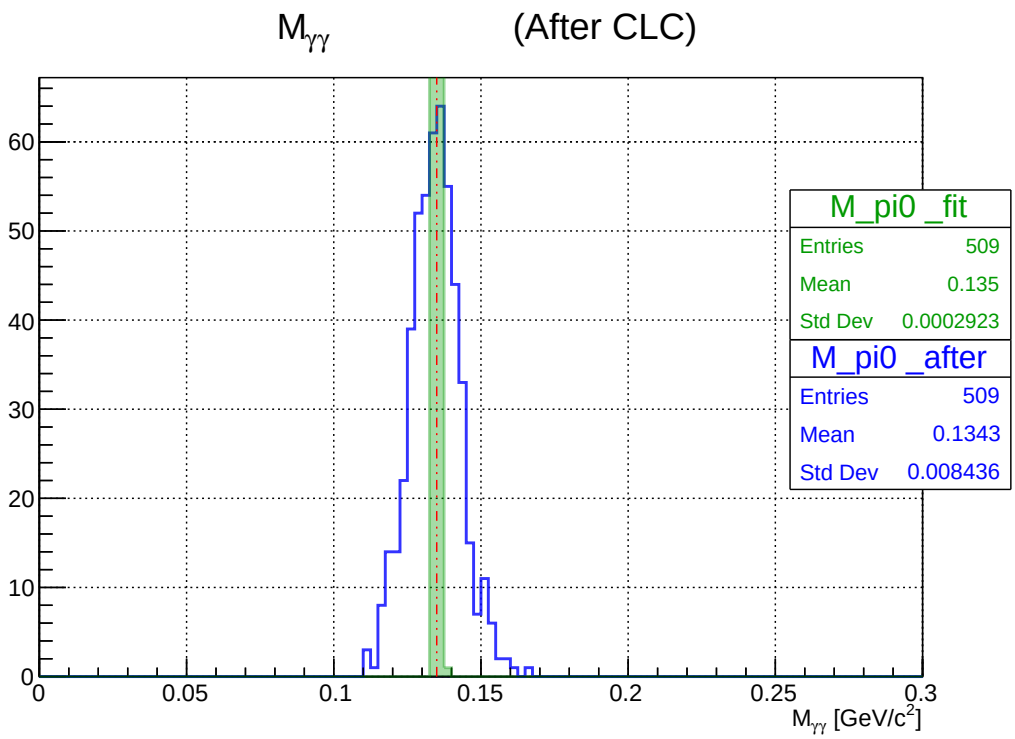

Fig. 11.4: Photon pair invariant mass

The invariant mass distribution of the photon pair along with the exclusivity variable distributions of all the measured particles give a great degree of confidence in the selected events belonging to the exclusive coherent π^0 production process: $e\ ^4\text{He} \rightarrow e\ ^4\text{He}\ \pi^0$. With these selected events, the beam spin asymmetry for this process can be extracted.

Chapter 12

$5C$ Kinematic Fit Results

Unfortunately, the statistics are very limited making an extraction of all three parameters of **Eq. 2.12** unfeasible. Instead, the variation in ϕ of the beam spin asymmety is parameterized as sinusoidal since

$$A_{LU} \sim \alpha \sin \phi \quad . \tag{12.1}$$

To see this variation, binning of at least ϕ is required for the kinematic variables.

12.1 Kinematic Coverage and Binning Data

Since the events selected are very limited, it only makes sense to have one combined kinematic bin in Q^2, x, and t. From there, we can extract the variation in ϕ of the beam spin asymmetry by binning ϕ into a few bins.

From **Fig. 12.1**, we can see that there is no binning in Q^2, x, or t, but ϕ is partitioned into 8 bins to extract the beam spin asymmetry (as demarcated by color).

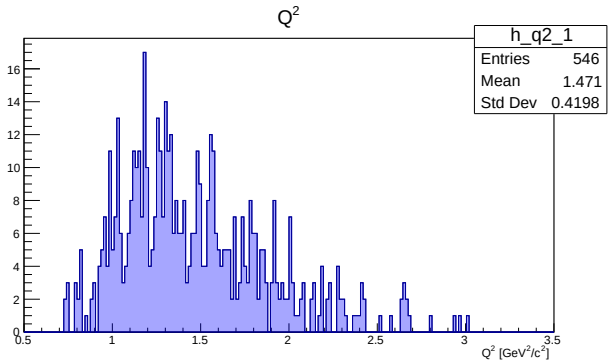

(a) Q^2 binning

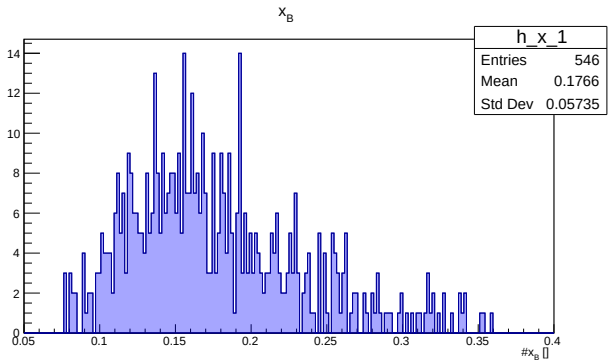

(b) x binning

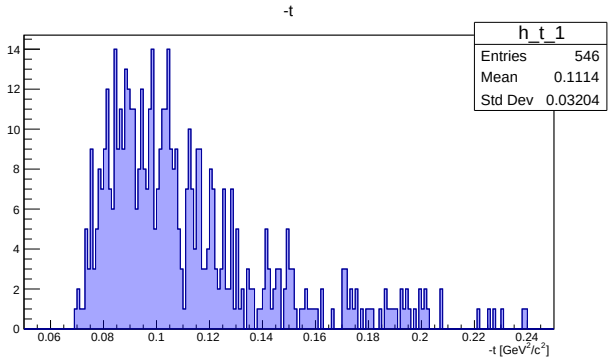

(c) t binning

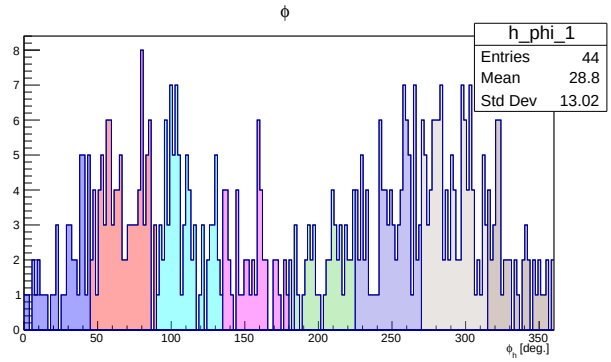

(d) ϕ binning

Fig. 12.1: Kinematic binning

12.2 Beam Spin Asymmetry

Experimentally, the BSA is extracted as

$$A_{LU} = \frac{1}{P_B}\frac{N_- - N_+}{N_- + N_+} \quad ,$$

where the $N_\pm$ is the counts of ± 1 helicity events, respectively. The statistical errors bars follows from:

$$\begin{aligned}\delta A_{LU} &= \frac{2}{P_B}\frac{\sqrt{N_-^2\left(\delta N_+\right)^2 + N_+^2\left(\delta N_-\right)^2}}{\left(N_- + N_+\right)^2} \\ &= \frac{2}{P_B}\frac{\sqrt{N_-^2 N_+ + N_+^2 N_-}}{\left(N_- + N_+\right)^2}\end{aligned} \quad .$$

As shown in **Fig. 12.2a**, the result is consistent with no asymmetry. Now this is contradictory to the BSA extracted from events selected via exclusivity cuts, as seen in **Fig. 12.2b**. This large discrepancy needs to be investigated in order to explore where the differences lie in the events selected in each of the two methods. In the following chapter, the events selected are separated into different datasets to find out if there is any clear distinction that directly leads to why the two asymmetries do not agree.

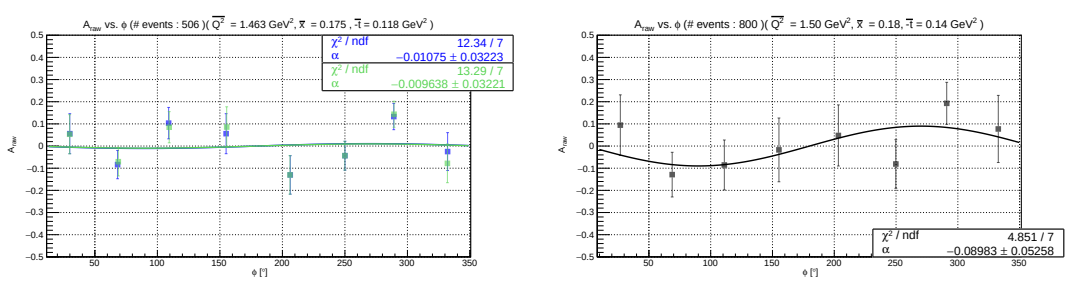

(a) Events selected from $5C$ kin. fit with 5% CLC

(b) Events selected with exclusivity cuts

Fig. 12.2: Beam spin asymmetry variation in ϕ, integrated over all $Q^2, x, -t$ for the events selected by different methods

Chapter 13

Resolving Discrepancies

Event selected through a set of exclusivity cuts yields a very different BSA (**Fig. 12.2b**) from that of events selected through kinematic fitting with a 5% CLC (**Fig. 12.2a**). To resolve the discrepancy, we have to look at various subsets to pin down what is fundamentally different about the two results.

13.1 Breaking Down the Datasets

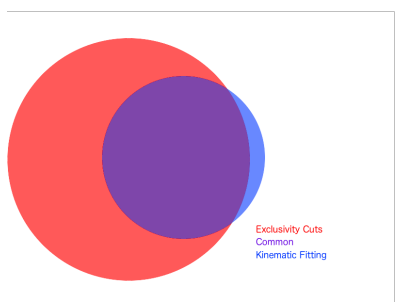

Fig. 13.1: Venn diagram of events passing exclusivity cuts (red) and kin. fitting with 5% CLC (blue)

First, we form the union between all events passing exclusivity cuts and all events passing the 5% CLC (see **Fig. 13.1**). Then we can break it down to look at particular subsets. For a quick reference, we introduce Venn diagrams for the different subsets (see **Fig. 13.2**).

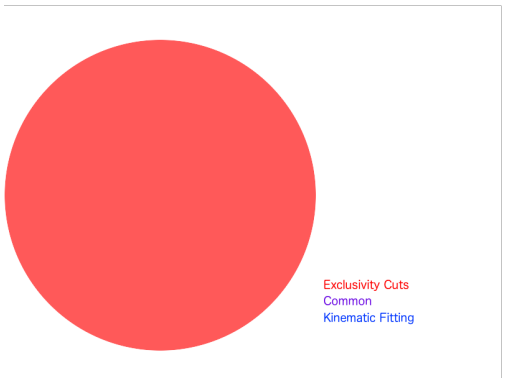

(a) Events passing exclusivity cuts

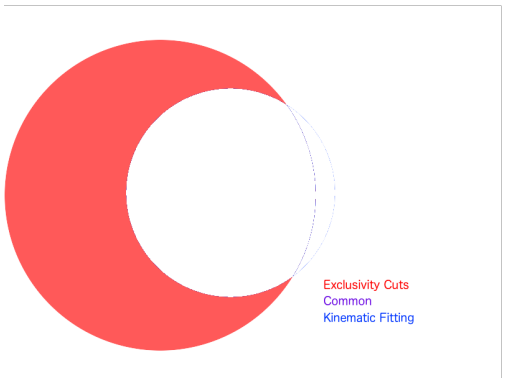

(b) Events passing only exclusivity cuts

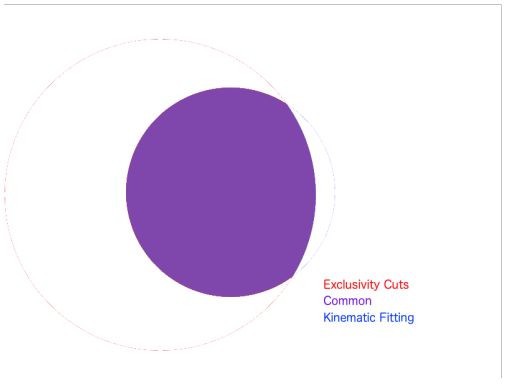

(c) Common events

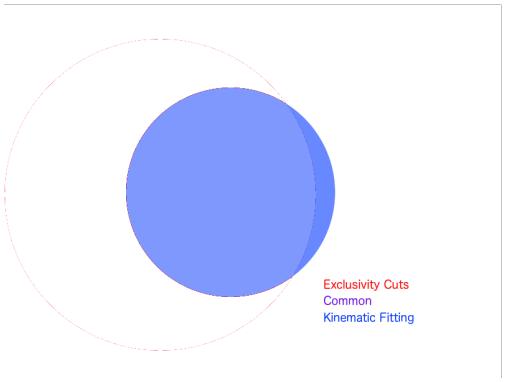

(d) Events passing kinematic fitting

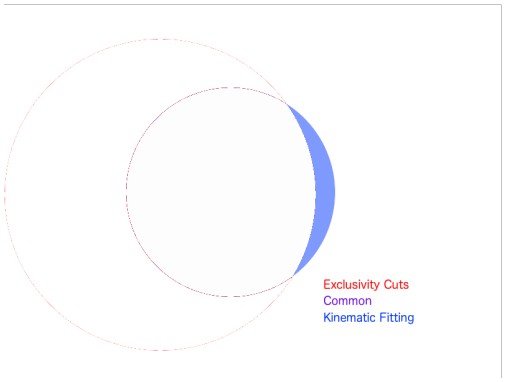

(e) Events passing only kinematic fitting

Fig. 13.2: Legend for proper subsets of the union of events passing exclusivity cuts and events passing $5C$ kinematic fit with 5% confidence level cut

13.2 Beam Spin Asymmetries

The first thing to look at to resolve the discrepancies is the magnitude of each asymmetry, $A_{LU}^{90^\circ}$, to see if anything sticks out with this partitioning. Again, starting with the two results: all events passing exclusivity cuts (**Fig. 13.3**) from the previous study [5] and all events passing kinematic fitting (**Fig. 13.4**) from this study.

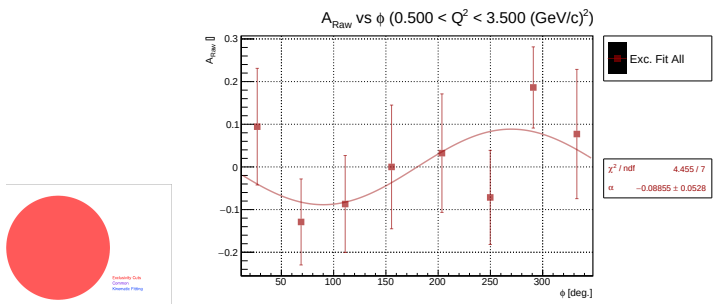

(a) 800 events **(b)** $A_{LU}^{90^\circ} = -8.9 \pm 5.3\%$

Fig. 13.3: Beam spin asymmetry (b) of selected events (a): All events passing exclusivity cuts

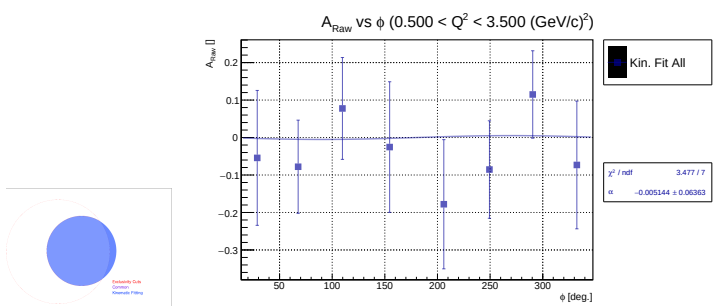

(a) 506 events **(b)** $A_{LU}^{90^\circ} = -1.1 \pm 3.2\%$

Fig. 13.4: Beam spin asymmetry (b) of selected events (a): All events passing kinematic fitting

To see if the discrepancy is beyond a difference in statistics, we look to the common events between the two methods produces an asymmetry (**Fig. 13.5**). What we see is that the set of common events brings the previous study's asymmetry substantially down

(in magnitude) and brings the asymmetry from kinematic fitting up (in magnitude). That is, the common events' central value asymmetry ($-3.3 \pm 6.8\%$) has moved well outside the range of the previous study's asymmetry ($-8.9 \pm 5.3\%$). In comparison, the common events' central value asymmetry is within the kinematic fitting's asymmetry range ($-0.5 \pm 6.4\%$).

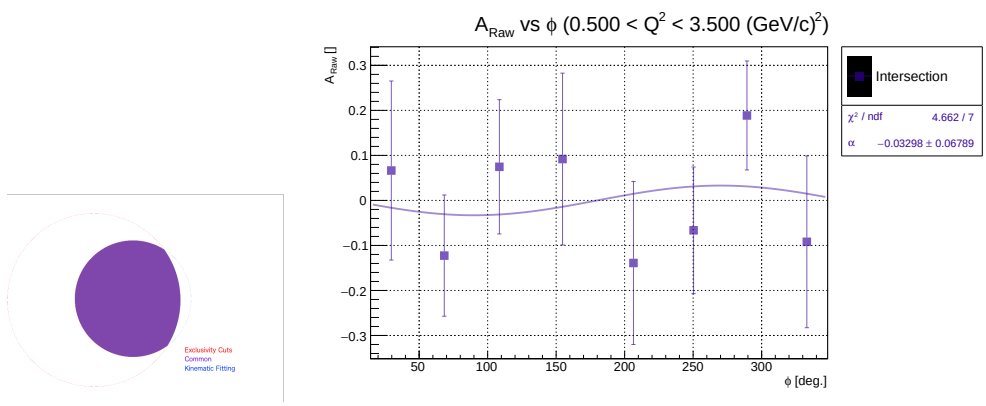

(a) 488 events

(b) $A_{LU}^{90^\circ} = -3.3 \pm 6.8\%$

Fig. 13.5: Beam spin asymmetry (b) of selected events (a): Events passing both exclusivity cuts and kinematic fitting

Although the common events do not reveal anything conclusive, the exercise of partitioning the dataset shows its benefit when looking into events passing only exclusivity cuts.

When taking events that only pass the exclusivity cuts, we see in **Fig. 13.6** that the asymmetry of these events are $-20.3 \pm 8.5\%$. This strong asymmetry is coming from over a third of the previous study's events. To understand why it is these events that have such a high asymmetry, we look at the different distributions they produce.

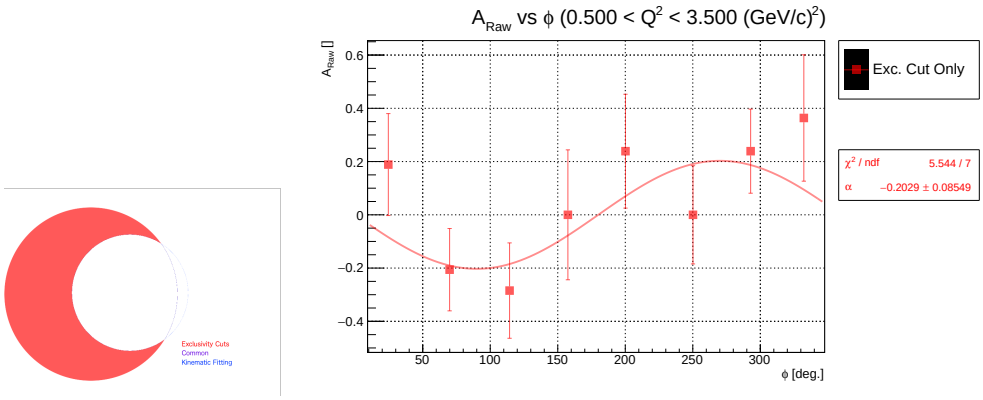

(a) 312 events

(b) $A_{LU}^{90^\circ} = -20.3 \pm 8.5\%$

Fig. 13.6: Beam spin asymmetry (b) of selected events (a): Events passing only exclusivity cuts

13.3 Invariant Mass Distributions

The invariant mass distribution of the photon pair should show if anything stands out. Looking at the invariant mass distribution of the disjointed sets in **Fig. 13.7**, there is nothing of note between the three distributions except maybe for the fact that the red distribution is wider.

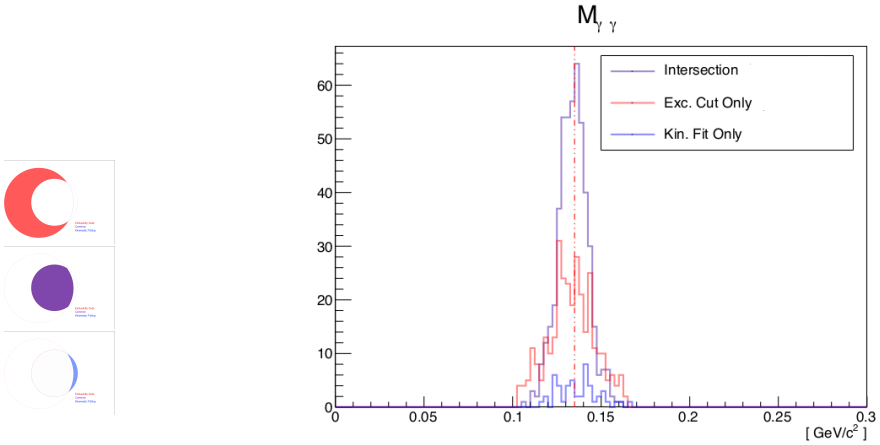

(a) Reference sets

(b) Invariant mass distributions

Fig. 13.7: Inv. mass distributions for events passing: exclusivity cuts only, kin. fitting only, and both

13.4 Exclusivity Variable Distributions

The exclusivity distributions show the interplay between the measured particles. These distributions should show whether the set of particles are part of the same event. We see from **Fig. 13.8** that the blue distributions just looks like more of the same of the purple distributions. However, the red distributions are much wider, having longer tails.

In particular, the events passing only the exclusivity cuts (red), have:

- Distributions are centered farther out from their expected value of zero for:
  - the missing transverse momentum (pt_{X_2}),
  - the angle between the measured and missing π^0 (θ_{X_1,π^0})
- The coplanarity ($\Delta\phi$) is uniformly distributed with no clear peak
- The distributions have many events in the tail for:
  - The missing mass-squared ($M^2_{X_0}$) of the process $e^4\text{He} \rightarrow e'\pi^0 X_0$
  - The missing energy (E_{X_2}) of the process $e^4\text{He} \rightarrow e'^4\text{He}'\pi^0 X_2$

It is clear why these events fail the kinematic fitting: the events in the tails do not conserve momentum and energy within the detectors' errors. What is not obvious is why these events have such a higher magnitude in its asymmetry.

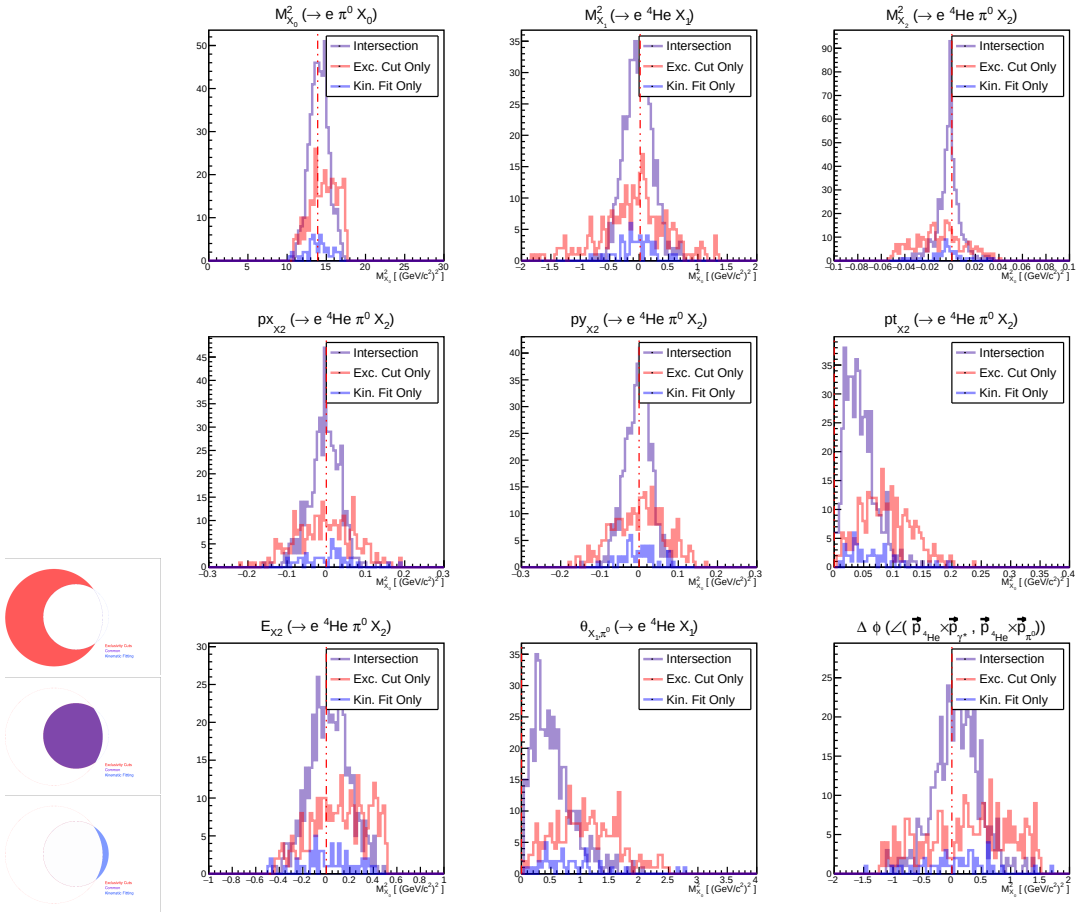

(a) Reference

(b) Invariant mass distributions

Fig. 13.8: Exclusivity variable distributions of the disjoint sets:

- passing exclusivity cuts only (red)

- common events (purple)

- kinematic fitting only (blue)

13.5 Summary

If we focus on just the previous dataset, obtained from exclusivity cuts, we can reframe the results. The kinematic fitting has the surprising effect of partitioning the previous study's 800 coherent π^0 events into 312 events with a strong asymmetry ($-20.3 \pm 8.5\%$) and 488 events with little to no asymmetry ($-3.3 \pm 6.8\%$), as can be seen in **Fig. 13.9**. The difference between the events is just whether or not they pass kinematic fitting.

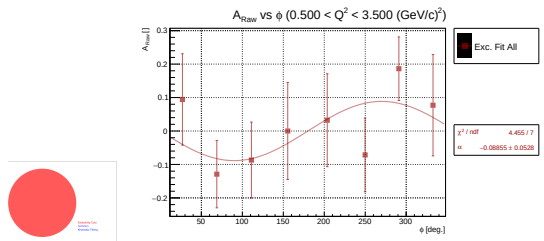

(a) $A_{LU}^{90^\circ} = -8.9 \pm 5.3\%$

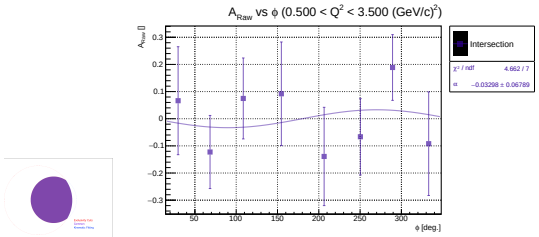

(b) $A_{LU}^{90^\circ} = -3.3 \pm 6.8\%$

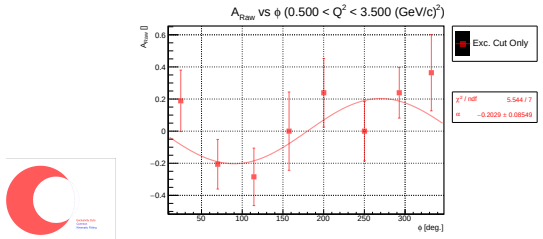

(c) $A_{LU}^{90^\circ} = -20.3 \pm 8.5\%$

Fig. 13.9: Beam spin asymmetries of (a) events passing exclusivity cuts but

(b) Passing kinematic fitting

(c) Failing kinematic fitting

Admittedly, it is unclear where exactly this large background asymmetry is coming from. It is, however, clear that events passing both exclusivity cuts and kinematic fitting is diluting this large asymmetry and producing the asymmetry from the previous study. Moving forward, the events selected from the $5C$ kinematic fit will be discussed.

Chapter 14

Systematic Uncertainties

Now that the differences are resolved, showing that the large asymmetry coming from events passing exclusivity varible cuts are coming from background events, we can look into the systematic uncertainties of the BSA measurement of the kinematic fit selected events. To reiterate, event selection through kinematic fitting is advantageous in that it only requires one cut (confidence level cut) to select events. So a systematic study of the confidence level cut will be done. Additionally, the beam polarization plays a direct role in measuring the asymmetry so any uncertainty in it can considerably affect the result. The systematics will be calculated to see its contribution. Finally, since the statistics are limited and the ϕ distribution is not uniform, the binning choice in ϕ can affect the final BSA measurement.

Although being overwhelmed by statistical uncertainties, it is worthwhile to consider and explore these key systematic uncertainties as well, to really pin down a limit on the result. In the following sections, these aforementioned systematics will be studied to see the effect and contribution of each on the overall BSA measurement.

14.1 Beam Polarization

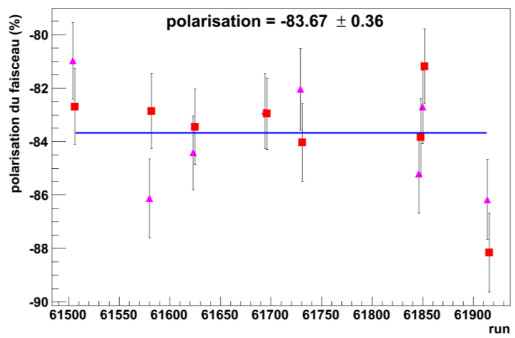

Fig. 14.1: Beam polarization variation over the CLAS EG6 run: The red (magenta) are runs with negative (positive) current runs through the Møller polarimeter's Helmholtz coils [4].

Since the BSA is rescaled by the polarization:

$$A_{LU} = \frac{1}{P_B} \frac{N_- - N_+}{N_- + N_+} \quad ,$$

the magnitude of the asymmetry is very sensitive to the uncertainty of the polarization. From polarization studies, the percent uncertainty, $\delta P_B / P_B$, is 3.5%. This directly propagates to a percent uncertainty in the asymmetry:

$$\begin{aligned} \delta A = \left| \frac{\partial A}{\partial P_B} \right| \delta P_B &= \left| \left(-\frac{1}{P_B^2} \right) \left(\frac{N^+ - N^-}{N^+ + N^-} \right) \right| \delta P_B \\ &= \left(\frac{1}{P_B} \right) \; A \; \delta P_B \end{aligned}$$

$$\Rightarrow \frac{\delta A}{A} = \frac{\delta P_B}{P_B} = 3.5\% \quad .$$

An estimate of the systematic certainty of the measured BSA that is attributed to the beam polarization is taken to be 3.5%.

14.2 Confidence Level Cut

The confidence level is the only user-based cut that selects events. The choice of the cut is made to maximize statistics while trying to minimize background introduced. It is important to see how the cut affects the measurement of the BSA. Below shows several extracted BSA for different confidence level cuts. The systematic contribution from this cut is estimated to an absolute value of 2.26%.

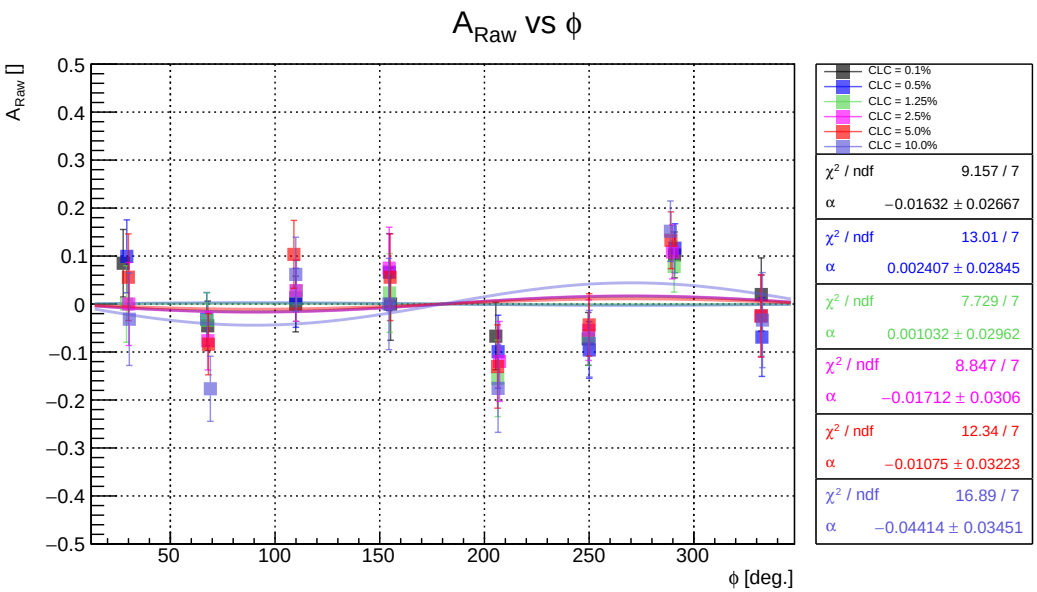

Fig. 14.2: Beam spin asymmetry variation with different confidence level cut values. The red are the nominal data points of this study.

To look more closely into its effect, the BSA is measured at different CLCs. In **Fig. 14.3**, the BSA hovers between -1% to 0% with wide error bars for a considerable range of high CLC and then migrates to 0% as the CLC decreases, expectedly. That is, at lower and lower CLC's, any discernible BSA signal becomes increasingly diluted and swamped by all random, background events.

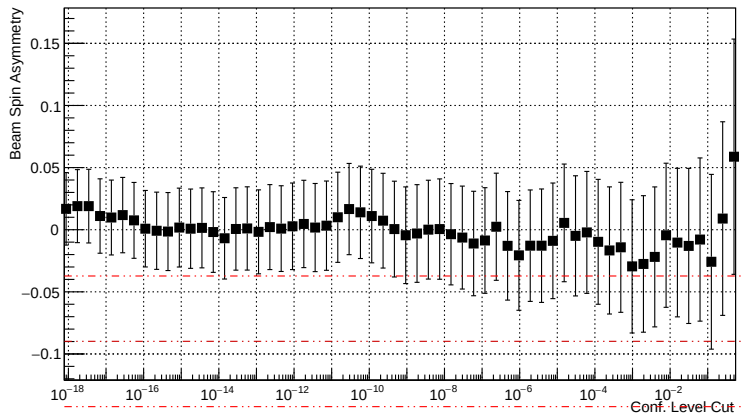

Fig. 14.3: Beam spin asymmetry as a function of confidence level cut

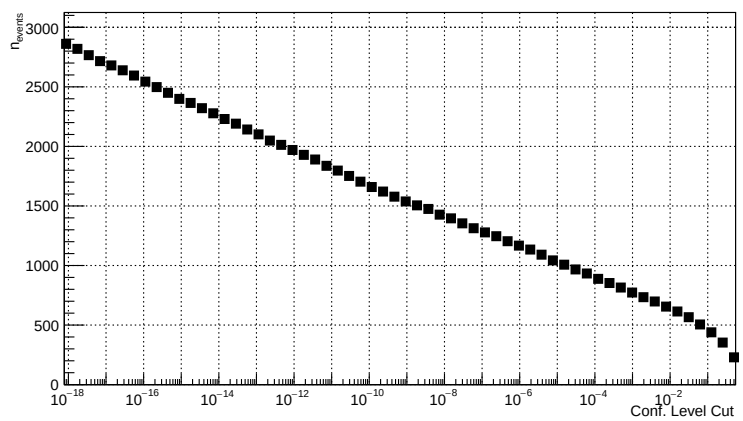

Fig. 14.4: Number of events passing CLC as a function of confidence level cut value

This can explicitly be seen in **Fig. 14.4** around a CLC of 1%, near this study's choice of CLC. Here, a change of behavior in the number of events passing the CLC is apparent. At low confidence levels, the number of events is exponential (the $CLC-$axis is logarthmic), dominated by background. At higher confidence levels, the behavior changes as the number of events grows linearly with decreasing CLC, signifying the confidence level distribution is uniform in this range.

Again, the confidence level distribution characteristics in **Section ??**, a uniform distribution in the confidence level shows that these events do indeed satisfy the hypothesis of coherent π^0 production, via conservation of momentum and energy within the detector resolutions.

14.3 Binning in ϕ

Due to the limited statistics, the choice of binning in ϕ can significantly contribute to the uncertainty. Choosing the right number of bins involves striking a balance between maximizing the number of bins to show the variation in the asymmetry and limiting number of bins to minimize the statistical error bars.

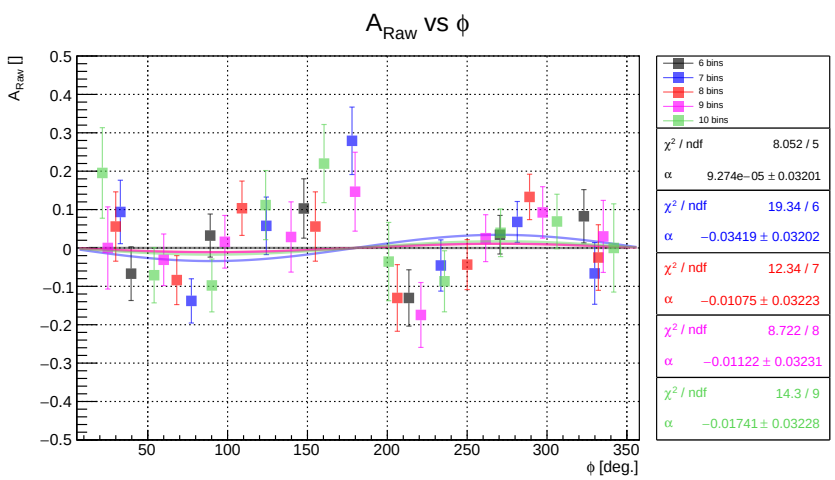

Fig. 14.5: Beam spin asymmetry variation in different number of equally spaced ϕ bins. The red are the nominal data points of this study.

Out of the different binnings, the most reasonable χ^2/ndf other than the 8 bins used for this analysis is 9 equally spaced bins. The systematic uncertainty coming from this binning scheme is estimated to be about 1.70%.

14.4 Summary of Systematic Uncertainties

Table 14.1 summarizes the systematic uncertainties. The largest contributions comes from the CLC and ϕ binning. Although this is a systematics study, the underlying uncertainty comes from statistics:

- The choice of CLC is to maximize statistics while minimizing background.
  - With better statistics, a confidence level cut can be made much higher where very little background is creeping in. The nominal value chosen sits right on a steep slope of the background. Any cut higher limits the statistics dramatically and any lower increases the background noticeably.
- The binning in ϕ is chosen to show if the BSA is of the form $\alpha \sin \phi$, while maintaining an appreciable amount of statistics in each bin. Of course, better statistics would make the choice of binning in ϕ irrelevant, while improving χ^2/ndf.

Because of this, it is not possible to decouple the statistical limitations from the systematic uncertainties. Therefore, instead of reporting the statistical and systematic uncertainties as two independent disparate quantities, maybe a single estimate should be used to characterize the overall uncertainty.

Systematic Uncertainty Source	**Contribution**	
	$\boldsymbol{\Delta A_{LU}/A_{LU}}$	$\boldsymbol{\Delta A_{LU}}$
Beam polarization	3.50%	0.04%
Conf. level cut	–	2.26%
ϕ binning	–	1.70%
Total	–	2.83%

Table 14.1: Systematic Uncertainties

Chapter 15

Final Result and Discussion

15.1 Result

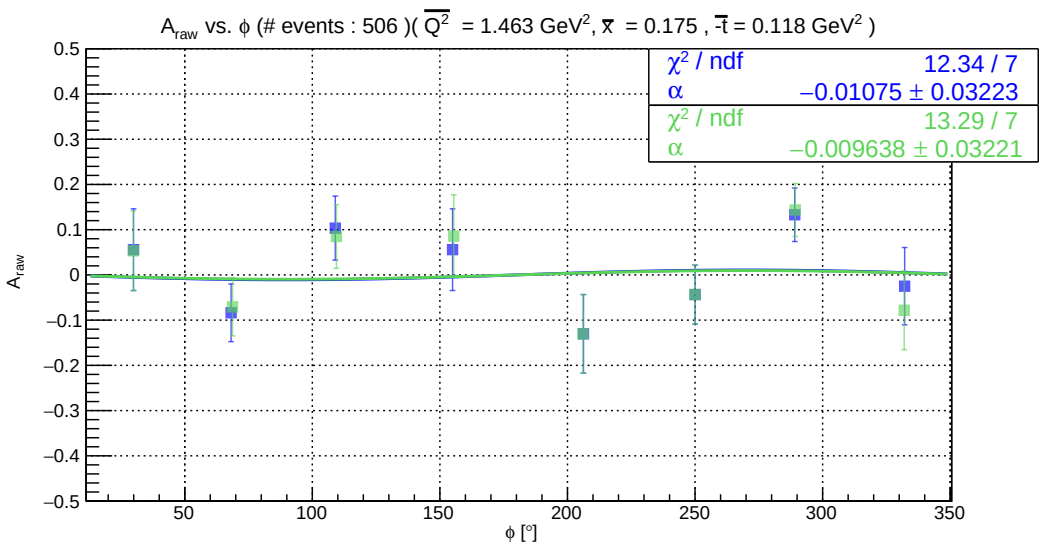

Fig. 15.1: Events selected from $5C$ kin. fit with 5% CLC

Experimentally, the magnitude of the BSA of coherent π^0 production off ^{4}He, for

$$\bar{Q}^2 = 1.463\,(\mathrm{GeV}/c)^2\,, \quad \bar{x} = 0.175, \quad \bar{t} = -0.118\,(\mathrm{GeV}/c)^2 \tag{15.1}$$

is extracted as $A_{LU}^{90^\circ} = -1.08 \pm 3.22\,(\mathrm{stat.}) \pm 2.83\,(\mathrm{sys.})\,\%$ when fitting the variation of the form $A_{LU}(\phi) = A_{LU}^{90^\circ} \sin\phi$.

The result is statiscally limited, and furthermore, the systematics are driven by these same statistical limitations. With that said, and including the contribution from the systematic uncertainty of beam polarization,

$$A_{LU}^{90^\circ} = -1.08 \pm 3.22\% \quad .$$

We can exclude, with 95% confidence, $A_{LU}^{90^\circ}$ greater than 5.36% or less than -7.52%. However, we can see from **Fig. 15.1** that the asymmetry is consistent with zero.

15.2 Discussion

A nonzero asymmetry can arise from effects beyond the single-photon exchange approximation, the virtual photon interacting with any non spin-0 constituent of the ^{4}He nucleus, or a myriad of other possible scenarios. However it is unnecessary to speculate since the measured BSA points to these effects being neglible. By inspection of the data points in **Fig. 15.1**, there is no evidence of any sizable asymmetry; there are an equal number of points scattered closely above and below the ϕ-axis. Furthermore, the quality of the sinusoidal fit, quantified by the reduced χ^2, is poor ($\chi^2/\text{ndf} = 1.76$).

Recall that the choice of the sinusoidal fit was to show that any ϕ-dependent asymmetry would arise and manifest itself in the form of a sinusoidal relationship in a model independent way (originally shown in **Chapter 1**):

$$A_{LU} = \frac{\alpha \sin\phi}{1 + \beta\cos\phi + \gamma\cos 2\phi} \tag{15.2}$$

where the parameters are

$$\begin{aligned} \alpha &:= \left[\frac{\sigma_{L'T}}{\sigma_T + \epsilon_L \sigma_L}\right] \sqrt{2\epsilon_L\left(\epsilon - 1\right)} \\ \beta &:= \left[\frac{\sigma_{LT}}{\sigma_T + \epsilon_L \sigma_L}\right] \sqrt{2\epsilon_L\left(\epsilon + 1\right)} \qquad . \\ \gamma &:= \left[\frac{\sigma_{TT}}{\sigma_T + \epsilon_L \sigma_L}\right] \epsilon \end{aligned} \tag{15.3}$$

It is possible that the asymmetry can be supressed by the β and γ terms in of **Eq. 15.2** which points to, from **Eq. 15.3**, sizable contributions coming from either or both the structure functions σ_{LT} and σ_{TT}. This however would require the contributions to these structure functions to significantly overcome the contributions from the combination $\sigma_T + \epsilon_L \sigma_L$ and the polarization of the virtual photon ϵ along with its longitudinal component ϵ_L. To pin this down, more statistics are required and an extraction of the cross sections is needed to constrain these contributions.

What is maybe more likely is that there a supression of the asymmetry simply due to the symmetries of the electroproduction process of the pseudoscalar π^0 off the scalar ^{4}He target at play. C. R. Ji independently shows, in a general formulation, that under the assumption of single-photon exchange, that this must be the case [2].

Chapter 16

Conclusion and Outlook

16.1 Summary of Results

Particle candidate selection is based on well-established and published particle identifcation procedures of [6, 5] for finding the scattered electron, the recoiling ^{4}He, and the produced photons.

Event selection, using the kinematic fitting technique as formulated and outlined in this thesis, [65], and [66], works well based on a myriad of observations.

From fit quality, the distributions are expected:

- Confidence level distribution: Sharp peak at zero and a plateau thereafter
- Pull distributions: All pull measurements look standard normally distrbuted

From fit results:

- Exclusivity variable distributions: All distributions look very similar to ones passing all exclusivity cuts [6, 5] but with suppressed tails
- Invariant mass distribution: The photon pair invariant mass distribution for the π^0 selection has a clear, clean peak around the nominal π^0 mass

- Beam spin asymmetries: The raw $A_{LU}(\phi)$ of the published coherent DVCS off ^{4}He [6], which used exclusivity variable cuts for event selection, was verified independently using $4C$ kinematic fit; all data points are consistently well within error bars of the previous results (**Fig. 9.4**), with most χ^2/ndf of the asymmetry fit improved

The higher statistics DVCS events showed that the BSA for events selected with kinematic fit is consistent to that of the events selected with exclusivity cuts, validating the procedure. The power of this method is shown when dealing with the lower statistics DVπ^0P events. The $4C$ fit selects events where the photon pair showed a clear peak at π^0 without any information given about the π^0 mass. The $5C$ fit cleans this distribution up and shows the invariant mass distribution with a width inherent to the detector uncertainties. The utility and need for this method in this analysis was exhibited with the lower statistics, wherein the fit is able to throw away background events that no obvious set of traditional exclusivity cuts can eliminate. The kinematic fit is able to separate a high asymmetry background from an asymmetry consistent with zero for DVπ^0P.

Due to statistics, there is only binning in one kinematic variable: ϕ. From this the BSA of coherent π^0 production off ^{4}He, for

$$\bar{Q^2} = 1.463\,(\mathrm{GeV}/c)^2\,, \quad \bar{x} = 0.175, \quad \bar{t} = -0.118\,(\mathrm{GeV}/c)^2 \tag{16.1}$$

is measured to be

$$A_{LU}^{90^\circ} = -1.08 \pm 3.22\% \quad ,$$

where the uncertainty is dominated by statistics.

The result, especially just by inspection of **Fig. 15.1**, is in agreement with a BSA supression due to the symmetries at play of the pseudoscalar π^0 electroproduction off the scalar ^{4}He target shown in [2]. This measurement puts strong constraints on contributions from higher order processes, and makes it clear that DVMP can be safely interpreted in the given kinematics, paving the way to look into the much more complicated incoherent channel among other DVMP processes and reactions.

16.2 Outlook

The results of this thesis is in agreement with and provides a benchmark measurement for a recent theoretical formulation [2]. Moreover, it shows the feasibility of approximations and assumptions made in the formulism, opening the door to explore

- other electroproduction reactions off ^{4}He in the coherent channel
  - DVMP of the η to cross-check the BSA with another pseudoscalar electroproduction off the scalar target
  - DVMP of scalar mesons where a BSA measurement can help get at two form factors that play a role in the hadronic current [2]
- the more complicated DVMP off ^{4}He in the incoherent channel, where the symmetries certainly no longer hold, to extract the BSA of
  - DVMP of the π^0 to compare to that of the free proton [11]
  - DVMP of the η to compare to that of the free proton [12]

in an effort to understand the medium modifications of the GPDs in a nuclear environment, to get at the so-called EMC effect in the same manner as [7]

- and revisit all of these with the CLAS12 era experiments, where
  - greater statistics are achievable given the possible luminosity
  - an approximation of the covariance matrix is unnecessary, as the full covariance matrix is available and includes other variables relating to the vertex

to support, validate, or offer new insights into this measurement.

The incoherent channel offers a few challenges, most significantly accounting for the Fermi motion of the nucleon in the nucleus. In order to keep kinematic fitting applicable, an extension would be required to incorporate the uncertainty from this initial condition. Additionally, although the incoherent channel is an exclusive process, where every particle involved is detected, the spectator is unaccounted for. This would would require tweaking the energy and momentum conservation constraints or making some assumptions.

Alternatively, there is active development of A Low Energy Recoil Tracker (ALERT) detector for CLAS12 which aims to measure all fragments/spectators of an incoherent process with improved particle discrimination, tracking efficiency, and variable trigger [67]. These advantages make it possible to even measure the Fermi momentum.

Even further down the line, the proposed Electron Ion Collider (EIC) planned to accelerate both the electron and ions (including ^{4}He) also aims to detect all reaction products and variably reach center of mass energies and luminosities up to 140 GeV and 10^{34} cm^{-2}s^{-1}, respectively [68].

These future endeavors and accompanying statistics, along with the previously mentioned DVMP reactions make for a bright future, especially the DVMP program to provide flavor decomposition of GPDs and the nuclear program to understand nuclear medium modifications and the EMC effect.

Appendices

A Mott Differential Cross Section Relationship

The Rosenbluth differential cross-section is a modification of the Mott differential cross-section $\left(\frac{d\sigma}{d\Omega}\right)_{\text{Mott}}$, which is the relativistic quantum mechanical generalization of the Rutherford elastic scattering differential cross-section between two point-like spin-1/2 particles, defined by

$$\left(\frac{d\sigma}{d\Omega}\right)_{\text{Mott}} = \left(\frac{\alpha^2}{4E^2 \sin^4 \frac{\theta}{2}}\right) \cos^2 \frac{\theta}{2} \tag{A.1}$$

$$= \left(\frac{d\sigma}{d\Omega}\right)_{\text{Rutherford+}} \cos^2 \frac{\theta}{2} \tag{A.2}$$

where α is the fine-structure or electromagnetic coupling constant.

The Rosenbluth differential cross-section is a modification of the Mott differential cross-section $\left(\frac{d\sigma}{d\Omega}\right)_{\text{Mott}}$, which is the elastic scattering differential cross-section between two point-like spin-1/2 particles (see **Appendix A** for more). The modification factors, which account for the recoiled nucleon target or its finite mass, as well as nontrivial charge and magnetic moment distributions, are described by

- the ratio (E'/E) is the fractional energy loss of the scattered electron relative to the incoming electron, imparted onto the recoiled nucleon,

- the term in the square bracket parametrized by the dimensionless Lorentz invariant $\tau := \frac{Q^2}{4M^2}$ (see **Section 1.2**)
- the electric G_E and magnetic G_M form factors depending on Q^2 and
- the $\tan^2 \frac{\theta}{2}$ term accounts for the spin-spin interaction, the magnetic component of the interaction.

Since the electric and magnetic form factors are functions of Q^2 and *not* $\vec{\boldsymbol{q}}$, the usual direct interpretation of the form factor as Fourier transforms of charge or magnetic moment distributions is washed away.

B Corrections and Calibrations

B.1 Electron Vertex Correction

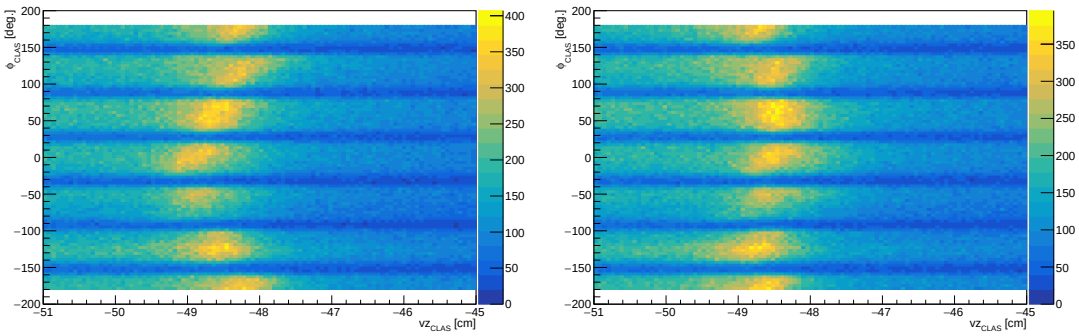

(a) Before correction **(b)** After correction

Fig. B.1.1 : Vertex Correction: An azimuthal angle dependent vertex shift is implemnted to account for changes in beam position.

Reconstruction assumes the beam to be fixed at the origin CLAS, when projecting CLAS along the beam axis. However, changes in the experiment reveal the position moves. To account for beam movement over the course of the experimental run, a correction to the vertex is developed by N. Baltzell [69]. The correction has the form:

```
vz_corr = vz[ipart] - r/tan(theta) cos( phi - phi_0 )
```

where the parameters `r` and `phi_0` are given in **Table B.1** and `theta` and `phi` are the polar and azimuthal angle measured in CLAS given by the direction unit-vector $\hat{\boldsymbol{p}}$ in **Eq. B.1.1**.

$$\hat{\boldsymbol{p}} = \begin{bmatrix} \texttt{cx[ipart]} \\ \texttt{cy[ipart]} \\ \texttt{cz[ipart]} \end{bmatrix} \tag{B.1.1}$$

Variable	Value	Units
r	0.24	cm
phi_0	-186.6	deg.

Table B.1: Vertex Correction Parameters

B.2 RTPC Corrections

B.2.1 θ_{RTPC} Correction

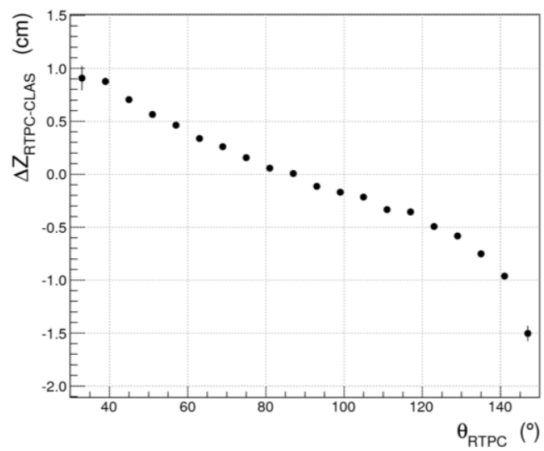

Fig. B.2.1.1 : RTPC Vertex Correction: Δz vs θ showing a linear dependence[70].

When checking the vertex measured by CLAS and the RTPC, there was a strong linear dependence in the reconstructed RTPC θ vertex. First a correction to the polar angle, developed by N. Baltzell [70], is applied:

$$\theta_{\mathrm{RTPC}} = \frac{\Delta z}{\mathtt{r}} \sin(2\theta) \tag{B.2.1.1}$$

from **Fig. B.2.1.1** , we see that Δz, in cm, is linear in θ:

$$\Delta z = \mathtt{m}\theta_{\mathrm{deg}} + \mathtt{b} \tag{B.2.1.2}$$

where the parameters of the slope `m` and intercept `b` are given by

```
m = -0.017

b = 1.53
```

θ and θ_{deg} are the uncorrected the RTPC polar angle ($\theta_\circ$ is in degrees) and the parameter `r =` 4.5 cm is the radial position half way through the drift region.

B.2.2 vz_{RTPC} Correction

Now that the polar angle is corrected, the vertex can be shifted into place:

$$vz_{\mathrm{RTPC}} = z_{\mathrm{cm}} - \Delta z \tag{B.2.2.1}$$

and z_{cm} is the original, uncorrected RTPC vertex from the `GCPB` bank but in cm.

B.3 EC Calibration

The need for calibration of the EC becomes apparent when looking at the invariant mass distribution of photon pairs coming from the EC, as can be seen in **Fig. B.3.1** . There is clear peak near the nominal mass of π^0 but there is about a 10% shift that is consistent over all runs. First, a check is made on the sampling fraction over the course of the experiment for each sector. Then, an in-depth look at the energy dependent scaling, with the constraint of the π^0 invariant mass, is applied to each of the photons in the pair.

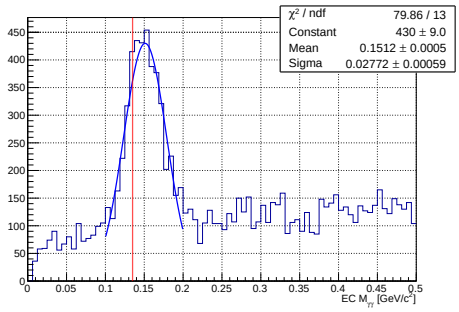

(a) The invariant mass distribution over a single run (Run Number `61510`).

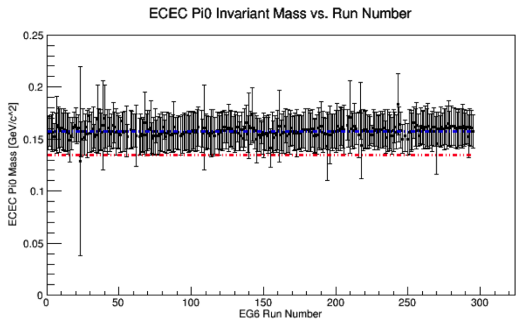

(b) The invariant mass over all runs.

Fig. B.3.1 : The invariant mass distribution of EC photon pairs over one run (B.3.1 a) and all runs (B.3.1 b). The red line represents the nominal π^0 mass and the blue represents the mean from fit to the data.

B.3.1 Sampling Fraction Correction

The sampling fraction is the fraction of the energy that a particle traversing the EC deposits in the sensitive scintillating material. Energy is deposited in the lead blocks too but that area is not sensitive to measurement. Although the sampling fraction was optimized by simulation to be 0.293, measurements show that this valued varied as a function of time (explicitly, of run number and event number). To explicitly see what its effect on each sector, a measurement of the sampling fraction over the EG6 run for

each sector was made as seen in **Fig. B.3.1.2** .

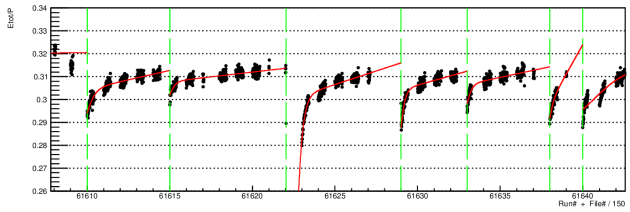

Fig. B.3.1.1 : A fit to the measured sampling fraction as a function of event number [63].

Each of these six sector sampling fractions can be fit to replace the fixed sampling fraction of 0.293. An extensive study was done by Cole Smith and then Nathan Baltzell [63] to determine the parameters of the functional form:

$$\texttt{sampFrac}\,(s,x) = E_0 + A\left(\exp\left[-\alpha\,(x-x_0)\right] + \exp\left[-\beta\,(x-x_0)\right]\right) \tag{B.3.1.1}$$

where the sampling fraction depending on the sector, s, and the effective time, $x := r + f/150$, with r and f representing the run and file number, respectively.

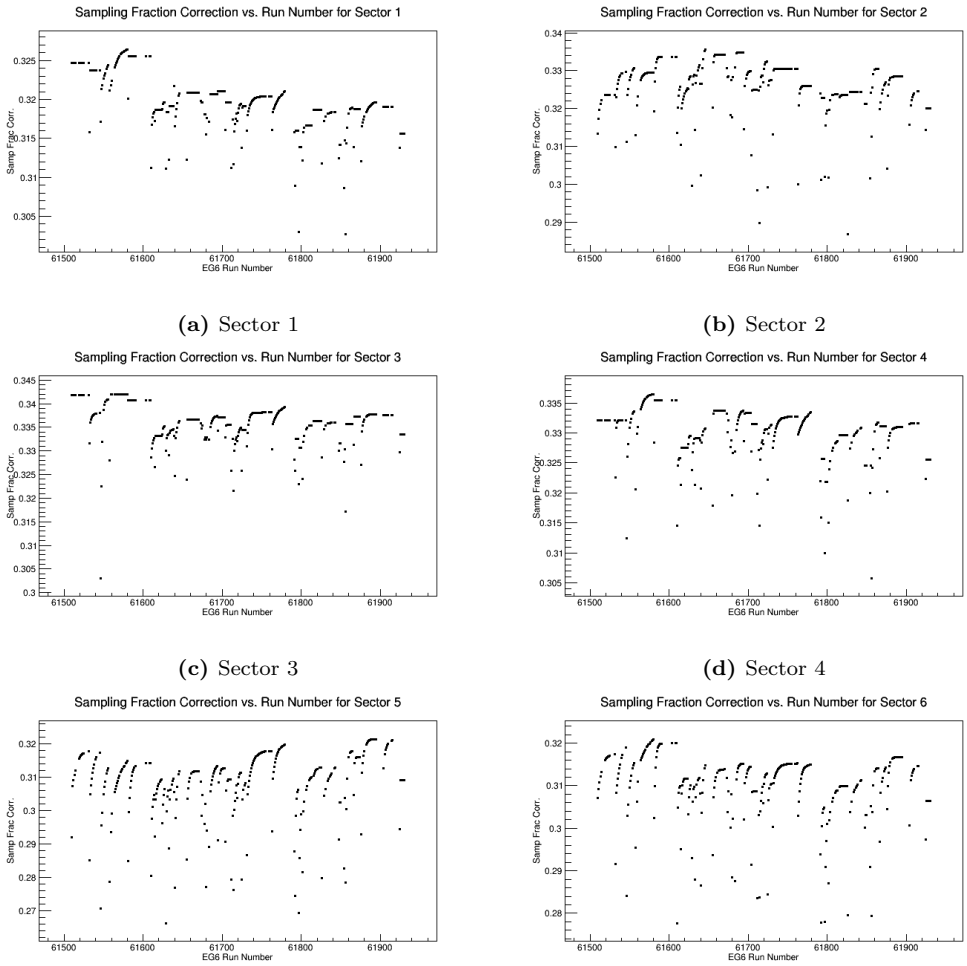

(a) Sector 1 **(b)** Sector 2

(c) Sector 3 **(d)** Sector 4

(e) Sector 5 **(f)** Sector 6

Sampling Fraction vs. Run Number for each EC sector.

Fig. B.3.1.2 : Sampling fraction vs. run number by sector

The other parameters, E_0, A, α, β, and x_0 all also depend on s and x. Overall, `sampFrac` is piece-wise in x, for each sector, as can be seen in **Fig. B.3.1.1** .

The result of the fit gives a better invariant mass distribution over the entire EG6 run, as can be seen in **Fig. B.3.1.3** .

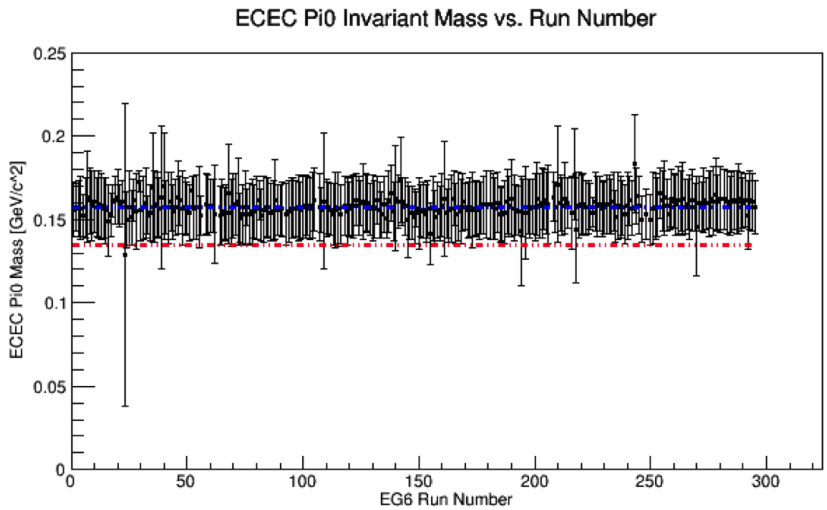

(a) Before sampling fraction correction

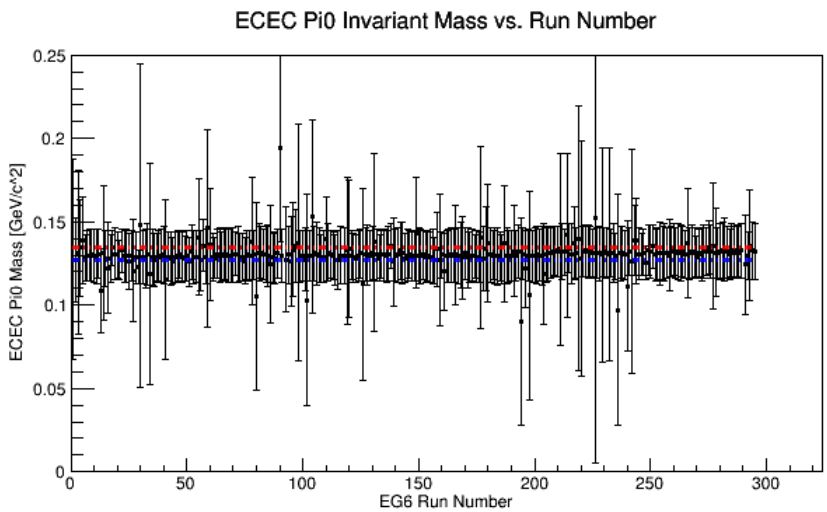

(b) After sampling fraction correction

Fig. B.3.1.3 : Comparison of the invariant mass distribution before (B.3.1.3 a) and after (B.3.1.3 b) the sampling fraction correction.

B.3.2 Scaling Factor Correction

Taking a closer look at the π^0 invariant mass as a function of run number, there is a still a uniform shift over all sectors, over all run numbers.

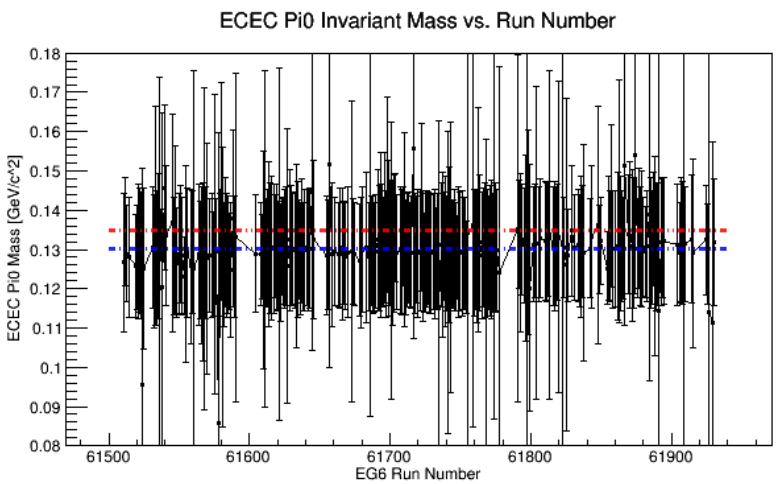

Fig. B.3.2.1 : Invariant mass distribution vs run number for EC photon pairs zoomed in.

Comparing this to the IC photon pairs, in **Fig. B.3.2.2** , we see that even when zoomed in, the shift is not as dramatic.

To see where this shift is coming from, we check to see if there is an energy dependence in the two-photon invariant mass. In **Fig. B.3.2.3** , the two-photon invariant mass is plotted against the lower energy photon. It reveals that the invariant mass may be linearly dependent on the energy of the lower photon.

Assuming that the measured EC energy, E'_γ, has a scaling factor, c, we can rewrite the energy as:

$$E'_\gamma = cE_\gamma$$

where E_γ is the true photon energy.

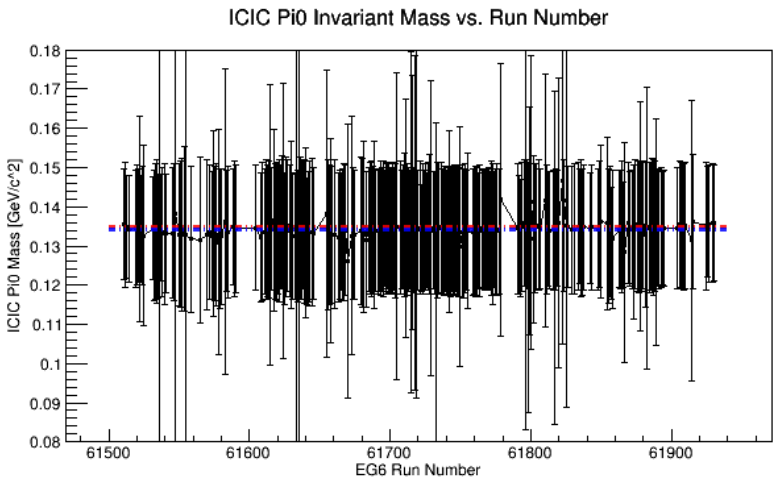

Invariant mass distribution vs run number for IC photons.

Fig. B.3.2.2 : Invariant mass distribution vs run number for IC photons

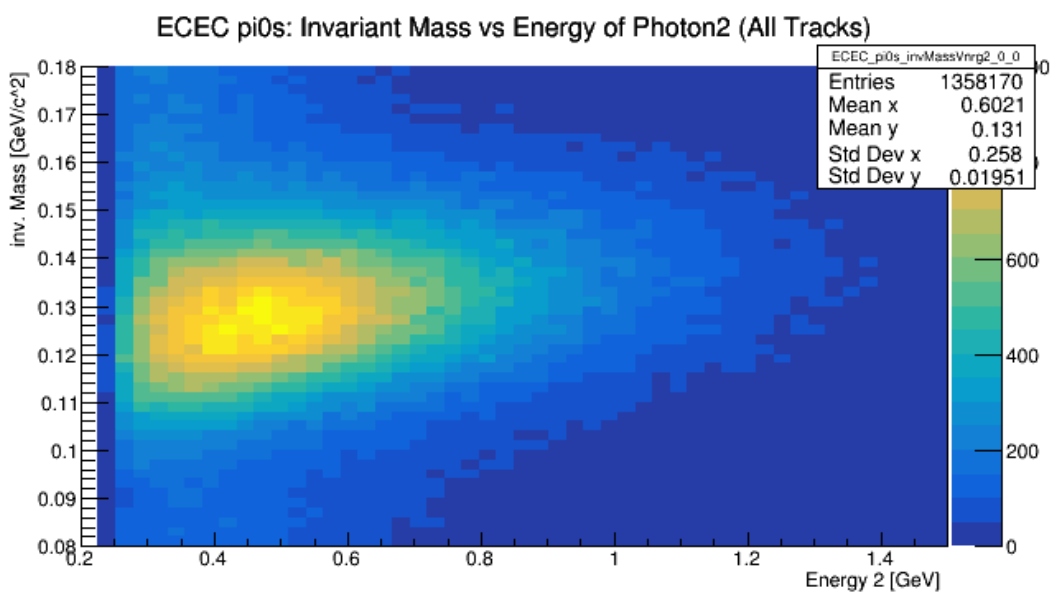

Fig. B.3.2.3 : Invariant mass of two EC photons vs. energy of the lower energy photon : The peak of the invariant mass is dependent on the energy of the lower energy photon.

Then the measured invariant mass, $M_{\gamma\gamma}$ will be expressed as, in terms of the scaling factor, c as:

$$\begin{aligned} M_{\gamma\gamma}^2 &= \left(E'_{\gamma_1} + E'_{\gamma_2}\right)^2 - \|\vec{\boldsymbol{p}}_{\gamma_1} + \vec{\boldsymbol{p}}_{\gamma_2}\|^2 \\ &= 2E'_{\gamma_1}E'_{\gamma_2}\left(1 - \cos\theta_{\gamma\gamma}\right) \\ &= 2c_1c_2E_{\gamma_1}E_{\gamma_2}\left(1 - \cos\theta_{\gamma\gamma}\right) \end{aligned}$$

To do this systematically, let us consider symmetric π^0. That is, π^0 formed from two photons with equal energy, $E_1 = E_2 =: E$ and $c_1 = c_2 =: c$. Then,

$$M_{\gamma\gamma}^2 = 2\left(cE\right)^2\left(1 - \cos\theta_{\gamma\gamma}\right)$$

and solving for the factor, c, gives

$$c = \frac{M_{\gamma\gamma}}{E\sqrt{2\left(1 - \cos\theta_{\gamma\gamma}\right)}} \quad . \tag{B.3.2.1}$$

Practically, choosing truly symmetric π^0 is too restrictive. Instead, closely symmetric π^0, with an energies satisfying $|E_1 - E_2| < 100\,\text{MeV}$, are chosen. Then **Eq. B.3.2.1** becomes:

$$\bar{c} = \frac{M_{\gamma\gamma}}{\bar{E}\sqrt{2\left(1 - \cos\theta_{\gamma\gamma}\right)}} \tag{B.3.2.2}$$

where $\bar{E}$ is the average photon energy and $\bar{c}$ is the effective scaling factor.

In **Fig. B.3.2.4** the scaling factor, $\bar{c}$, as a function of the average photon energy, $\bar{E}'$ is plotted. We see that this scaling factor is dependent on $\bar{E}'$:

$$\bar{c} \equiv \bar{c}\left(\bar{E}'\right) \quad . \tag{B.3.2.3}$$

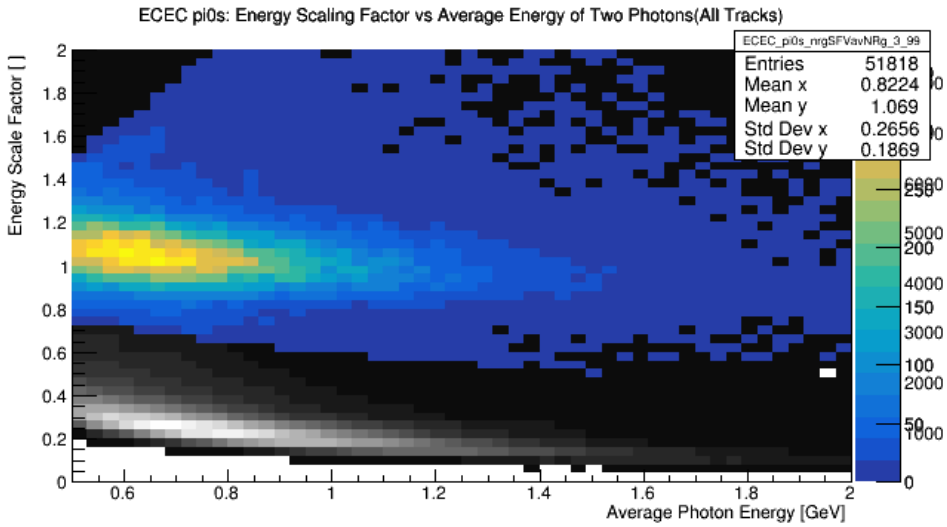

Fig. B.3.2.4 : Scaling factor vs. average energy: The energy scaling factor depends on energy.

Although, on first glance it looks linear, slicing the distribution into strips, the profile, represented as a candle-plot in **Fig. B.3.2.5** , reveals that the relationship more complex than a linear one.

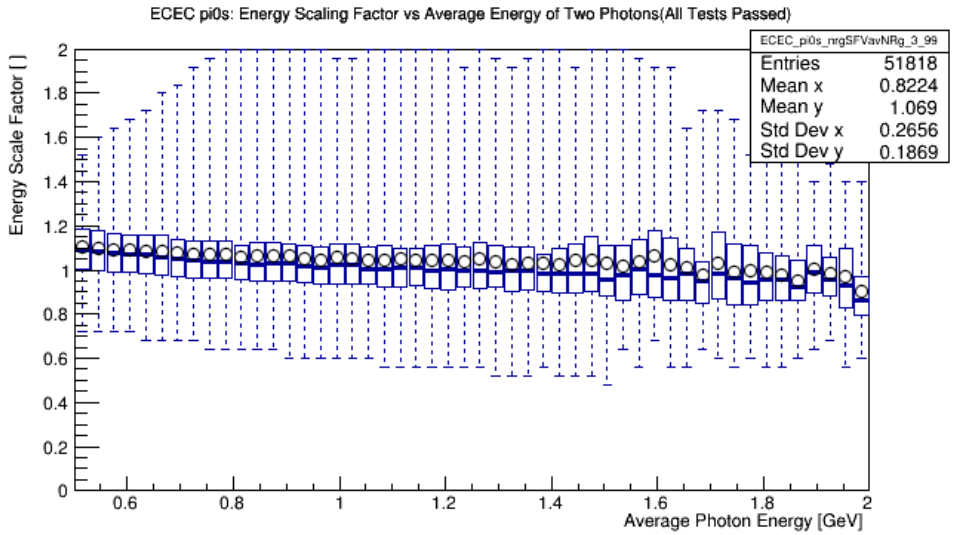

Fig. B.3.2.5 : Scaling factor vs. average energy: Candle-plot profile of **Fig. B.3.2.4** .

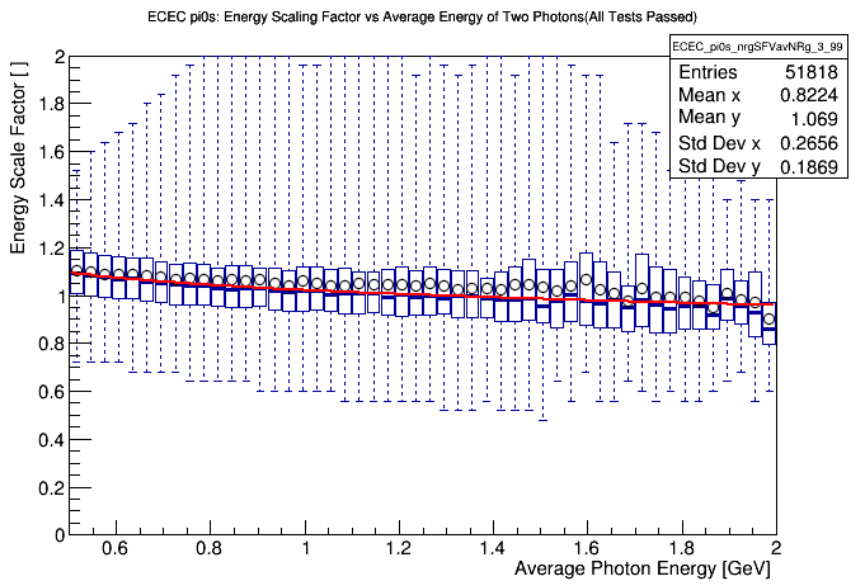

Fig. B.3.2.6 : Scaling factor vs. average energy: Candle-plot profile of **Fig. B.3.2.4** with fit **Eq. B.3.2.4**.

A fit of the form:

$$c\,(E) = 1 + aE + \frac{b}{E} \tag{B.3.2.4}$$

is applied and a qualitative look can be seen in **Fig. B.3.2.6** . The values of fit parameters a and b are listed in **Table B.2**.

Parameter	**Value**	**Units**
a	-0.0354677	GeV^{-1}
b	0.0563963	GeV

Table B.2: Scaling Factor Parameters

To see how it affects the invariant mass of EC photon pairs, we see how it affects symmetric π^0's with low energy photons and high energy photons:

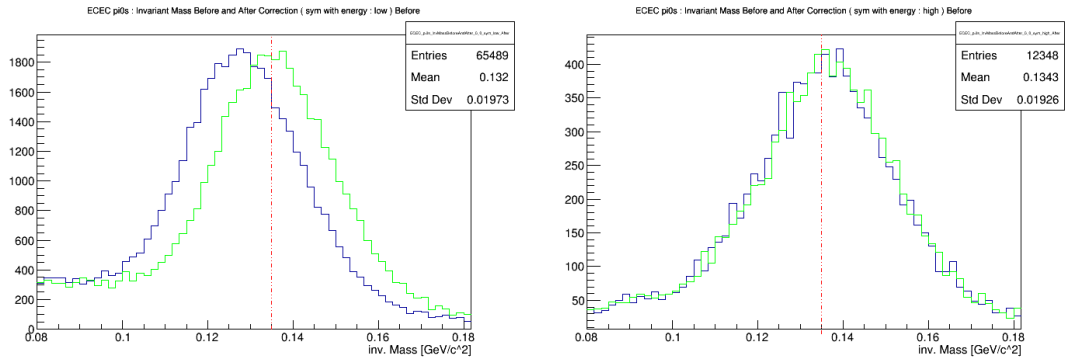

(a) Low energy ($E_{\gamma\gamma} < 1.8GeV$) invariant mass distribution.

(b) High energy ($E_{\gamma\gamma} > 1.8GeV$) invariant mass distribution.

Fig. B.3.2.7 : Invariant mass distribution for low (B.3.2.7 a) and high (B.3.2.7 b) energy symmetric EC π^0. The blue and green are the uncorrected and corrected distributions, respectively. The red is the nominal value of the π^0 invariant mass.

We see that this correction does exactly what we want: it scales up the poorly reconstructed low energy EC photons, while leaving the well reconstructed EC photons essentially unchanged (see **Fig. B.3.2.7**). To check if this correction only works for symmetric π^0, this symmetric criterion is lifted and the invariant mass is checked again.

Again, we see from **Fig. B.3.2.8** , that higher energy π^0 are unchanged and the lower energy π^0 are shifted in the right direction. This shows that although the symmetric π^0 were used to simplify the correction, the correction cares only on the energy of the individual photons, justifying the omission of the bars in **Eq. B.3.2.4**.

Here, we can see that the invariant mass is shifted much closer to the nominal value for each run (**Fig. B.3.2.10**), and integrated over all runs (**Fig. B.3.2.9**).

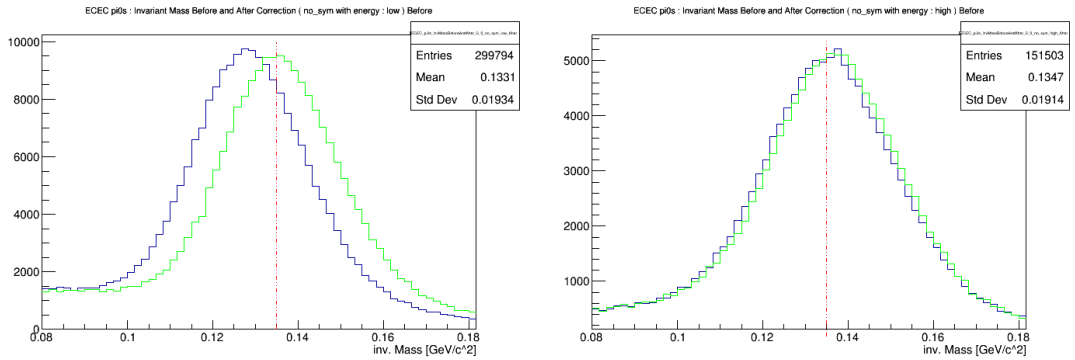

(a) Low energy ($E_{\gamma\gamma} < 1.8GeV$) invariant mass distribution.

(b) High energy ($E_{\gamma\gamma} > 1.8GeV$) invariant mass distribution.

Fig. B.3.2.8 : Invariant mass distribution for low (B.3.2.8 a) and high (B.3.2.8 b) energy generic EC π^0. The blue and green are the uncorrected and corrected distributions, respectively. The red is the nominal value of the π^0 invariant mass.

- -

In summary, the sampling fraction correction shifts the invariant mass closer to nominal value but overshoots by quite a bit. A study of the symmetric π^0 reveal that this overshot was due to poorly reconstructed low EC energy photons. These are corrected and combined, giving a better measurement of energy coming from the EC.

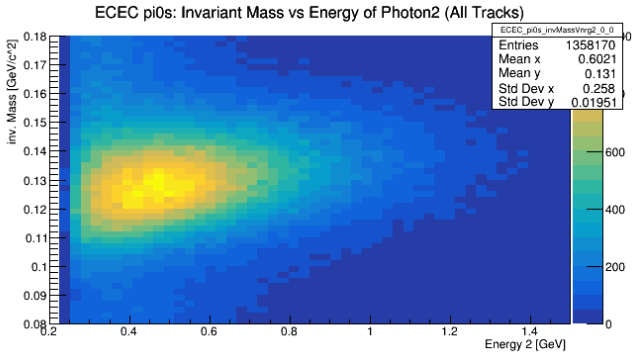

(a) Before sampling fraction correction

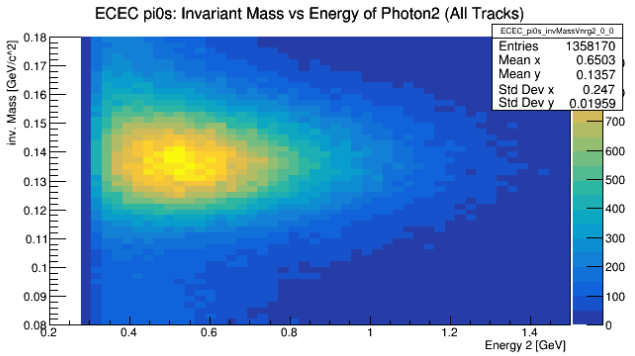

(b) After sampling fraction correction

Fig. B.3.2.9 : Comparison of the invariant mass distribution vs energy of lower energy photon before (B.3.2.9 a) and after (B.3.2.9 b) the sampling fraction correction.

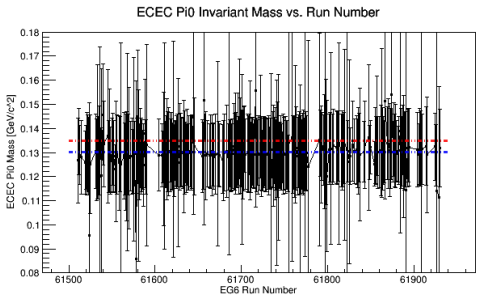

(a) Before scaling factor correction (but after sampling fraction correction)

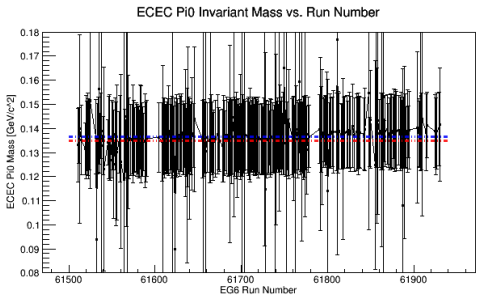

(b) After scaling factor correction

Fig. B.3.2.10 : Comparison of the invariant mass distribution vs run number before (B.3.2.10 a) and after (B.3.2.10 b) the scaling factor correction.

Furthermore, the invariant mass of the photon pairs show an enhancement of the peak right around the nominal value for η. Although there are very few events that pass event selection, a yield can be estimated with the right cuts (as seen in **Fig. B.3.2.12**).

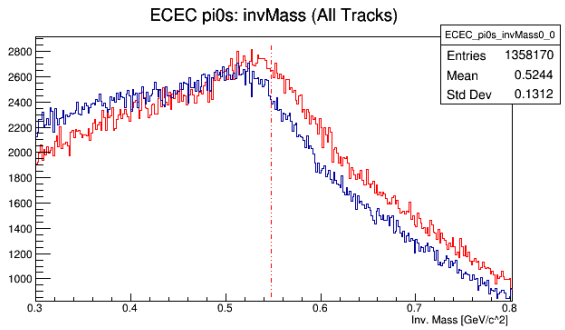

Fig. B.3.2.11 : Invariant mass distribution of generic EC photon pairs. The blue and red are the uncorrected and corrected distributions, respectively. The red is the nominal value of the η invariant mass.

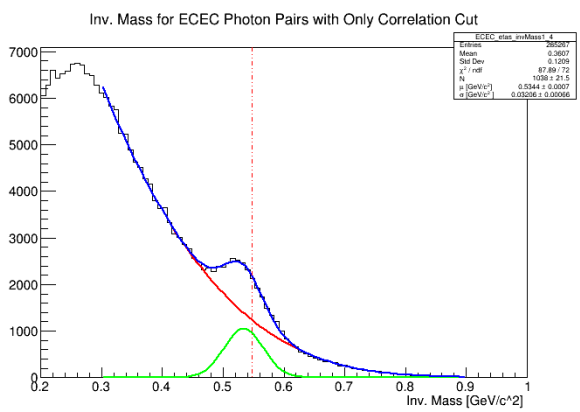

Fig. B.3.2.12 : Invariant mass distribution of EC photons coming from neighoring sectors. The blue, red, and green are the full corrected, fitted background, and the extracted signal (from subtracting fitted background distribution from full distribution) distributions, respectively. The red is the nominal value of the η invariant mass.

C Supplemental Psuedocode for PID

C.1 EC Fiducial Cut

`u, v,` and `w` make up the coordinates of the EC's scintillating strips, are explicitly given by

```
u = (y_rel - y_lo)/sin(rho)

v = (y_hi - y_lo)/tan(rho) - x_rel + (y_hi - y_rel)/tan(rho)

w = (0.5/cos(rho))*((y_hi - y_lo)/tan(rho) + x_rel + (y_hi - y_rel)/tan(rho))
```

having relative `x_rel` and `y_rel` coming from the linear transformation:

$$\begin{bmatrix} \texttt{x\_rel} \\ \texttt{y\_rel} \\ \texttt{z\_rel} \end{bmatrix} = \begin{bmatrix} \cos(\theta_{\mathrm{EC}})\cos(\phi_{\mathrm{EC}}) & -\sin(\phi_{\mathrm{EC}}) & \sin(\theta_{\mathrm{EC}})\cos(\phi_{\mathrm{EC}}) \\ \cos(\theta_{\mathrm{EC}})\sin(\phi_{\mathrm{EC}}) & \cos(\phi_{\mathrm{EC}}) & \sin(\theta_{\mathrm{EC}})\sin(\phi_{\mathrm{EC}}) \\ -\sin(\theta_{\mathrm{EC}}) & 0. & \cos(\theta_{\mathrm{EC}}) \end{bmatrix} \begin{bmatrix} \texttt{x\_ec} \\ \texttt{y\_ec} \\ \texttt{z\_ec} \end{bmatrix} - \begin{bmatrix} 0.00 \\ 0.00 \\ 510.32 \end{bmatrix} .$$

Here `x_ec`, `y_ec`, and `z_ec` are the $x-$, $y-$, and $z-$ coordinates of the EC hit with

```
x_ec = ech_x[ec[ipart]-1]

y_ec = ech_y[ec[ipart]-1]  .

z_ec = ech_z[ec[ipart]-1]
```

The EC sector's central azimuthal angle, ϕ_{EC}, is determined from sector index, `isect` ($\in \{0, \ldots, 5\}$), which depends on the particle's shifted azimuthal angle, ϕ_{shifted} ($\in [0, 360]^{\circ}$):

$$\phi_{\mathrm{EC}} = \texttt{isect} * \frac{2\pi}{6};$$
$$\texttt{isect} = \lfloor \phi_{\mathrm{shifted}}/60^{\circ} \rfloor$$

The rest of the variables, listed in **Table C.3**, are hard-coded, fixed values representing the geometrical configuration of the EC.

Variable	**Value**	**Units**
θ_{EC}	0.4363323	rad.
`rho`	1.0976200	rad.
`y_lo`	-182.974	cm
`y_hi`	189.956	cm

Table C.3: Constant EC Parameters

C.2 IC Hot Channels Cut

Index `i`	`ix_bad[i]`	`iy_bad[i]`
0	-8	-2
1	-4	-6
2	-2	-6
3	-1	-6
4	3	-8
5	8	-10
6	-5	8
7	-9	-6

Table C.4: Index of bad IC crystals

The hot channels that are overactive are taken out by explicitly looping over the bad crystals:

```
isInICHotChannel(ix, iy){
  for( int ii = 0; ii < 8; ii++ ){
    x_bad = ix_bad[ii]
    y_bad = iy_bad[ii]
    if( ix == x_bad && iy == y_bad )
      return true
  }
  return false
}
```

where `ix_bad` and `iy_bad` are arrays tabulated in **Table C.4**.

C.3 IC Fiducial Cuts

The IC Fiducial is defined as:

```
isInICFiducial(x,y){
  if( isOutICOuterEdge(x,y) ) return false
  if( isInICnnerEdge(x,y)   ) return false
  return true
}
```

where the cut requires passing the inner and outer edge cuts of the calorimeter.

C.3.1 IC Fiducial Outer Edge Cut

The outer calorimeter cut, `isOutICOuterEdge(x,y)`, can be expressed as:

```
isOutICOuterEdge(x,y){
  if( abs(x)/dx          >= nout           ||
      abs(y)/dy          >= nout           ||
      abs( x/dx - y/dy ) >= nout * sqrt(2) ||
      abs( x/dx + y/dy ) >= nout * sqrt(2)
    ) return true
  return false
}
```

returning `false` if the hit is outside the outer fiducial region and `true` if it is inside.

C.3.2 IC Fiducial Inner Edge Cut

The inner calorimeter cut, `isInICInnerEdge(x,y)`, can be expressed as

```
isInICInnerEdge(x,y){
  if( abs(x)/dx          <= nin           &&
      abs(y)/dy          <= nin           &&
      abs( x/dx - y/dy ) <= nin * sqrt(2) &&
      abs( x/dx + y/dy ) <= nin * sqrt(2)
    ) return true
  return false
}
```

returning `false` if the hit is outside the inner fiducial region and `true` if it is inside.

The hard-coded parameters in the expressions above are listed in **Table C.5**, represent the size of the pixel and the number of pixels to the inner and outer diagonal of the octagonal cut applied to the IC.

Variable	Value	Units
`dx`	1.346	cm
`dy`	1.360	cm
`nin`	3.25	–
`nout`	10.75	–

Table C.5: Constant IC Parameters

C.4 RTPC Fiducial Cuts

The RTPC Fiducial Cut, `isInRTPCFiducial`, depends on three other cuts:

```
isInRTPCFiducial(vz, theta, phi){
  if( !isInRTPCDrift(vz, theta)   ) return false
  if(  isInRTPCSupport(phi)       ) return false
  if(  isInRTPCHolder(vz, theta)  ) return false
  return true
}
```

Failing any one of these other cuts results in rejection of the RTPC track entirely.

C.4.1 Drift Region Fiducial Cut

To ensure the track is coming inside the drift region, a fiducial cut is place:

```
isInRTPCDrift(vz, theta){
   if( abs(z1) > 10 ) return false
   if( abs(z2) > 10 ) return false
}
```

where `z1` and `z2` are the reconstructed particle's projected z-components when it hits the inner cathode, at `rinner`, and outer anode, at `router`, respectively:

```
z1 = (vz+64) + cos(theta)*rinner/abs(sin(theta))
```

```
z2 = (vz+64) + cos(theta)*router/abs(sin(theta))
```

with

```
rinner = 3

router = 6
```

in cm. The shift of 64 cm is to account for the target being placed at -64 cm with respect to the nominal center of CLAS.

C.4.2 Support Region Fiducial Cut

The left and right sides of the RTPC is separated by two mechanical supports, one at the top and and one at the bottom, with an azimuthal angular extent of 30°. Tracks reconstructed that hit these supports are rubbish. The cut is introduced to deal with these:

```
isInRTPCSupport(phi){
   if( abs(phi_shifted -  90) < 30 ) return false
   if( abs(phi_shifted - 270) < 30 ) return false
}
```

where `phi_shifted` is the reconstructed azimuthal angle, ϕ, in degrees, so that the top support is centered at `phi_shifted`= 90° and the bottom support is centered at `phi_shifted`= 270°

```
phi_shifted = phi

if( phi_shifted < 0 ) while( phi_shifted <  0    ) phi_shifted += 2*pi

else                  while( phi_shifted >= 2*pi ) phi_shifted -= 2*pi
```

C.4.3 Target Holder Fiducial Cut

To remove the tracks originating from the target holder, the fiducial cut is used:

```
isInRTPCHolder(vz, theta){

  cz = cos(theta)

  vz = 10 * (vz + 64)

  dz = z_targ - vz

  if( cz < cos( atan2(r_targ, dz) ) ) return false

}
```

where `vz` is shifted from the center of CLAS, `z_targ` is the position of the target's downstream end and `r_targ` is the target's radius:

```
r_targ =   2.5

z_targ = -84.0
```

are all in mm.

D Solving for Kinematic Fitting Variables

The conditions to minimize the Lagrangian in **Section 7.1.2.1**:

$$\vec{\mathbf{0}} \equiv \frac{1}{2}\left(\frac{\partial \mathcal{L}}{\partial \vec{\boldsymbol{\delta}}}\right)^{\nu} = C_{\eta}^{-1}\vec{\boldsymbol{\epsilon}}^{\nu} + (B^{\nu})^{T}\,\vec{\boldsymbol{\mu}}^{\nu} = C_{\eta}^{-1}\left(\vec{\boldsymbol{\delta}}^{\nu} + \vec{\boldsymbol{\epsilon}}^{\nu-1}\right) + (B^{\nu})^{T}\,\vec{\boldsymbol{\mu}}^{\nu} \tag{D.1}$$

$$\vec{\mathbf{0}} \equiv \frac{1}{2}\left(\frac{\partial \mathcal{L}}{\partial \vec{\boldsymbol{\mu}}}\right)^{\nu} = A^{\nu}\,\vec{\boldsymbol{\xi}}^{\nu} + B^{\nu}\,\vec{\boldsymbol{\delta}}^{\nu} + \vec{\boldsymbol{c}}^{\nu} \tag{D.2}$$

$$\vec{\mathbf{0}} \equiv \frac{1}{2}\left(\frac{\partial \mathcal{L}}{\partial \vec{\boldsymbol{\xi}}}\right)^{\nu} = (\vec{\boldsymbol{\mu}}^{\nu})^{T}\,A^{\nu} = (A^{\nu})^{T}\,\vec{\boldsymbol{\mu}}^{\nu} \tag{D.3}$$

where identity $\vec{\boldsymbol{\epsilon}}^{\nu} \equiv \vec{\boldsymbol{\delta}}^{\nu} + \vec{\boldsymbol{\epsilon}}^{\nu-1}$ is used in **Eq. D.1** from the fact that:

$$\begin{aligned}
\vec{\boldsymbol{\epsilon}}^{\nu} &:= \vec{\boldsymbol{y}}^{\nu} - \vec{\boldsymbol{\eta}} = \vec{\boldsymbol{y}}^{\nu} - \vec{\boldsymbol{y}}^{0} \\
&= \vec{\boldsymbol{y}}^{\nu} + \left[\left(-\vec{\boldsymbol{y}}^{\nu-1} + \vec{\boldsymbol{y}}^{\nu-1}\right) + \ldots + \left(-\vec{\boldsymbol{y}}^{1} + \vec{\boldsymbol{y}}^{1}\right)\right] - \vec{\boldsymbol{y}}^{0} \\
&= \left(\vec{\boldsymbol{y}}^{\nu} - \vec{\boldsymbol{y}}^{\nu-1}\right) + \ldots + \left(\vec{\boldsymbol{y}}^{1} - \vec{\boldsymbol{y}}^{0}\right) \\
&= \sum_{j=1}^{\nu} \vec{\boldsymbol{\delta}}^{j} \quad .
\end{aligned}$$

To solve for each $\vec{\boldsymbol{\mu}}^{\nu}$, $\vec{\boldsymbol{\delta}}^{\nu}$, $\vec{\boldsymbol{\xi}}^{\nu}$ that satisfy **Eqs. D.1,D.2,D.3**s' conditions, we start with $\vec{\boldsymbol{\xi}}^{\nu}$, multiplying $[B^{\nu}C_{\eta}]$ to **Eq. D.1**:

$$\begin{aligned}
[B^{\nu}C_{\eta}]\left(C_{\eta}^{-1}\left(\vec{\boldsymbol{\delta}}^{\nu} + \vec{\boldsymbol{\epsilon}}^{\nu-1}\right) + (B^{\nu})^{T}\,\vec{\boldsymbol{\mu}}^{\nu}\right) &\equiv \vec{\mathbf{0}} \\
B^{\nu}\left(\vec{\boldsymbol{\delta}}^{\nu} + \vec{\boldsymbol{\epsilon}}^{\nu-1}\right) + \left[B^{\nu}C_{\eta}\,(B^{\nu})^{T}\right]\vec{\boldsymbol{\mu}}^{\nu} &\equiv \vec{\mathbf{0}}
\end{aligned}$$

$$\Rightarrow \qquad B^{\nu}\,\vec{\boldsymbol{\delta}}^{\nu} = -\left(\left[B^{\nu}C_{\eta}\,(B^{\nu})^{T}\right]\vec{\boldsymbol{\mu}}^{\nu} + B^{\nu}\,\vec{\boldsymbol{\epsilon}}^{\nu-1}\right) \quad . \tag{D.4}$$

Rearranging **Eq. D.2** and equating expressions for $-B^{\nu}\,\vec{\boldsymbol{\delta}}^{\nu}$ with **Eq. D.4**, we obtain

$$A^{\nu}\,\vec{\boldsymbol{\xi}}^{\nu} + \vec{\boldsymbol{c}}^{\nu} = \left[B^{\nu}C_{\eta}\,(B^{\nu})^{T}\right]\vec{\boldsymbol{\mu}}^{\nu} + B^{\nu}\,\vec{\boldsymbol{\epsilon}}^{\nu-1}$$

$$A^{\nu}\vec{\boldsymbol{\xi}}^{\nu} + \vec{\boldsymbol{c}}^{\nu} - B^{\nu}\vec{\boldsymbol{\epsilon}}^{\nu-1} = \left[B^{\nu}C_{\eta}\left(B^{\nu}\right)^{T}\right]\vec{\boldsymbol{\mu}}^{\nu} \quad . \tag{D.5}$$

Eliminating the $\vec{\boldsymbol{\mu}}$ term by using **Eq. D.3**, we have

$$\left[\left(A^{\nu}\right)^{T}C_{B}^{\nu}\right]\left(A^{\nu}\vec{\boldsymbol{\xi}}^{\nu} + \vec{\boldsymbol{c}}^{\nu} - B^{\nu}\vec{\boldsymbol{\epsilon}}^{\nu-1}\right) = \left[\left(A^{\nu}\right)^{T}C_{B}^{\nu}\right]\left[B^{\nu}C_{\eta}\left(B^{\nu}\right)^{T}\right]\vec{\boldsymbol{\mu}}^{\nu}$$

where C_B^{ν} is defined as

$$C_{B}^{\nu} := \left[B^{\nu}C_{\eta}\left(B^{\nu}\right)^{T}\right]^{-1} \quad .$$

Then,

$$\left[\left(A^{\nu}\right)^{T}C_{B}^{\nu}\right]\left(A^{\nu}\vec{\boldsymbol{\xi}}^{\nu} + \vec{\boldsymbol{c}}^{\nu} - B^{\nu}\vec{\boldsymbol{\epsilon}}^{\nu-1}\right) \equiv \vec{\mathbf{0}}$$

$$\Rightarrow \left[\left(A^{\nu}\right)^{T}C_{B}^{\nu}A^{\nu}\right]\vec{\boldsymbol{\xi}}^{\nu} = -\left[\left(A^{\nu}\right)^{T}C_{B}^{\nu}\right]\left(\vec{\boldsymbol{c}}^{\nu} - B^{\nu}\vec{\boldsymbol{\epsilon}}^{\nu-1}\right)$$

$$\vec{\boldsymbol{\xi}}^{\nu} = -C_{x}^{\nu}\left[\left(A^{\nu}\right)^{T}C_{B}^{\nu}\right]\left(\vec{\boldsymbol{r}}^{\nu}\right) \tag{D.6}$$

where $\vec{\boldsymbol{r}}^{\nu}$ and C_x^{ν} are defined as

$$\begin{aligned} \vec{\boldsymbol{r}}^{\nu} &:= \vec{\boldsymbol{c}}^{\nu} - B^{\nu}\vec{\boldsymbol{\epsilon}}^{\nu-1} \\ C_{x}^{\nu} &:= \left[\left(A^{\nu}\right)^{T}C_{B}^{\nu}A^{\nu}\right]^{-1} \end{aligned} \quad ,$$

respectively.

To get $\vec{\boldsymbol{\mu}}^{\nu}$ we go back and rewrite **Eq. D.5** with our newly defined variables:

$$\left(C_{B}^{\nu}\right)^{-1}\vec{\boldsymbol{\mu}}^{\nu} = A^{\nu}\vec{\boldsymbol{\xi}}^{\nu} + \vec{\boldsymbol{r}}^{\nu}$$

$$\vec{\boldsymbol{\mu}}^{\nu} = C_{B}^{\nu}\left(A^{\nu}\vec{\boldsymbol{\xi}}^{\nu} + \vec{\boldsymbol{r}}^{\nu}\right) \tag{D.7}$$

Finally, to get $\vec{\boldsymbol{\delta}}^{\nu}$, we go back to **Eq. D.4**:

$$B^{\nu}\vec{\boldsymbol{\delta}}^{\nu} = -\left(\left[B^{\nu}C_{\eta}\left(B^{\nu}\right)^{T}\right]\vec{\boldsymbol{\mu}}^{\nu} + B^{\nu}\vec{\boldsymbol{\epsilon}}^{\nu-1}\right)$$

$$\vec{\boldsymbol{\delta}}^{\nu} = -C_{\eta}\left(B^{\nu}\right)^{T}\vec{\boldsymbol{\mu}}^{\nu} - \vec{\boldsymbol{\epsilon}}^{\nu-1} \tag{D.8}$$

- -

In summary, we obtain the vectors that minimize the Lagrangian **Eq. 7.4**, meeting minimization conditions **Eq. 7.5** that are listed in **Eq. 7.6** and below:

$$\vec{\boldsymbol{\xi}}^{\nu} = -C_{x}^{\nu}\left(A^{\nu}\right)^{T}C_{B}^{\nu}\vec{\boldsymbol{r}}^{\nu}$$

$$\vec{\boldsymbol{\mu}}^{\nu} = C_{B}^{\nu}\left(A^{\nu}\vec{\boldsymbol{\xi}}^{\nu} + \vec{\boldsymbol{r}}^{\nu}\right)$$

$$\vec{\boldsymbol{\delta}}^{\nu} = -C_{\eta}\left(B^{\nu}\right)^{T}\vec{\boldsymbol{\mu}}^{\nu} - \vec{\boldsymbol{\epsilon}}^{\nu-1}$$

References

[1] J. C. Collins, D. E. Soper, and G. F. Sterman, "Factorization of Hard Processes in QCD," *Adv. Ser. Direct. High Energy Phys.*, vol. 5, pp. 1–91, 1989.

[2] C.-R. Ji, H.-M. Choi, A. Lundeen, and B. L. G. Bakker, "Beam Spin Asymmetry in Electroproduction of Pseudoscalar or Scalar Meson Production off the Scalar Target," 2018.

[3] C. Patrignani *et al.*, "Review of Particle Physics," *Chin. Phys.*, vol. C40, no. 10, p. 100001, 2016.

[4] M. Hattawy, *Deeply Virtual Compton Scattering Off* ^{4}*He*. PhD thesis, Institut de Physique Nucléaire (IPN), September 2015.

[5] B. Torayev, "Electroproduction of Neutral Pion Off ^{4}He," *CLAS Note*, December 2016.

[6] M. Hattawy *et al.*, "First Exclusive Measurement of Deeply Virtual Compton Scattering off ^{4}He: Toward the 3D Tomography of Nuclei," *Phys. Rev. Lett.*, vol. 119, p. 202004, Nov 2017.

[7] M. Hattawy *et al.*, "Deeply Virtual Compton Scattering Measurement Off Bound Protons," 2018.

[8] F. Girod, *Deeply Virtual Compton Scattering (Beam Spin Asymmetries) for the study of Generalized Parton Distributions*. PhD thesis, Louis Pasteur University, December 2006.

[9] N. Baltzell, *A Search for the Exotic* Θ^+ *Pentaquark in* $\gamma d \to ppK^0K^-$. PhD thesis, University of South Carolina, September 2001.

[10] H.-S. Jo, *Deeply Virtual Compton Scattering on the Nucleon with the CLAS Detector of Jefferson Lab : Measurement of the polarized and unpolarized Cross Sections*. Theses, Université Paris Sud - Paris XI, Mar. 2007.

[11] R. De Masi *et al.*, "Measurement of $e\ p \to e\ p\ \pi^0$ Beam Spin Asymmetries Above the Resonance Region," *Phys. Rev.*, vol. C77, p. 042201, 2008.

[12] B. Zhao *et al.*, "Measurement of the Beam Spin Asymmetry of $\overrightarrow{e}\ p \to e\ p\ \eta$ in the Deep-Inelastic Regime with CLAS," *Physics Letters B*, vol. 789, pp. 426 – 431, 2019.

[13] A. G. Frodesen, O. Skjeggestad, and H. Tofte, *Probability and Statistics in Particle Physics*. Universitetsforlaget, 1971.

[14] M. Williams and C. A. Meyer, "Kinematic Fitting in CLAS," *CLAS Note*, November 2003.

[15] M. Williams, D. Applegate, and C. A. Meyer, "Determining Momentum and Energy Corrections for g1c Using Kinematic Fitting," *CLAS Note*, June 2004.

[16] P. T. Mattione, "Kinematic Fitting of Detached Vertices," Master's thesis, Rice University, 2007.

[17] P. T. Mattione and D. S. Carman, "CLAS g13 Experiment Studies," *CLAS Note*, 2017.

[18] D. Keller, "Techniques in Kinematic Fitting," *CLAS Note*, November 2010.

[19] R. Frisch and O. Stern, "Über die magnetische ablenkung von wasserstoffmolekülen und das magnetische moment des protons. i," *Zeitschrift für Physik*, vol. 85, pp. 4–16, Jan 1933.

[20] I. Estermann and O. Stern, "Über die magnetische ablenkung von wasserstoffmolekülen und das magnetische moment des protons. ii," *Zeitschrift für Physik*, vol. 85, pp. 17–24, Jan 1933.

[21] R. Hofstadter and R. McAllister, "Electron Scattering from the Proton," *Phys. Rev*, April 1955.

[22] M. N. Rosenbluth, "High energy elastic scattering of electrons on protons," *Phys. Rev.*, vol. 79, pp. 615–619, Aug 1950.

[23] C. F. Perdrisat, V. Punjabi, and M. Vanderhaeghen, "Nucleon Electromagnetic Form Factors," *Prog. Part. Nucl. Phys.*, vol. 59, pp. 694–764, 2007.

[24] R. Hofstadter, "The Electron-Scattering Method and its Application to the Structure of Nuclei and Nucleons," *Nobel Lecture*, December 1961.

[25] J. I. Friedman and H. W. Kendall, "Deep Inelastic Electron Scattering," *Annual Review of Nuclear Science*, vol. 22, April 1972.

[26] M. Breidenbach, J. I. Friedman, H. W. Kendall, E. D. Bloom, D. H. Coward, H. DeStaebler, J. Drees, L. W. Mo, and R. E. Taylor, "Observed Behavior of Highly Inelastic Electron-Proton Scattering," *Phys. Rev. Lett.*, vol. 23, pp. 935–939, Oct 1969.

[27] W. Armstrong, *Measurement of the Proton A_1 and A_2 Spin Asymmetries: Probing Color Forces*. PhD thesis, Temple University, May 2015.

[28] M. Gell-Mann, "A Schematic Model of Baryons and Mesons," *Phys. Lett.*, vol. 8, pp. 214–215, 1964.

[29] G. Zweig, "An SU(3) model for strong interaction symmetry and its breaking. Version 2," in *DEVELOPMENTS IN THE QUARK THEORY OF HADRONS. VOL. 1. 1964 - 1978* (D. Lichtenberg and S. P. Rosen, eds.), pp. 22–101, " ", 1964.

[30] R. P. Feynman, "Very High-Energy Collisions of Hadrons," *Phys. Rev. Lett.*, vol. 23, pp. 1415–1417, Dec 1969.

[31] S. Drell and J. Walecka, "Electrodynamic Processes with Nuclear Targets," *Annals of Physics*, vol. 28, no. 1, pp. 18 – 33, 1964.

[32] Y. L. Dokshitzer, "Calculation of the Structure Functions for Deep Inelastic Scattering and e+ e- Annihilation by Perturbation Theory in Quantum Chromodynamics.," *Sov. Phys. JETP*, vol. 46, pp. 641–653, 1977. [Zh. Eksp. Teor. Fiz.73,1216(1977)].

[33] J. Beringer *et al.*, "Review of particle physics," *Phys. Rev. D*, vol. 86, p. 010001, Jul 2012.

[34] R. Placakyte, "Parton Distribution Functions," in *Proceedings, 31st International Conference on Physics in collisions (PIC 2011): Vancouver, Canada, August 28-September 1, 2011*, 2011.

[35] C. Lorcé, B. Pasquini, and M. Vanderhaeghen, "Unified framework for generalized and transverse-momentum dependent parton distributions within a 3Q light-cone picture of the nucleon," *JHEP*, vol. 05, p. 041, 2011.

[36] A. Bacchetta, M. Diehl, K. Goeke, A. Metz, P. J. Mulders, and M. Schlegel, "Semi-inclusive deep inelastic scattering at small transverse momentum," *JHEP*, vol. 02, p. 093, 2007.

[37] A. V. Belitsky and A. V. Radyushkin, "Unraveling Hadron Structure with Generalized Parton Distributions," *Phys. Rept.*, vol. 418, pp. 1–387, 2005.

[38] A. V. Radyushkin, "Nonforward Parton Distributions," *Phys. Rev.*, vol. D56, pp. 5524–5557, 1997.

[39] R. L. Jaffe, "Spin, Twist and Hadron Structure in Deep Inelastic Processes," in *The Spin Structure of the Nucleon. Proceedings, International School of Nucleon Structure, 1st Course, Erice, Italy, August 3-10, 1995*, pp. 42–129, 1996.

[40] I. Bedlinskiy *et al.*, "Exclusive π^0 Electroproduction at $W > 2$ GeV with CLAS," *Phys. Rev.*, vol. C90, no. 2, p. 025205, 2014. [Addendum: Phys. Rev.C90,no.3,039901(2014)].

[41] A. Bacchetta, U. D'Alesio, M. Diehl, and C. A. Miller, "Single-spin Asymmetries: The Trento Conventions," *Phys. Rev.*, vol. D70, p. 117504, 2004.

[42] G. R. Goldstein, J. O. G. Hernandez, and S. Liuti, "Flexible parametrization of generalized parton distributions from deeply virtual compton scattering observables," *Phys. Rev. D*, vol. 84, p. 034007, Aug 2011.

[43] G. R. Goldstein, J. O. Gonzalez Hernandez, and S. Liuti, "Flexible Parametrization of Generalized Parton Distributions: The Chiral-Odd Sector," *Phys. Rev.*, vol. D91, no. 11, p. 114013, 2015.

[44] S. V. Goloskokov and P. Kroll, "Transversity in Hard Exclusive Electroproduction of Pseudoscalar Mesons," *Eur. Phys. J.*, vol. A47, p. 112, 2011.

[45] F. X. Girod *et al.*, "Measurement of Deeply Virtual Compton Scattering Beam-Spin Asymmetries," *Phys. Rev. Lett.*, vol. 100, p. 162002, 2008.

[46] J. C. Collins and A. Freund, "Proof of Factorization for Deeply Virtual compton Scattering in QCD," *Phys. Rev.*, vol. D59, p. 074009, 1999.

[47] X.-D. Ji and J. Osborne, "One Loop Corrections and All Order Factorization in Deeply Virtual Compton Scattering," *Phys. Rev.*, vol. D58, p. 094018, 1998.

[48] J. M. Laget, "Unitarity constraints on deeply virtual compton scattering," *Phys. Rev. C*, vol. 76, p. 052201, Nov 2007.

[49] I. Bedlinskiy *et al.*, "Exclusive η electroproduction at W¿2 GeV with CLAS and transversity generalized parton distributions," *Phys. Rev.*, vol. C95, no. 3, p. 035202, 2017.

[50] J. M. Laget, "Unitarity constraints on neutral pion electroproduction," *Phys. Lett.*, vol. B695, pp. 199–204, 2011.

[51] J. Aubert *et al.*, "The ratio of the nucleon structure functions f2n for iron and deuterium," *Physics Letters B*, vol. 123, no. 3, pp. 275 – 278, 1983.

[52] J. Arrington, A. Daniel, D. Day, N. Fomin, D. Gaskell, and P. Solvignon, "A Detailed Study of the Nuclear Dependence of the EMC Effect and Short-range Correlations," *Phys. Rev.*, vol. C86, p. 065204, 2012.

[53] I. Clot, W. Bentz, and A. Thomas, "Emc and polarized emc effects in nuclei," *Physics Letters B*, vol. 642, no. 3, pp. 210 – 217, 2006.

[54] L. B. Weinstein, E. Piasetzky, D. W. Higinbotham, J. Gomez, O. Hen, and R. Shneor, "Short range correlations and the emc effect," *Phys. Rev. Lett.*, vol. 106, p. 052301, Feb 2011.

[55] O. Hen, E. Piasetzky, and L. B. Weinstein, "New data strengthen the connection between short range correlations and the emc effect," *Phys. Rev. C*, vol. 85, p. 047301, Apr 2012.

[56] S. Liuti and S. K. Taneja, "Microscopic description of deeply virtual compton scattering off spin-0 nuclei," *Phys. Rev. C*, vol. 72, p. 032201, Sep 2005.

[57] B. Mecking *et al.*, "The CEBAF Large Acceptance Spectrometer (CLAS)," *Nucl. Instrum. Meth.*, vol. A503, pp. 513–553, 2003.

[58] M. Mestayer *et al.*, "The CLAS Drift Chamber System," *Nuclear Instruments and Methods in Physics Research Section A: Accelerators, Spectrometers, Detectors and Associated Equipment*, vol. 449, no. 1, pp. 81 – 111, 2000.

[59] M. Amarian *et al.*, "The CLAS Forward Electromagnetic Calorimeter," *Nuclear Instruments and Methods in Physics Research Section A: Accelerators, Spectrometers, Detectors and Associated Equipment*, vol. 460, no. 2, pp. 239 – 265, 2001.

[60] H. Avakain *et al.*, "Deeply Virtual Compton Scattering with CLAS at 6 GeV," *Research Proposal to Jefferson Lab PAC*, vol. PAC 29 PR 06-003, 2005.

[61] K. Hafidi *et al.*, "Deeply Virtual Compton Scattering off 4He," *Research Proposal to Jefferson Lab PAC*, vol. PAC 33 PR 08-024, 2007.

[62] W. R. Leo, *Techniques for Nuclear and Particle Physics Experiments*. Springer-Verlag, 1994.

[63] N. Baltzell, "EG6 EC Sampling Fraction Time-Dependence Correction," August 2013. `https://clasweb.jlab.org/rungroups/lowq/wiki/index.php/EG6_EC_Sampling_Fraction_Time-Dependence_Correction`.

[64] F. T. Cao, "Frank Cao's Kinematic Fitter ," March 2019. DOI: 10.5281/zenodo.2605692 .

[65] F. T. Cao, "Kinematic Fitting On CLAS EG6: Exclusive Coherent π^0 Electroproduction Off ^{4}He," *CLAS Note*, November 2018.

[66] F. T. Cao, "Coherent DVπ^0P with CLAS EG6: Exclusive π^0 Electroproduction Off ^{4}He," *CLAS Analysis Note*, March 2019.

[67] W. Armstrong *et al.*, "Partonic Structure of Light Nuclei," 2017.

[68] A. Accardi *et al.*, "Electron Ion Collider: The Next QCD Frontier," *Eur. Phys. J.*, vol. A52, no. 9, p. 268, 2016.

[69] N. Baltzell and S. Stepanyan, "Beam XY-Position at the Target for CLAS/EG6," *CLAS Note*, April 2013.

[70] N. Baltzell, "RTPC Vertex and Angle Correction," August 2013. `https://clasweb.jlab.org/rungroups/lowq/wiki/index.php/User:RTPC_Vertex_and_Angle_(Aug_7,_2013)`.